Novel orbit-based approaches for matter in strong laser fields

by

Jie Wu

Under the Supervision of Dr Carla Figueira de Morisson Faria

A thesis submitted in partial fulfillment for the
degree of Doctor of Philosophy

University College London
Department of Physics and Astronomy

Examination committee:

Dr. Sergey Yurchenko, Department of Physics and Astronomy (UCL)
Professor Dr. Dieter Bauer, Institute of Physics (University of Rostock)

November 2014

Declaration of authorship

I, Jie Wu, declare that the thesis entitled "Novel orbit-based approaches for matter in strong laser fields" and the work presented in the thesis are both my own, and have been generated by me as the result of my own original research. I confirm that:

- This work was done wholly or mainly while in candidature for a research degree at this University.
- Where any part of this thesis has previously been submitted for a degree or any other qualification at this University or any other institution, this has been clearly stated.
- Where I have consulted the published work of others, this is always clearly attributed.
- Where I have quoted from the work of others, the source is always given. With the exception of such quotations, this thesis is entirely my own work.
- I have acknowledged all main sources of help.
- Where the thesis is based on work done by myself jointly with others, I have made clear exactly what was done by others and what I have contributed myself.

Signed: _____

Date: _____

Abstract

Two novel methods in strong-field and attosecond physics are studied in this thesis: Bohmian trajectories and initial-value representations (IVRs). Both methods describe the system dynamics in terms of trajectories of electrons, and include the binding potential and the laser field. The full solution of the time-dependent Schrödinger equation (TDSE) is used as a benchmark.

First, Bohmian trajectories are applied to high-order harmonic generation (HHG). We find that the trajectory located at the innermost region of the atomic core is the most important for HHG and yields spectra with a well defined plateau and cutoff. Using time-frequency analysis, we associate this trajectory to an ensemble of unbound classical trajectories leaving and returning to the core, and observe arch-like patterns that build up in the phase of the wave function. Furthermore, we relate the Bohmian trajectories to the short and long trajectories encountered in the strong-field approximation (SFA) and show that the central Bohmian trajectory overestimates the contribution of the long SFA trajectory.

Second, IVRs, namely the Herman-Kluk (HK) propagator and the coupled coherent states (CCS) method, are employed in the study of strong-field ionization dynamics. This study is performed in phase space, where signatures of tunneling and over-the-barrier ionization are identified for an initially bound wave packet. Our results indicate that the HK propagator does not fully account for tunneling and over-the-barrier reflections, but partly reproduces features associated with the wave packet crossing classically forbidden regions. In contrast, the CCS method accurately reproduces the results from the time-dependent Schrödinger equation (TDSE). The original CCS, compared with the TDSE, works well in short time propagation. If reprojection of the wave function to the initial grid is

employed quantitative agreement between these two methods, and the first ever CCS computation of HHG spectra, with a plateau and sharp cutoff, is obtained in long time propagation.

Acknowledgements

This thesis could not have been completed without the help of many people.

First of all, I would like to express my earnest appreciation and deep gratitude to Dr. Carla Figueira de Morisson Faria, for her excellent supervision and continuous support. She has not only provided me with extremely helpful insights derived from her rich professional knowledge, but also lighted my academic path in some of the darkest times (e.g. before I achieved a break through in the CCS method) with much encouragement and kindness. Without her, I could not have had the opportunity to pursue my PhD studies at University College London (UCL), nor could have completed this thesis along with several publications on my findings.

I am grateful to the China Scholarship Council (CSC) and the British Department of Business Innovation and Skills (BIS) for funding my PhD studies, especially during my writing up of this thesis, for which BIS has generously agreed to continue providing funding.

I would like to thank Dr. Ángel S. Sanz Ortiz at the Institute of Fundamental Physics in Spain for his collaboration on the Bohmian mechanics. From him I have learnt a great deal about this theory, and without his knowledge and assistance, the modeling in the first part of this thesis could not have been completed successfully.

I also would like to express my sincere gratitude to Dr. Dmitry Shalashilin and Dr. Miklos Ronto at the University of Leeds and Dr. Adam Kirrander when he was at Laboratoire Aimé Cotton in Paris, for their very insightful views on the

CCS method and for sharing the original CCS coding with me. These have served as a solid foundation for the innovative results in the second part of this thesis.

Furthermore, I would like to thank my colleagues Dr. Bradley Bernhard Augstein, Dr. Carlos Zagoya Montiel, Ms Toni Das and Dr. Xuanyang Lai for their valuable contributions during my research work through many insightful discussions. I would like to mention my special thanks to Dr. Carlos Zagoya Montiel, for his selfless help, unsurpassed patience and much appreciated kindness, he has provided me a helping hand to resolve many problems arisen during my PhD studies.

Many thanks also go to Dr. Jing Guo and Professor Xue-shen Liu at Jilin University on the useful discussions on the CCS.

I also would like to acknowledge Dr. Tahir Shaaran and Dr. Yanxin Yu for their kind help in sorting out the early stage of my life in the UK after my initial arrival.

Finally, I would like to give many thanks to my lovely friend, Ms Xiao Yu, for her continuous support and encouragements during my PhD studies, as well as proof reading this thesis and correcting my grammar. At the same time, even though seldomly mentioned, I would always remember the support from my entire family throughout my PhD years and keep them close at my heart.

Frame of this thesis

This work was mainly carried out at the Physics and Astronomy department of University College London (UCL) from October 2010 until March 2014, under the supervision of Dr. Carla Figueira de Morisson Faria. However, it also includes long-term collaborations with Dr. Bradley Bernhard Augstein and Dr. Carlos Zagoya Montiel at UCL, Dr. Dmitry Shalashilin and Dr. Miklos Ronto at the University of Leeds, Dr. Adam Kirrander at the University of Edinburgh and the early stage collaboration with Dr. Ángel S. Sanz Ortiz at Institute of Fundamental Physics in Spain on Bohmian trajectories. Parts of this thesis may be found in the following publications:

Paper 1: J. Wu, B. B. Augstein, and C. Figueira de Morisson Faria, 'Local dynamics in high-order-harmonic generation using Bohmian trajectories', Phys. Rev. A 88, 023415 (2013).

Paper 2: J. Wu, B. B. Augstein, and C. Figueira de Morisson Faria, 'Bohmian-trajectory analysis of high-order-harmonic generation: Ensemble averages, non-locality, and quantitative aspects', Phys. Rev. A 88, 063416 (2013).

Paper 3: C. Zagoya, J. Wu, M. Ronto, D. V. Shalashilin, and C. Figueira de Morisson Faria, 'Quantum and semiclassical phase-space dynamics of a wave packet in strong fields using initial-value representations', New. J. Phys. 16, 103040 (2014).

Paper 4: J. Wu, C. Symonds, M. Ronto, C. Zagoya, B. B. Augstein, A. Kirrander, D. V. Shalashilin, and C. Figueira de Morisson Faria, 'Coupled-coherent state approach for high-order harmonic generation', submitted, Phys. Rev. A

(2014).

Paper 5: B. B. Augstein, J. Wu, T. Shaaran and C. Figueira de Morisson Faria, 'High-harmonic generation and nonsequential double ionization in atoms and molecules: quantum interference, causality, excitation and the role of multiple orbitals', Chapter in book, to be published, Advances in Laser Physics and Technology (2014).

In this thesis, paper 1 and 2 mainly appear in Chapters 3 and 4. Paper 3, 4 and a part of 5 are mainly presented in Chapters 6 and 7. I was the lead author in these publications except for paper 3 and 5. In paper 3, I contributed to the computations of the Wigner function from the CCS as well as to the theory related to this method, the computations of the Wigner function using the HK propagator have been performed by Dr. Carlos Zagoya Montiel. In paper 5, I contributed to the computations of HHG spectra from the CCS and the corresponding theory related to it. However, my contributions were not limited to the results published in thses paper, since I have brought complementary aspects and computations that went beyond the original scope.

Contents

Nomenclature

1D 1 dimensional

3D 3 dimensional

ACF autocorrelation function

AIMS ab initio multiple spawning

ATI above threshold ionization

CCS coupled coherent states

CR coordinate representation

CS coherent state

CSR coherent state representation

CSs coherent states

FFT Fast Fourier transform

G-MCTDH Gaussian multiconfigurational time-dependent Hartree

HHG high-order harmonic generation

HK Herman-Kluk

IFFT inverse Fast Fourier transform

IVR initial value representation

MCTDH multiconfigurational time-dependent Hartree

NSDI non-sequential double ionization

SFA strong-field approximation

SHO simple harmonic oscillator

SPA saddle point approximation

SPEs saddle point equations

TDHF time-dependent Hartree-Fock approximation

TDQMC time-dependent quantum Monte Carlo

TDSE time-dependent Shrödinger equation

TSM three-step model

vMCG variational multiconfigurational Gaussians

VVG Van Vleck-Gutzwiller

List of Tables

List of Figures

Chapter 1

Introduction

Since the first high-intensity highly coherent laser light source became available in the 1960s, laser science has played a vital role in laser-matter interaction research. Because of the rapid development of lasers, studies of the interaction between laser and matter have attracted a large amount of attention in the past few decades. When atoms, molecules or clusters are exposed to an external laser field, their time evolution can be described by the TDSE. If the intensity of the external field $I \ll 10^{13}$ W/cm^2, the external field can be treated as a perturbation. However, for laser fields with higher intensities, perturbation theory breaks down and several new phenomena described as the result of laser-induced scattering or recombination of an electron with its parent ion have been observed, such as HHG, above threshold ionization (ATI) and laser-induced non-sequential double ionization (NSDI).

Due to its potential applications, HHG is recognised as a coherent light source in the extreme ultraviolet [1–4] and soft X-ray [5–7] frequency range. Furthermore, because the physical mechanism behind HHG takes place on the same timescale (attosecond = 10^{-18} s) of an electron rearrangement in a chemical reaction (which in the atomic unit is about 24.3 attoseconds), this phenomenon has become an important tool for generating attosecond pulses [8–10] and attosecond imaging of dynamic process in matters, as well as studying electron correlation in attosecond regime [11–15]. Both experimental and theoretical studies have shown that typical HHG spectra have a common characteristic: it decreases quickly for the first few harmonics, then exhibits a broad plateau followed by a cutoff (as shown

in Fig. 1.1). A very intuitive physical interpretation of HHG that makes reference to electron orbits has been put across in the context of the three step model (TSM) [16–19] and quantum mechanical approaches, such as the SFA [20]. Furthermore, this picture can also be obtained from purely numerical models using time-frequency analysis (see, e.g., [21–24]), such as the numerical solution of the TDSE.

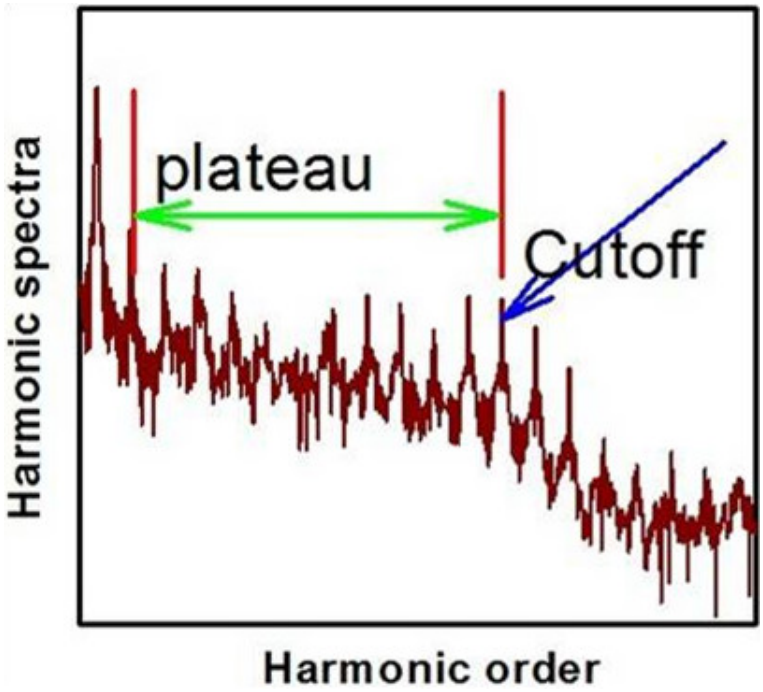

Figure 1.1: The schematic plot of HHG spectrum with a broad plateau and a cutoff located at the end of the plateau.

Initially, the TSM was proposed in a classical framework and describes the following three steps (see Fig. 1.2). First, an electron tunnels through the barrier that is formed by the atomic potential modified by the presence of the laser field. Second, the electron oscillates and gains kinetic energy under the influence of the laser field, during this process the influence of the Coulomb force from the nucleus is practically negligible. Finally, as the laser field inverses its direction, the electron is pulled back to recombine with the parent ion and emits a harmonic photon with the energy of I_p (the ionization energy) plus the kinetic energy ac-

quired during the oscillatory motion. The cutoff of the HHG spectrum is related to the maximal kinetic energy the electron has upon return. If the electron starts from the core, this maximal kinetic energy is $3.17U_p$ for a monochromatic field, where $U_p = E_0^2/4\omega_0^2$ (E_0 is the strength of the laser field, ω_0 is the frequency of the laser field) is the ponderomotive energy *. Classically, the behavior of a quantum mechanical wave packet can be mimicked by an ensemble of electrons which behavior corresponds to the above mentioned recombination picture, and both the binding potential and the external laser field are fully considered. This is also the main idea behind the classical trajectory methods, which have been used to reproduce the main features of the V-shaped structure in NSDI [29, 30] and the low-energy structure in ATI [31].

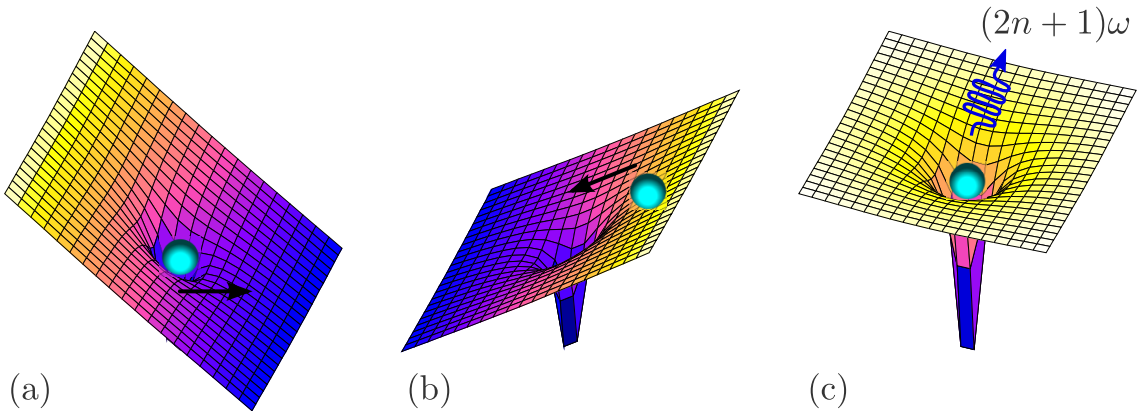

Figure 1.2: The three stages in the high-order harmonic generation process: (a) tunneling, (b) acceleration and (c) recombination. The superposition of the atomic binding potential and the time-dependent laser potential is represented by the surface whereas the electron is represented by the sphere [32].

In contrast to classical methods, most quantum mechanical approaches in strong field physics incorporate quantum interference effects and tunneling ionisation

*In order to circumvent the tunneling problem, electrons start from the excursion amplitude (E_0/ω_0^2) have been studied in Refs. [25–28], which resulted the corresponding maximal kinetic energy around $2U_p$. The main difference between the two initial conditions is that, by placing the electron to start at the excursion amplitude [25–28], one is focusing on the recombination step only, rather than both of the ionization and recombination steps.

with drastic approximations regarding the binding potential. An example is the SFA [20] which in conjunction with the steepest descent method underlines almost any analytical approach to HHG, ATI, NSDI and provides a transparent physical picture for the quantum interference in these phenomena [20, 33–36]. In the SFA, the laser field is neglected when the electrons are bound to atoms or molecules, and the Coulomb potential is neglected when the electrons are in the continuum, furthermore, the internal atomic structure is over simplified. In particular, the electron wave packet in the continuum is approximated by field-dressed plane waves, namely, the Volkov states, but the distinction between the bound and continuum is not clear. Nonetheless, the interplay between the external laser field and the binding potential is important and has revealed itself in many ways. For instance, this interplay has lead to prominent low-frequency structures [31, 37–39], fan-shaped interference patterns [40, 41] in ATI, and strongly influenced NSDI in circularly polarized fields [42, 43]. Because of the importance of the interplay, Coulomb-corrected analytic approaches have been developed in the past few years and successfully applied to strong field phenomena [39, 44–46]. However, these approaches require the external field to be dominant, and it is difficult, especially for big systems, to determine in which regions the binding potential or the external field is dominant. Recently, other orbit-based approaches, such as the Volkov-eikonal approximation [45, 46], the Coulomb-corrected SFA, the HK propagator [26, 28] and the adiabatic approximation [47, 48] have been employed and gone beyond the SFA as the Coulomb potential is incorporated in the electron propagation, even though in many cases only approximately. A list of the main differences between the analytical methods (e.g. the SFA and Coulomb-corrected methods) and the numerical method (TDSE) is given in Table 1.1.

The numerical solution of the TDSE contains no approximation upon the binding potential and the laser field, both of them are fully incorporated. To solve the TDSE numerically is straightforward for one-dimensional, one-electron systems [49, 50], but almost impossible for three-dimensional complex systems, since the numerical effort increases exponentially with the number of degrees of freedom and this limits its wide applications on complex systems. However, with increasing experimental investigations of the attosecond dynamics in multielectron systems [51–55], numerical studies on these complex systems have become

Table 1.1: Comparison of the main advantages and disadvantages of the analytical methods (e.g. the SFA and Coulomb corrected methods) and the numerical method (TDSE).

Analytical methods	**Numerical method**
Provides transparent physical picture of the quantum interference.	Contains no approximations upon $V(r)$ and $E(t)$.
Internal structure of the target is over-simplified.	Straightforward for one-dimensional, one-electron systems.
Continuum is approximated by field-dressed plane waves or binding potentials. Expected to fail if $V \sim r \cdot E(t)$.	Difficult physical interpretation (no clear orbit-based picture).
Requires a clear distinction between bound and continuum states (unclear for large systems).	Prohibitive for multielectron systems (increases exponentially with the number of degrees of freedom).

important. Furthermore, because the numerical solution of the TDSE lacks the clarity of space-time picture in terms of electron orbits, it is of difficult physical interpretation. Typically, this space-time picture is extracted by using windowed Fourier transforms and constructing time-frequency maps. Otherwise, the main focus is on how to minimize the numerical background and spurious reflections in the spectra. From this perspective, it is well known that using the expectation value of the dipole acceleration instead of that of the dipole length normally leads to spectra with large plateau and well-defined cutoff [56, 57]. Physically, it has been argued that, since the light emitted by a moving charge, i.e., the electron, is proportional to its dipole acceleration, it would make more sense to use this quantity as the observable from which HHG spectra are calculated. On a more technical level, the dipole acceleration probes regions near the core, while the dipole length emphasizes large distances. This implies that the latter observable is far more sensitive with regard to reflections at the edges of the box employed in the numerical integration. This sensitivity can be reduced using absorbing boundaries and a Hanning filter, but these devices are expected to alter

the system dynamics. This suggests that regions near the core, where the overlap between continuum and bound dynamics is likely to occur, are important for HHG. This further leads to the question of how the above-stated overlap relates to the physical picture of the TSM.

In order to overcome the above-mentioned problems, we need an orbit-based method with no simplification on the target/binding potential. Furthermore, to understand the overlap in detail, it is helpful to study the probability-density flow associated with the quantum mechanical wave function in specific configuration space region, without losing the phase information.

One of such methods is Bohmian mechanics [58, 59]. In strong field physics to date, Bohmian mechanics has only been employed very recently in a handful of publications [60–72]. It is, however, a powerful tool in order to assess the interplay between the residual potential and the laser field. Within an analytic framework [73], Bohmian trajectories are directly obtained from the full solution of the TDSE. Hence they contain all the quantum phase information necessary for the full description of the problem. Because of this reason, Bohmian trajectories are employed in many areas of physics and chemistry as "tracer particles" [74, 75], which provide an insightful hydrodynamic-like picture of the probability density flow associated with the quantum mechanical wave function (indeed, this picture is pretty much related to Madelung's former hydrodynamical reformulation of quantum mechanics [76].)

Some other orbit-based methods are the initial value representation (IVR) techniques [77, 78], which have evolved into useful orbit-based tools for the simulations of the dynamics of atoms and molecules. Apart from the semiclassical IVR methods, such as the Van Vleck-Gutzwiller (VVG) [79–81] and HK propagators [82–84], Shalashilin and Child have recently developed a quantum IVR method, namely the CCS approach [85–97], which exploits the properties of multidimensional trajectory-guided grids of Gaussian wave packets (i.e. coherent states) as a basis set for the coupled quantum equations. The advantages of the CCS approach are that 1) it can be extended to more degrees of freedom, such as multi-electron atoms and molecules, without scaling problem; 2) the initial

sampling used for the propagation can be chosen randomly; 3) in the coupled equations some cancelations will appear which simplify the quantum mechanical coupling terms; 4) the motion of electrons can be guided by classical mechanics; and 5) it accounts for quantum mechanical effects such as tunneling and quantum interference. Recently, this method has been applied in NSDI ion and electron momentum distributions [97–99]. However, the application of the CCS on HHG has not been reported. This is because in order to be able to apply this method widely, some challenges must be overcome. Particularly, due to the wave function in this method is expanded on the coherent states (obtained from the harmonic oscillator) basis, the CCS strongly depends on the phase of the wave function and works well for harmonic or near harmonic potentials, but requires adaptations if strong anharmonicities are present. Moreover, several technical issues, such as the selection of the initial sampling, the convergency of the wave function and the compensation of the coupling between different coherent states during the propagation, have to be resolved.

Although the phase-space dynamics of a wave packet in strong fields with IVR methods will be studied in Chapter 6, this thesis mainly focuses on the HHG spectra, which can be obtained through the following Fourier transform of the dipole.

$$S(\omega) = \left| \int \mathscr{D}(t) e^{-i\omega t} \mathrm{d}t \right|^2 , \tag{1.1}$$

where $\mathscr{D}(t) = \langle \Psi(t) | \hat{\mathscr{D}} | \Psi(t) \rangle$ is the expectation of the dipole operator $\hat{\mathscr{D}}$, and $|\Psi(t)\rangle$ is the time-dependent wave function, which can be obtained from the TDSE

$$i \frac{\partial |\Psi(t)\rangle}{\partial t} = H(t) |\Psi(t)\rangle. \tag{1.2}$$

However, even for the simplest one electron system no analytical solution of Eq. (1.2) can be obtained. As mentioned in the previous statements, the numerical solutions that incorporate both the binding potential and the laser field, are available but only up to two active electrons. In this thesis we use both the Bohmian trajectory and the IVR methods to study HHG but limit ourself to the one electron system, and hope this could pave the way for large systems.

This thesis is split into two parts. In the first part, we focus on the Bohmian

trajectories. Specifically, in Chapter 2, the basic theory of Bohmian mechanics, and existing methods applied to analyse the Bohmian trajectories and HHG are listed; in Chapter 3, Bohmian trajectories are used to study the local dynamics in HHG; Bohmian trajectory analysis of HHG in the ensemble averages, nonlocality and quantitative aspects are shown in Chapter 4. The second part of this thesis mainly focuses on the IVR methods, it is organised as follows: in Chapter 5 the basic theory of the CCS method is discussed, including a short introduction of coherent states (CSs) and the basic equations in the coherent states representation (CSR) as well as their discrete forms; in Chapter 6 we use the IVR methods to study the phase-space dynamics of a wave packet in strong fields; finally, in Chapter 7, we apply the CCS method to study the autocorrelation function (ACF), discuss reprojection of the wave function to the initial grid and apply this reprojected CCS method to the study of HHG in different kinds of systems; the main conclusions of this thesis are shown in Chapter 8. The appendices detail the complicated derivations of quantities in the CSR. Appendix A.1 is the definition of multi-dimension CSs; Appendix A.2 shows the 3D simple harmonic oscillator (SHO), Gaussian potential and the Coulomb potential in the CSR; the analytic form of the laser field along the $\hat{e}_z$ direction in the CSR is stated in Appendix A.3; we will show different dipole forms in the CSR in Appendix A.4; finally, the derivation of the coefficients of the CSR wave function is shown in Appendix A.5.

Note that, throughout this thesis atomic units are used, although $\hbar$ is shown in Part II and appendix of this thesis to indicate the "quantum nature" of specific equations. In order to distinguish the 1D and 3D CSs, the lower letter z_i (or $|z_i\rangle$) and upper letter Z_i (or $|Z_i\rangle$) are used to denote them respectively. Furthermore, in some equations the foot index of the CSs are removed to indicate that the continuum forms are considered, otherwise the discrete forms are considered.

Part I

Bohmian Mechanics

Bohmian mechanics is also known as the de Broglie-Bohm theory, the pilot-wave theory, the Bohm or Bohm's interpretation, and the causal interpretation. Bohmian mechanics was first proposed by Louis de Broglie in 1927 *, even before the establishment of the Copenhagen interpretation of the quantum particles, and rediscovered by David Bohm in 1952 [58]. Bohmian mechanics provides an explanation of quantum phenomena in accordance to point particles motions guided by waves. Unfortunately, this idea was abandoned by Louis de Broglie. 25 years later David Bohm clarified the meaning and applications of this explanation on quantum phenomena [58].

Bohmian mechanics has become an useful tool in its research activities. Very importantly, Bohmian mechanics can provide very useful explanations of quantum dynamical systems in terms of trajectories, and provides a source of inspiration to discover novel quantum phenomena, such as quantum chaos and two-slit experiment (more details and references about these can be found in Refs. [100] and [**?**]). At the same time, since it provides an alternative mathematical formulation, Bohmian mechanics offers new computational tools to explore physical scenarios which have been computationally inaccessible previously. For instance, based on this theory, Christov proposed the computation of two-electron multi-dimensional time-dependent quantum Monte Carlo (TDQMC) method [101, 102]. Since it accounts for the electron-electron interaction (correlation) and effectively deals with the ionization properties of Helium in the laser field, the results from this method are more accurate than those from the time-dependent Hartree-Fock approximation (TDHF) [103] and paved a new way for the simulation of many-body multi-dimensional systems. In addition, Bohmian mechanics sheds light on the limits and extensions of our present understanding of quantum mechanics towards other paradigms such as relativistic quantum mechanics and quantum field theory [59, 104–106], where the intrinsic structure of Bohmian mechanics in terms of well-defined trajectories is very attractive.

*In 1927, de Broglie found an equation of particle motion equivalent to the guiding equation for a scalar wave function and he explained at the 1927 Solvay Congress how this motion could account for quantum interference phenomena. [Cited from *Goldstein, Sheldon, "Bohmian Mechanics", The Stanford Encyclopedia of Philosophy (Spring 2013 Edition) http://plato.stanford.edu/entries/qm-bohm/.*]

However, numerical complexity has been the main shortcoming in the application of Bohmian trajectories. Since Bohmian trajectories are extracted from the TDSE, according to the present scheme, it is first necessary to solve the full TDSE, which is particularly problematic for systems with many degrees of freedom. Therefore, only a few publications directly applying Bohmian trajectories are reported in the strong-field community. Particularly, Bohmian mechanics has been applied recently to study the ionisation of atoms and molecules, and HHG. For instance, S. Wang revisited the activated dissociation of hydrogen molecules at metal surfaces within the framework of Bohm's reformulation of quantum physics [108]; Lai studied the ATI photoelectron and HHG spectra through Bohmian trajectories [60–62]; A Picón and his coworkers used Bohmian mechanics to study the three-dimensional electron trajectories in linearly and elliptically polarized laser fields [65]; Song applied Bohmian trajectories to study atomic radiative recombination processes and HHG [68, 69].

In Part I of this thesis, in contrast to the conventional scheme of considering a set of Bohmian trajectories, we mainly employ individual Bohmian trajectories to study the HHG in order to probe different regions in the configuration space.

Chapter 2

Background of Bohmian trajectories

This chapter is related to the main theory and background of the next two chapters. Specifically, Section 2.1 is the main theory of Bohmian trajectories; Section 2.2 states the models of the first part of this thesis, including the Hamiltonian, how to use the splitting operator method to propagate the time-dependent wave function, a short introduction of how to compute the HHG from the expectation value of dipole length/acceleration as well as those from Bohmian trajectories are listed; finally, in Section 2.3, the existing approaches, namely the classical-ensemble computations, the SFA and the time-frequency analysis methods, which will be used to study Bohmian trajectories and HHG, are stated.

2.1 Bohmian trajectories

In order to determine Bohmian trajectories, first the time-dependent wave function in the TDSE (1.2) is recast in polar form as

$$\Psi(\vec{R},t) = \rho^{1/2}(\vec{R},t)e^{iS(\vec{R},t)}, \tag{2.1}$$

where ρ is the probability density and S is the real-valued phase. After inserting this form into the TDSE (1.2) and rearranging terms, one obtains a set of two real-valued differential equations, which account for the evolution of both ρ and

S. One is the continuity equation,

$$\frac{\partial \rho}{\partial t} + \nabla \cdot \vec{J} = 0, \tag{2.2}$$

where $\vec{J} = \rho \nabla S$ is the usual quantum probability current density.

The other one is the quantum Hamilton-Jacobi equation,

$$\frac{\partial S}{\partial t} + \frac{(\nabla S)^2}{2} + V + Q = 0, \tag{2.3}$$

where

$$Q(\vec{R}, t) = -\frac{1}{2}\frac{\nabla^2 \rho^{1/2}}{\rho^{1/2}} = -\frac{1}{4}\left[\frac{\nabla^2 \rho}{\rho} - \frac{1}{2}\left(\frac{\nabla \rho}{\rho}\right)^2\right], \tag{2.4}$$

is the so called quantum potential and S is the equivalent of the classical action, and V is the atomic potential.

As happened with the classical analog of Eq. (2.3), one can postulate [58, 59] the existence of trajectories (characteristics) that are solutions to this equation. Similar to the classical case, these trajectories are perpendicular to surfaces of constant phase and therefore the corresponding equation of motion is proportional to ∇S. Alternatively, the same can also be straightforwardly stated if Eq. (2.2) is regarded as describing a quantum transport problem [74], with a local velocity field defined as $\vec{v} = \vec{J}/\rho$. In either case one obtains the equation of motion

$$\dot{\vec{R}} = \nabla S = \frac{\vec{J}}{\rho} = -\frac{i}{2}\left(\frac{\Psi^* \nabla \Psi - \Psi \nabla \Psi^*}{|\Psi|^2}\right) = \mathrm{Im}\left(\frac{\nabla \Psi}{\Psi}\right), \tag{2.5}$$

which, after integration at each time step, i.e., once the wave function $\Psi(\vec{R}, t)$ and the initial conditions $\vec{R}(0)$ are obtained, gives the corresponding Bohmian trajectories.

2.2 Model

2.2.1 Hamiltonian

For the sake of simplicity, we consider our model in one spatial dimension, which contains the essential physical elements for linearly polarized fields. Making use

of the dipole approximation and the length gauge, the electron dynamics can then be described by the time-dependent Hamiltonian (in atomic units), which is given by:

$$H = -\frac{1}{2}\nabla^2 + V(x) - xE(t) \tag{2.6}$$

where, $E(t)$ denotes the driving field and $V(x)$ is the binding potential.

In the first part of this thesis, we will mainly assume that the atomic potential, $V(x)$, is given by either the long-range soft-core potential

$$V_{sc}(x) = -\frac{1}{\sqrt{x^2+a^2}}, \tag{2.7}$$

or the truncated short-range potential

$$V_{tr}(x) = -\frac{1}{\sqrt{x^2+a^2}} f(x), \tag{2.8}$$

where a is the impact parameter. Far away from the core, this potential decays as x^{-1}, behaving similarly to a Coulomb-type, long-range interaction. Here we have chosen the impact parameter to be $a = 1$, which yields a ground-state energy $\epsilon_0 = -0.66995$ for the field free [$E(t) = 0$ in Eq. (2.1)] Hamiltonian. And the truncating function is described as

$$f(x) = \begin{cases} 1, & |x| < a_0 \\ \cos^7\left(\frac{\pi}{2}\frac{|x|-a_0}{L-a_0}\right), & a_0 \le |x| \le L \\ 0, & |x| > L \end{cases} \tag{2.9}$$

The explicit values of a_0 and L have been chosen in two different ways, which will be specified later in Section 3.1 (see Table 3.1 for details). A similar truncation was formerly used in Ref. [109] to assess the influence of the potential tail on resonant HHG enhancements.

Regarding the external laser field, $E(t) = E_0 f(t)\sin(\omega_0 t)$, several kinds of envelopes, $f(t)$, have been considered, namely a flat-top trapezoidal pulse, where

$$f(t) = \begin{cases} t/\tau_{on}, & 0 \le t < \tau_{on} \\ 1, & \tau_{on} \le t < \tau_{off} \\ 1-(t-\tau_{off})/\tau_{on}, & \tau_{off} \le t \le \tau_f \end{cases}, \tag{2.10}$$

and a $\sin^2$ function, where

$$f_{s^2}(t) = \sin^2(\pi t/\tau_f). \tag{2.11}$$

In both cases, $\omega_0 = 0.057$ and $\tau_0 = 2\pi/\omega_0$ denote the frequency and period of the field, respectively. More specifically, in (2.10) the time required for the external field to reach its maximum amplitude is $\tau_{on} = 2.25\tau_0$, while $\tau_{off} = 2.25\tau_0 + N\tau_0$ stands for the duration of the field with maximum amplitude, and $\tau_{off} + 2.25\tau_0$ refers to the time at which the field is switched off (and our quantum simulations are completed); to ensure a high monochromaticity in the flat-top pulse, we have chosen $N = 10$ ($\tau_f = 14.5\tau_0$).

2.2.2 The propagation of the wave function

As the initial condition for the wave function, we have considered the ground state of the bare or field-free Hamiltonian,

$$H_0 = -\frac{1}{2}\nabla^2 + V(x). \tag{2.12}$$

This eigenstate has been numerically obtained by means of the imaginary time propagation method [110]. Starting from the Schrödinger equation (1.2) and the Hamiltonian (2.1), the time-dependent wave function can be written as [111]

$$\Psi(x, t + \Delta t) \approx e^{-i\frac{\hat{p}^2}{2}\Delta t/2} e^{-i[V(x) - xE(t+\Delta t/2)]\Delta t} e^{-i\frac{\hat{p}^2}{2}\Delta t/2} \Psi(x, t) + O(\Delta t^3). \tag{2.13}$$

Then, the time-propagation of the wave function according to the TDSE (1.2) can be carried out from time t to $t+\Delta t$ by combining the split-operator technique [111] with the Fast Fourier Transform (FFT) technique [112, 113] in the following steps:

1. By using the FFT method, the wave function $\Psi(x, t)$ is changed to the momentum space,

$$\Psi(x, t) = \sum_n \varphi_1(p_n, t) e^{ip_n x}. \tag{2.14}$$

Here, the $\varphi_1(p_n, t)$ coefficients denote the Fourier weights (in general, complex valued) associated with each of the plane-wave components with momentum p_n of the decomposition at time t. Then,

$$e^{-i\frac{\hat{p}^2}{2}\Delta t/2} \Psi(x, t) = \sum_n e^{-i\frac{\hat{p_n}^2}{2}\Delta t/2} \varphi_1(p_n, t) e^{ip_n x} = \sum_n \varphi_1'(p_n, t) e^{ip_n x}. \tag{2.15}$$

2. By using the Inverse Fast Fourier Transform (IFFT), the new wave function in the momentum space is changed to the coordinate space as $\Psi_2(x,t)$, and after that we obtain

$$e^{-i[V(x)-xE(t+\Delta t/2)]\Delta t}\Psi_2(x,t) = \Psi_2'(x,t). \tag{2.16}$$

3. By using the FFT again, the new wave function in the coordinate space is changed to the momentum space as

$$\Psi_2'(x,t) = \sum_n \varphi_3(p_n,t)e^{ip_n x}. \tag{2.17}$$

Then,

$$\Psi(x,t+\Delta t) = e^{-i\frac{\hat{p}^2}{2}\Delta t/2}\Psi_2'(x,t) = \sum_n e^{-i\frac{\hat{p}_n^2}{2}\Delta t/2}\varphi_3(p_n,t)e^{ip_n x} = \sum_n \varphi_3'(p_n,t)e^{ip_n x}. \tag{2.18}$$

From Eq. (2.14) we can see

$$\nabla\Psi(x,t) = \sum_n \varphi_1(p_n,t)\nabla e^{ip_n x} = \sum_n ip_n\varphi_1(p_n,t)e^{ip_n x}. \tag{2.19}$$

Regarding the Bohmian equation of motion (2.5), it has been integrated "on the fly", by substituting the value of the wave function $\Psi(x,t)$ at each time step into this equation. Now, given the general form (2.14), Eq. (2.5) can be recast as

$$\dot{x} = \mathrm{Im}\left[\frac{\sum_n ip_n\varphi_1(p_n,t)e^{ip_n x}}{\sum_n \varphi_1(p_n,t)e^{ip_n x}}\right]. \tag{2.20}$$

This way, since $\varphi_1(p_n,t)$ are known at each time step through the FFT operation, Bohmian trajectories $x(t)$ can be obtained straightforwardly by integrating the analytical form (2.20), which is an ordinary differential equation. In particular, the integration can be performed by means of the 4^{th} order Runge-Kutta or the Euler method, as soon as the initial conditions of $x(0)$ are obtained.

In this thesis, the initial conditions $x(0)$ considered for the Bohmian trajectories have been randomly chosen to mimic the initial probability distribution,

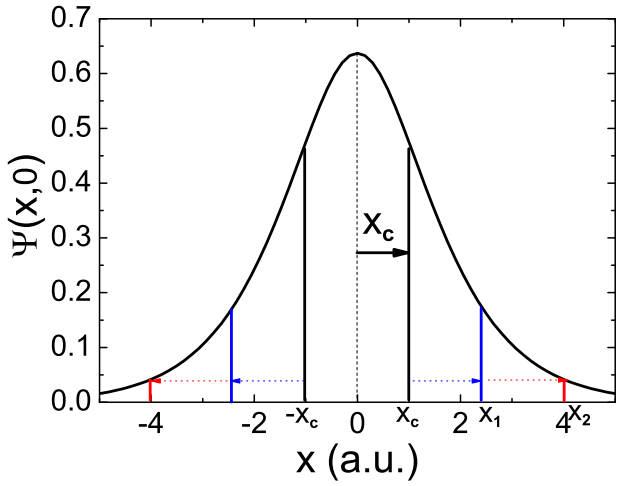

Figure 2.1: Schematic plot of how to choose the initial positions ensemble for Bohmian trajectories in a specific interval, corresponding to the probability distribution. The black solid curve is the ground state wave function of the soft-core potential Eq. (2.7). For a sampling with N initial positions in the whole space, we randomly choose $N\int_{-x_c}^{x_c}|\Psi(x,0)|^2\mathrm{d}x$ from the interval $[-x_c,x_c]$ or $N\int_{x_1}^{x_2}|\Psi(x,0)|^2\mathrm{d}x$ from the interval $[x_1,x_2]$.

$\rho(x,0)=|\Psi(x,0)|^2$, within the interval $[-x_c,x_c]$, with $x_c=4.102$. This ensures that the time-evolution of most of the propability density will be well monitored, as the integrated probability for $|x|\geq x_c$ is only 0.151% of the total probability. An illustration of how to choose the initial conditions is shown in Fig. 2.1

To ensure that all the relevant dynamics are incorporated for the parameter range of interest, we have set the box boundaries located far enough from the core region (at $|x|=150$). Furthermore, special care has been taken in order to avoid reflections and spurious effects near the box edges. First, we have employed a mask function in the form of a $\cos^{1/8}$ function

$$M(x)=\begin{cases}\cos^{1/8}\left[\frac{\pi|x+x_1|}{2(-l+x_1)}\right], & x\leq -x_1\\ 1, & -x_1<x<x_1\\ \cos^{1/8}\left[\frac{\pi|x-x_1|}{2(l-x_1)}\right], & x\geq x_1\end{cases} \tag{2.21}$$

which becomes active near the boundaries $\pm x_1$. This function is smooth enough, but still capable of absorbing noises with a high efficiency, thus avoiding nonphysical reflections. We have tested this fact by considering a wide range of box sizes. Second, the maximum/minimum value of the total potential function has been truncated in order to avoid nonphysical accelerations towards the box edges. In this regard, the size of the box is chosen such that this truncation takes place close to the region where the absorber becomes active.

Additionally, to avoid effects associated with the loss of probability due to the presence of the absorber, which becomes more prominent for higher external field intensity, in the calculations special attention is paid to proper renormalisation of the wave function. Finally, unless otherwise stated, no filter functions (e.g., Hanning windows) are used to avoid influence on the long-range dynamics and therefore the topology of Bohmian trajectories.

2.2.3 High-order harmonic generation (HHG) spectrum

The HHG spectrum can be obtained through the Fourier transform of the dipole:

$$S(\omega) = \left| \int \mathscr{D}(t) e^{-i\omega t} \mathrm{d}t \right|^2 . \tag{2.22}$$

The quantity $\mathscr{D}(t)$ that we are interested in here is the dipole length

$$\bar{x}(t) = \langle \Psi(t) | x | \Psi(t) \rangle, \tag{2.23}$$

which, in atomic units, is equal to the dipole moment but with opposite sign, since $\mu(t) = e\bar{x}(t)$; and the dipole acceleration expressed as

$$\bar{a}(t) = -\langle \Psi(t) | V'(x) | \Psi(t) \rangle, \tag{2.24}$$

where $V'(x) = \mathrm{d}V(x)/\mathrm{d}x$, is defined as the acceleration operator [114], for the soft-core potential (2.7), this term is read as $x/(x^2 + a^2)^{3/2}$. In these expressions, $\Psi(x, t)$ denotes the wave function solution of the TDSE (1.2).

Once Bohmian trajectories are synthesised, two types of calculations can be carried out with them. The first type is a direct evaluation of their individual spectrum in order to determine how each trajectory contributes to the expectation

values of (2.23) and (2.24). That is, we might study the power spectrum (2.22) for a series of individual trajectories, substituting $\mathscr{D}(t)$ by the time-dependent trajectory $x(t)$ obtained after integrating Eq. (2.20) with the corresponding initial condition $x(0)$. In the second type, we can understand the ensemble feature of Bohmian mechanics, by analysing the ensemble of the usual dipole length and acceleration as the number of Bohmian trajectories is increased with their initial positions distributed randomly according to $\rho(x,0)$ mentioned in Section 2.2.2. The Bohmian version of the expectation values of (2.23) and (2.24) are given by

$$\bar{x}_B(t) = \frac{1}{N}\sum_{i=1}^{N} x_i(t), \tag{2.25}$$

and

$$\bar{a}_B(t) = \frac{1}{N}\sum_{i=1}^{N} \frac{\mathrm{d}V(x)}{\mathrm{d}x}\bigg|_{x=x_i(t)} = \frac{1}{N}\sum_{i=1}^{N} \frac{x_i(t)}{\left[1+x_i^2(t)\right]^{3/2}}, \tag{2.26}$$

respectively, which follow the usual statistical approach (i.e. the average value contributed from each trajectory is considered). In these expressions, $x_i(t)$ denotes the ith Bohmian trajectory from an ensemble and N is the total number of trajectories in each numerical experiment performed.

2.3 Existing methods applied to analyse Bohmian trajectories and HHG

2.3.1 Classical-ensemble computations

In order to compare Bohmian and classical trajectories, we solve the classical equations of motion for an ensemble of electrons which are released in the laser field at time t_0. For each electron,

$$\ddot{x}(t) = F(x,t) \tag{2.27}$$

both in the presence and in the absence of the soft-core potential. In the former and the latter case, $F(x,t) = E(t) - dV(x)/dx$ and $F(x,t) = E(t)$, respectively. The initial release time t_0 is then varied within a monochromatic field given by $E(t)$. Only a subset of the trajectories obtained will return to the core, depending

on the time at which the electrons are released into the field. For a monochromatic field this will occur only for times $t_0 > 0.25\tau_0 + n\tau_0/2$ (τ_0 is the period of the laser field and n is an non-negative integer), i.e., after the peak-field times, and up to $t_0 \simeq 0.4\tau_0 + n\tau_0/2$, i.e., somewhat before the crossing, where, τ_0 is the period of the external laser field.

Assume the monochromatic laser field is $E(t) = E_0 \cos(\omega_0 t)$, the potential is absent, integrating Eq. (2.27) once and twice gives

$$\dot{x}(t) = \frac{E_0}{\omega_0} \sin(\omega_0 t) + \dot{x}(0), \tag{2.28}$$

and

$$x(t) = -\frac{E_0}{\omega_0^2} \cos(\omega_0 t) + \dot{x}(0)t + x(0), \tag{2.29}$$

respectively. Assume the initial velocity and position of the electron in the laser field are $\dot{x}(t_0) = v_0$ and $x(t_0) = x_0$, respectively, where t_0 is the ionisation time of the electron. One can obtain the $\dot{x}(0)$ and $x(0)$, which read as

$$\dot{x}(0) = v_0 - \frac{E_0}{\omega_0} \sin(\omega_0 t_0), \tag{2.30}$$

and

$$x(0) = \frac{E_0}{\omega_0^2} \cos(\omega_0 t_0) - \dot{x}(0)t_0 + x_0, \tag{2.31}$$

respectively. For an arbitrary time t, the velocity and the position of an electron can then be rewritten as

$$\dot{x}(t) = \frac{E_0}{\omega_0} \left[\sin(\omega_0 t) - \sin(\omega_0 t_0)\right] + v_0 \tag{2.32}$$

and

$$x(t) = \frac{E_0}{\omega_0^2} \left[\cos(\omega_0 t_0) - \cos(\omega_0 t)\right] + \frac{E_0}{\omega_0}(t_0 - t)\sin(\omega_0 t_0) + v_0(t - t_0) + x_0, \tag{2.33}$$

respectively. If we assume $v_0 = 0$, $x_0 = 0$ and solve the equation $x(t) = 0$, we can obtain the return time t_r of the electron, inserting t_r into Eq. (2.32) we can obtain the return velocity and the corresponding kinetic energy E_k, which reads as

$$E_k = 2U_p \left[\sin(\omega_0 t_r) - \sin(\omega_0 t_0)\right]^2, \tag{2.34}$$

in which, $U_p = E_0^2/4\omega_0^2$ is the ponderomotive energy of the electron in the laser field. The maximum kinetic energy is about $3.17U_p$, which added to I_p gives the cutoff position predicted by the TSM.

If the soft-core potential is included, Eq. (2.27) is rewritten as the coupled first order differential equations,

$$v(t) = \dot{x}(t) \tag{2.35}$$

and

$$\dot{v}(t) = E_0 \cos(\omega_0 t) - \nabla V(x), \tag{2.36}$$

which are solved employing the 4^{th} order Runge-Kutta method. However, solving these equations with the same initial conditions as in the potential-free case, i.e. with $x_0 = 0$ and $v_0 = 0$, leads to a series of bound trajectories, whose kinetic energy is very low and are not appropriate for the comparison one may wish to perform. Hence, we have placed the electrons initially at $x_0 = 0$ but with velocity v_0 such that $v_0^2/2 = -V(x_0)$. This gives $v_0 = \pm\sqrt{2}$ for the potentials employed in this work. These trajectories will exhibit unbound dynamics. Similar dynamics may be obtained by assuming that the electrons in the ensemble leave with vanishing velocity $v_0 = 0$ but initially located at a turning point x_0, such that $F(x_0, t_0) = 0$. A schematic plot related to this turning point is shown in Fig. 2.2.

2.3.2 Strong-field approximation (SFA)

Initially Lewenstein et al. [20] and Becker et al. [115] independently applied the SFA to the study of HHG using a zero-range potential. An integrated approach was subsequently developed to unify these two methods [116]. The SFA starts from the TDSE of a one-electron atom exposed to a linearly polarised laser field in the length gauge, in which the 1D Hamiltonian reads as Eq. (2.6) and the following three main assumptions hold:

1. Only the contribution of the ground state to the evolution of the system is considered, the contribution of all bound states can be neglected.

2. The depletion of the ground state can be neglected.

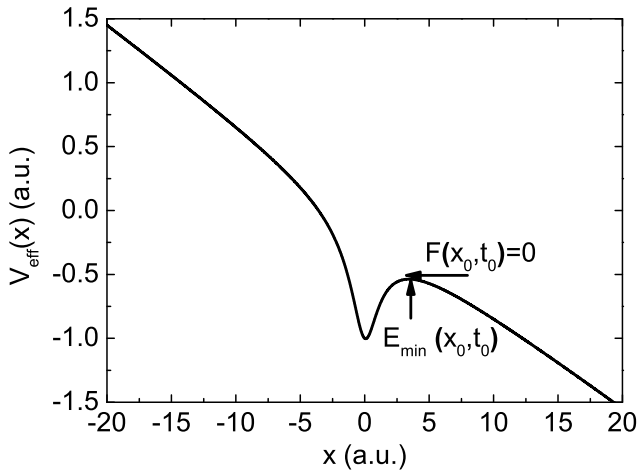

Figure 2.2: Schematic plot of the turning point related to Eq. (2.36), at time t_0. In this figure, the effective potential is defined as $V_{eff}(x) = V(x) - xE(t_0)$, and $E_{min}(x_0, t_0)$ is the minimum energy that an electron needs to escape via over-the-barrier ionisation, which corresponds to $F(x_0, t_0) = 0$ and the turning point x_0 at t_0.

3. In the continuum, the effect of $V(x)$ on the motion of an electron in the laser field is negligible, i.e. the electron moves as a free particle.

With these assumptions the time-dependent wave function in Eq. (1.2) can be expressed as the superposition of the ground state $|0\rangle$ and the continuum state $|v\rangle$, which reads as

$$|\Psi(t)\rangle = e^{iI_P t}\left(C_0(t)|0\rangle + \int C_v(t)|v\rangle \mathrm{d}v\right), \tag{2.37}$$

where $C_0(t) \simeq 1$ is the amplitude of the ground state (assumption 2) and $C_v(t)$ are the amplitudes of the corresponding continuum states.

By inserting this wave function into the TDSE and applying assumption 2 above, one can obtain the differential equation of the continuum amplitudes $C_v(t)$:

$$\dot{C}_v(t) = -i\left(\frac{v^2}{2} + I_p\right)C_v(t) - E(t)\frac{\partial C_v(t)}{\partial v} + iE(t)d_x(v), \tag{2.38}$$

where $d_x(v) = \langle v|x|0\rangle$ denotes the dipole matrix element of the bound-free transition. The analytical solution of Eq. (2.38) is

$$\begin{aligned} C_v(t) = i \int_0^t E(t') d_x \left(v + A(t) - A(t')\right) \\ \times \exp\left\{-i \int_{t'}^t \mathrm{d}t'' \left[\left(v + A(t) - A(t'')\right)^2 /2 + I_p\right]\right\} \mathrm{d}t', \end{aligned} \tag{2.39}$$

where $A(t) = -\int E(t)\mathrm{d}t$ is the vector potential of the laser field.

After the amplitudes of the continuum states are obtained, by applying assumption 3 above, we can get the time-dependent dipole moment along the laser field direction $x(t) = \langle \Psi(t)|\hat{x}|\Psi(t)\rangle$ which is written as

$$x(t) = \int d^*(v) C_v(t) \mathrm{d}v + c.c. \tag{2.40}$$

Introducing the canonical momentum

$$p = v + A(t), \tag{2.41}$$

the above equation can be rewritten as

$$x(t) = i \int_0^t \mathrm{d}t' \int E(t') d_z(p - A(t')) d_z^*(p - A(t)) \exp[-iS(p, t, t')] \mathrm{d}p + c.c. \tag{2.42}$$

where

$$S(p, t, t') = \int_{t'}^t \left\{\frac{1}{2}\left[p - A(t'')\right]^2 + I_p\right\} \mathrm{d}t''. \tag{2.43}$$

The corresponding Fourier transform of the dipole moment reads as

$$\begin{aligned} F(\omega) = i \int_{-\infty}^{\infty} \mathrm{d}t \int_0^t \mathrm{d}t' \int E(t') d_x(p - A(t')) d_z^*(p - A(t)) \\ \times \exp[-iS(p, t, t', \omega)] \mathrm{d}p + c.c. \end{aligned} \tag{2.44}$$

where

$$S(p, t, t', \omega) = \int_{t'}^t \frac{1}{2}\left[p - A(t'')\right]^2 \mathrm{d}t'' + I_p(t - t') - i\omega t \tag{2.45}$$

is the classical action which describes the propagation of a free moving electron in the continuum from time t' to t.

The highly oscillatory feature of the classical action mainly determines the oscillatory behavior of Eq. (2.44). The major contribution to the integral over p comes from the stationary points of the action. This approach is called the saddle point approximation (SPA) and the corresponding saddle point equations (SPEs) are:

$$\frac{\partial S(p,t,t',\omega)}{\partial t'} = \frac{1}{2}\left(p - A(t')\right)^2 + I_p = 0 \tag{2.46}$$

$$\frac{\partial S(p,t,t',\omega)}{\partial t} = \frac{1}{2}\left(p - A(t)\right)^2 + I_p - \omega = 0 \tag{2.47}$$

$$\frac{\partial S(p,t,t',\omega)}{\partial p} = \int_{t'}^{t} \left(p - A(t'')\right) \mathrm{d}t'' = 0. \tag{2.48}$$

Eq. (2.46) states that the kinetic energy of the electron at the instant of tunneling is equal to its binding energy, and only complex solutions exist for this equation meaning that tunneling has no classical counterpart. Eq. (2.47) expresses the conservation of energy at instant t of recombination, where the kinetic energy of the returning electron is converted into a high-order harmonic of frequency ω. Eq. (2.48) restricts the recombination of the electron to the site of ionisation. The trajectories obtained from these solutions are known as "quantum orbits" in the strong-field community [117], and have been used by many research groups across the globe (for example, the work on the steepest descent method and HHG, see Refs. [118–120]). Their real parts are related to the classical trajectories of an electron in a laser field. The imaginary parts are related to quantum mechanical processes and represent the width of the barrier that the electron must tunnel through.

2.3.3 Time-frequency analysis

Although one can use modulus of the Fourier transform of time-dependent atomic dipole to obtain the HHG spectrum, all the temporal information of HHG is lost under this approach. Certain features of HHG, which yield considerable information on its physical mechanisms, such as the semiclassical return times in the TSM [121], or the time-dependent level crossings in two-level atoms [122, 123], can only be revealed by a time-frequency or wavelet analysis.

The theoretical method related to the above statement was first proposed by Gabor in 1946 [124] based on the classical Fourier transform, but with introducing of the window function. During the past decades, this method has been widely applied to the study of signal and image processing, acoustical phenomena and medicine [125, 126]. Recently, this method was applied by Antoine [127] to study the emission of a given harmonic occurring during the interaction between atoms and the external laser field, and time interval, in which a given harmonic is preferably emitted. This method has powerful applications, for instance, it can provide both new information about the fundamental mechanism which leads to HHG and the competition between processes of photon emission and excitation or ionization [127], and therefore has been widely used to study HHG [22–24, 128–130].

In order to assess how Bohmian trajectories are related to those identified in the context of SFA, we will employ time-frequency analysis (the Gabor transform) to extract temporal information from the TDSE or from groups of Bohmian trajectories. For a generic function $\mathscr{D}(t)$, the Gabor transform reads as

$$a_G(\omega, t) = \int \mathscr{D}(t) \exp[-(t - t')^2/(2\sigma^2)] \exp(i\omega t') \mathrm{d}t'. \tag{2.49}$$

Note that, if $\sigma \to \infty$ the standard Fourier transform is recovered and all temporal information is lost. Here, we choose the same temporal width as that employed in Ref. [128], i.e., $\sigma = 1/(3\omega_0)$ (ω_0 is the frequency of the external laser field).

Chapter 3

Local dynamics in HHG using Bohmian trajectories

In this chapter we investigate the HHG spectra through Bohmian mechanics. Over recent years Bohmian mechanics has been adopted to provide descriptions and interpretations for phenomena in strong field physics [60–64] as well as serve as a source for numerical algorithms [65, 67–69]. These studies primarily follow the traditional approach where a set of Bohmian trajectories are employed and the obtained results are compared to those from quantum mechanics. In contrast, in this chapter we consider individual Bohmian trajectories and use them to probe different critical areas in the configuration space. Using a simplified 1D model, we show that (1) HHG spectra with a clear plateau and a cutoff can be reproduced by the Bohmian trajectory located in the innermost region of the core, in other words, in the vicinity of $x = 0$; (2) according to the TSM prediction, an ensemble of classical electron trajectories returning to the parent ion can be related to the innermost Bohmian trajectory; and (3) under Bohmian mechanics, the picture related to the TSM builds up nonlocally via the phase of the wave function, and as expected from the TSM, any alterations in the flow of the wave function far away from the core region will impact the central trajectory. We illustrate this by applying long- and short-range potentials, which essentially have the same core region, but a considerable different propagation of the wave function outside the core.

The structure of this chapter is as follows. In order to illustrate that Bohmian

trajectory is a powerful tool to probe the local dynamics in HHG, in Section 3.1 we compare the HHG spectra obtained from dipole length and acceleration through the TDSE with those from Bohmian trajectories. To substantiate that the results from Bohmian trajectories are generic, different kinds of model potentials and external laser fields are considered. Following this, in Section 3.2, in order to address the question of how Bohmian trajectories compare to the classical trajectories of an electron in a strong laser field, time-frequency analysis is applied to study the central and peripheral Bohmian trajectories. Finally, the last section presents the conclusions of this chapter.

3.1 The dipole length and acceleration compared with Bohmian trajectory

It is well known that in the TDSE computations, the expectation value of the dipole acceleration (rather than the dipole length) produces "cleaner" HHG spectra, with plateau and well-defined cutoff. The dipole acceleration concentrates on regions near the core, whereas the dipole length places more focus on regions far away from the core. This implies that regions important for the HHG are those near the core, where overlap between the continuum and bound dynamics is most likely to occur. However, this raises further thought-provoking questions, such as: can a specific region in the core be singled out as being the most relevant to HHG? How can the overlap mentioned above be related to the physical picture described by the TSM?

In order to address these questions we first revisit the issue of the dipole length and acceleration for the standard soft-core potential [$f(x) = 1$ in Eq. (2.8)] employing Bohmian dynamics. The dipole length over-emphasises regions near the box edges due to its linearity with the distance. Hence, even if the probability density far from the core is negligible, x can reach relatively high values, thus compensating this fact and enhancing the associated features in the corresponding spectra. In contrast, the dipole acceleration focuses on the core region. Specifically, for the soft-core potential, it increases up to $x = \pm 1/\sqrt{2}$, and then decreases to zero again very rapidly, such as in x^{-2} form. Hence, any contribution

from portions of the probability density outside this region is strongly suppressed [56].

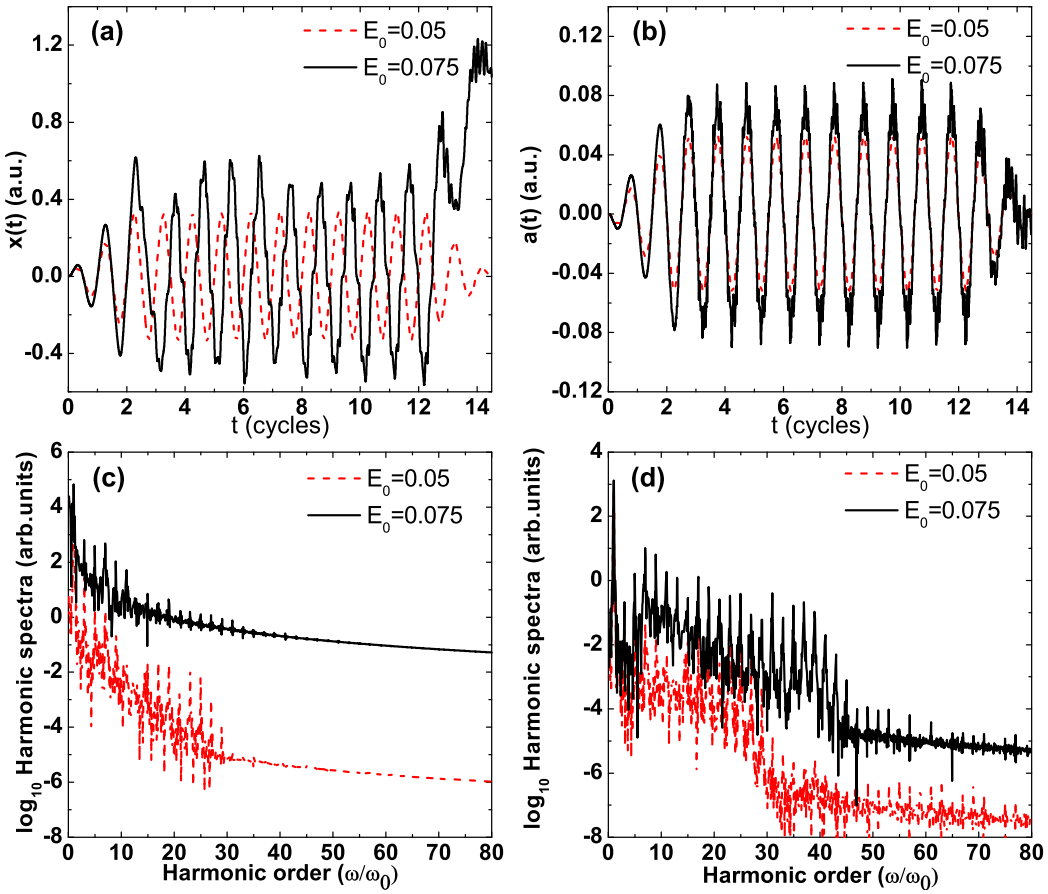

Figure 3.1: Dipole length (a) and dipole acceleration (b) computed from the TDSE for a soft-core potential $V_{sc}(x)$ in a flat-top trapezoidal laser pulse with frequency $\omega_0 = 0.057$, and intensities $E_0 = 0.05$ (dashed red line) and $E_0 = 0.075$ (black solid line). The corresponding HHG spectra are displayed in panels (c) and (d), respectively. The cutoff frequencies in the cases considered are $\omega = 22.5\omega_0$ for $E_0 = 0.05$, and $\omega = 35.8\omega_0$ for $E_0 = 0.075$.

In Fig. 3.1, we show the time-dependent dipole length [panel (a)] and acceleration [panel (b)] obtained from Eqs. (2.23) and (2.24) respectively, which are

computed using the TDSE. Moreover, the corresponding harmonic spectra are provided in the lower panels. As shown in Fig. 3.1(a), as the field strength E_0 increases, the amplitude of the oscillations for the dipole length becomes comparatively large. Furthermore, at the end of the pulse, the expectation value of the dipole operator is non-vanishing for the larger driving-field intensity. This can be traced to irreversible ionization and the contributions far from the core region, which are over-estimated in this case. The dipole acceleration [see Fig. 3.1 (b)], however, behaves in a rather different way. First, there is a much less pronounced increase in the amplitude of $a(t)$ with the driving-field strength. Comparing the two graphs, we note that their main difference lies in the substructure observed for $a(t)$. Second, the acceleration vanishes at the end of the pulse. These differences stem from the fact that $a(t)$ only depends on the part of the wave function where the electron undergoes the strongest interaction with the core, as discussed above.

When comparing the spectra for the dipole length and the acceleration for such intensities, however [see Figs. 3.1(c) and (d)], one readily notices that the spectra obtained from the dipole acceleration exhibit a plateau consisting of high-order harmonics extending up to a cutoff energy of $\omega_c \approx I_p + 3.17U_p$, where I_p is the ionisation energy and $U_p = E_0^2/4\omega_0^2$ is the ponderomotive energy. These features, shown in Fig. 3.1(d), are in full agreement with the predictions of the TSM. In the harmonic spectra computed from the dipole length, however, these features are not so easily identifiable. In particular, for higher driving-field intensity, the harmonic peaks are obfuscated by a large background, with no visible plateau. Overall, the HHG spectra in Fig. 3.1(c) are monotonically decreasing. Nonetheless, for moderate intensities of the external field [see curve for $E_0 = 0.05$] the cutoff could be assigned to the dramatic decrease in the intensity observed around $\omega \approx 30\omega_0$.

We will now employ Bohmian trajectories in order to analyse these differences in detail. In Figs. 3.2(a) and (b) two sets of Bohmian trajectories are displayed for the same driving-field intensities as those in Fig. 3.1. As E_0 increases some of the trajectories start to oscillate with increasingly larger amplitudes and eventually leave the core region [see panel (b)]. Actually, it is the behavior of E_0 that leads to the eventual dependence on the boundaries. That is, as E_0 increases,

the trajectories undergo larger excursions out of the core and therefore, when their average (2.25) is computed, one will obtain results highly dependent on the boundary conditions chosen to solve the TDSE. Note that this average formally corresponds to the expectation value of the dipole moment. On the contrary, if one only focusses on those Bohmian trajectories that always keep oscillating around the core, the average behavior will resemble that of the dipole acceleration.

The interpretation provided above is supported by the harmonic spectra obtained from a single Bohmian trajectory $x_i(t)$, depicted in the lower panels of Fig. 3.2. As an overall feature, a plateau followed by a cutoff is always obtained if a trajectory starting at $x(0) = 0$ is taken, regardless of the driving-field intensity. This trajectory corresponds to the innermost part of the wave function, which is strongly localised at the core. This spatial region resembles that spanned by the dipole acceleration. In contrast, the spectra from trajectories whose initial positions lie at a few atomic units of distance, i.e., at the outermost regions of the wave function, will be strongly influenced by the driving-field intensity. For moderate driving-field intensity [Fig. 3.2(c)] the spectra from both innermost and outer trajectories are quite similar in shape, apart from an overall intensity difference. If, however, the intensity increases, the spectra of the innermost and the outermost trajectories differ markedly, as exemplified in Fig. 3.2(d). In this figure, one observes that, if the trajectories are launched from $x(0) = -3$, or even $x(0) = 1.8$, the corresponding spectra will only consist of the fundamental and of a uniform background. For these initial conditions, the confined oscillating motion (around the corresponding initial position) is lost.

Apart from that, the further from $x(0) = 0$ the initial position of a trajectory is, the higher the overall intensity in the spectra will be. Thus, even if the number of trajectories that leave the core region is relatively small, the fact that their spectra are several orders of magnitude more intense than those obtained from the innermost trajectories gives rise to a masking of the latter's contribution in the dipole-length spectra. These findings are in agreement with the observations in Ref. [56], where a background in the HHG spectra was attributed to irreversible ionization at the end of the pulse, and in Ref. [57], where this background was

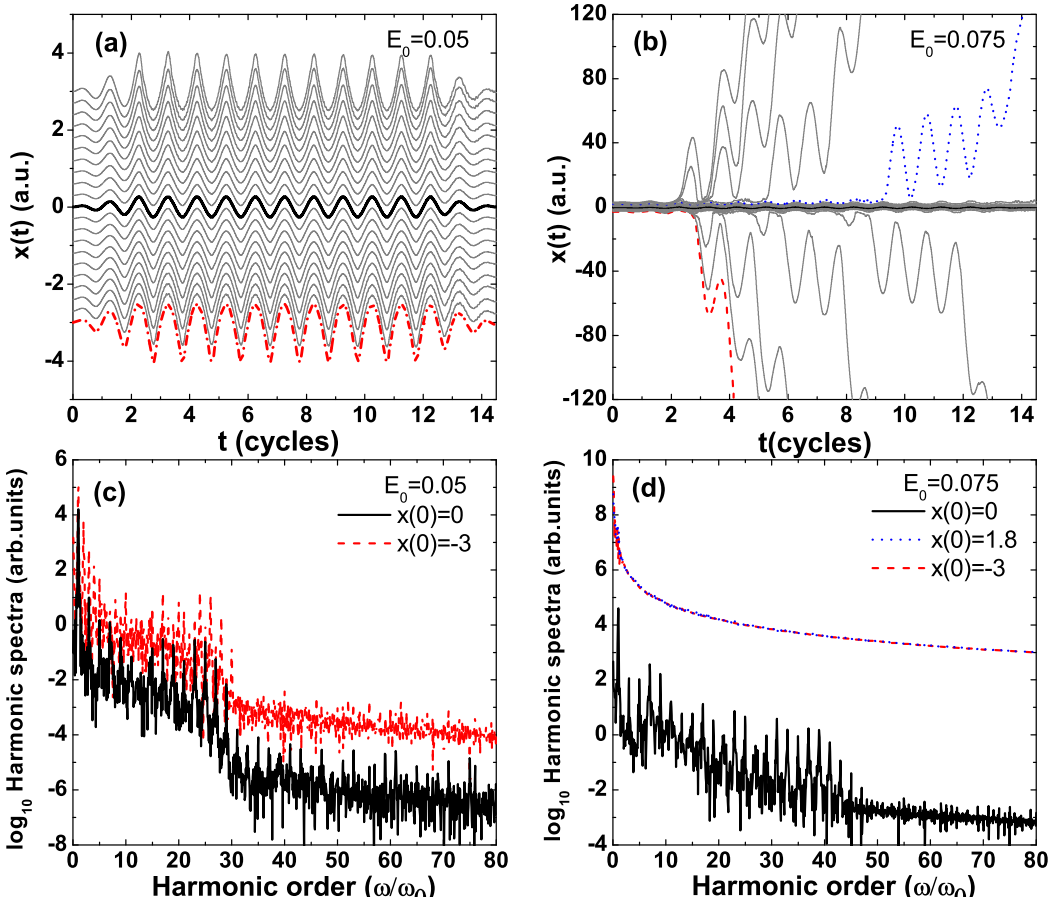

Figure 3.2: Upper panels: Bohmian trajectories obtained from the soft-core potential $V_{sc}(x)$ in a flat-top trapezoidal pulse with strength: (a) $E_0 = 0.05$ and (b) $E_0 = 0.075$. Lower panels: HHG spectra obtained from the trajectories in the upper panels. (c) Trajectories starting at $x(0) = 0$ (black solid line) and $x(0) = -3$ (red dashed line), for $E_0 = 0.05$. (d) Trajectories starting at $x(0) = 0$ (black solid line), $x(0) = 1.8$ (blue dotted line) and $x(0) = -3$ (red dashed line), for $E_0 = 0.075$.

attributed to the probability density near the edges of the integration box.
A blow-up shot of the expectation value of dipole acceleration and the central Bohmian trajectory in 2 laser cycles are shown in Fig. 3.3. From this figure, we can clearly see that both of the two time-dependent quantities follow the laser

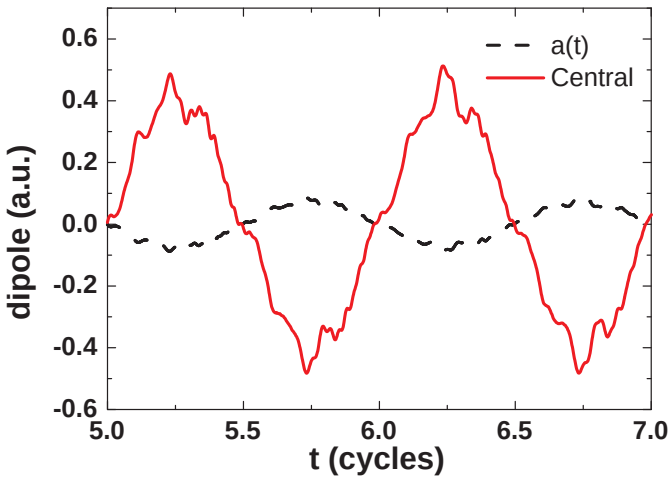

Figure 3.3: A blow-up of the central trajectory (red solid line) in Fig. 3.2(b) and the expectation value of the dipole acceleration computed from the TDSE (black dashed line) over two laser cycles using a long-range soft-core potential $V_{sc}(x)$ in a flat-top trapezoidal pulse (2.10) with strength $E_0 = 0.075$ and frequency $\omega_0 = 0.057$. Note that, formally, the central Bohmian trajectory $x_c(t)$ is equivalent to the time-dependent dipole length computed using only the innermost part of the time-dependent wave function.

field with a series of high-frequency oscillations. It is worth noting that, on average, the distance in time between adjacent peaks is around 0.03 times one laser cycle length. This roughly corresponds to a typical frequency of about $35\omega_0$, which is the cutoff frequency of the HHG spectrum. Through the computations of the dipole acceleration using both the TDSE [25] and other orbit-based methods [26–28, 48, 131], similar oscillations displayed in Fig. 3.3 have also been identified therein. However, this oscillating feature is not present in peripheral Bohmian trajectories. In fact, early studies [25] have identified that these oscillations, together with the strong localization feature of the dipole acceleration in the configuration space, are paramount for obtaining a plateau and a cutoff. These oscillations are related to the interference between the outgoing and in-

coming parts of the electronic wave packet, which overlap near the core.

More recent studies [47, 48] employing the adiabatic approximation also established similar findings, namely, part of the electronic wave function exhibits a highly oscillating phase structure. This phase may be associated with the classical action of an electron leaving and returning to the core, and contributes to the action $S(x,t)$ defining the Bohmian trajectories. Furthermore, studies using the HK propagator [26–28] and the CCS method [131] have identified that this highly oscillating structure can be associated with the quantum interference between different types of trajectories of electrons returning to the core.

Table 3.1: Eigenvalues of the untruncated soft-core (2.7) and two truncated (2.9) potentials. We shall refer to these models as first truncated, or $V_{tr}^{(1)}(x)$, for which $a_0 = 5.0$ and $L = 50$; and second truncated, or $V_{tr}^{(2)}(x)$, for which $a_0 = 1.0$ and $L = 7.55$. Note that, in principle, the number of eigenstates supported by the untruncated potential approaches infinity; in our calculations, we obtain a finite number of these because of the boundaries of the grid we use to solve the TDSE. Atomic units are used in this table.

n	untruncated	truncated 1	truncated 2
0	-0.66995	-0.66995	-0.65651
1	-0.27508	-0.27503	-0.17864
2	-0.15158	-0.15059	
3	-0.09276	-0.08714	
4	-0.06358	-0.05013	
5	-0.04552	-0.02390	
6	-0.03462	-0.00754	
⋮	⋮		
14	-0.00826		
15	-0.00707		
16	-0.00670		

A legitimate question is whether the above findings also hold for other model potentials. In order to address this, we truncate the soft-core potential according to Eq. (2.9). The parameters a_0 and L are chosen in two distinct ways. For the

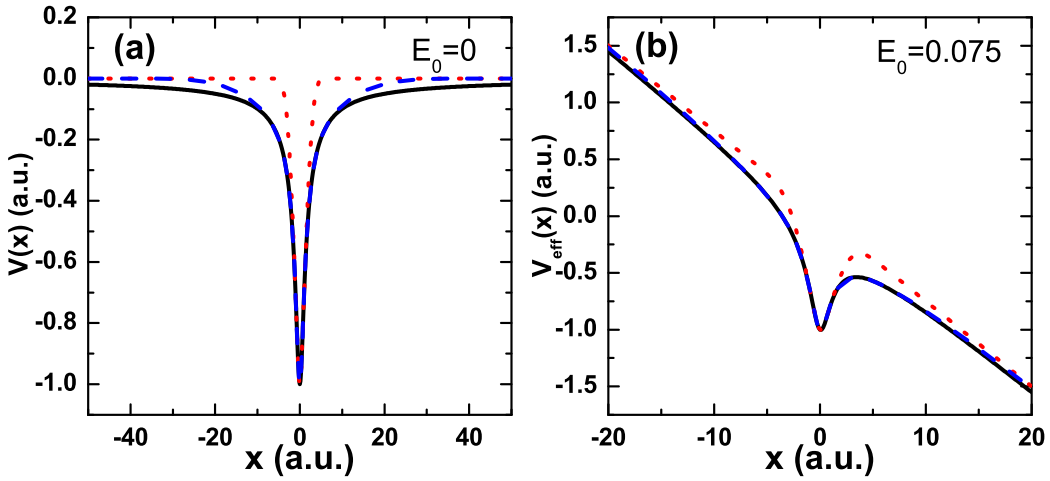

Figure 3.4: (a) Comparison between the soft-core model (2.7) (black solid line) and the truncated soft-core model (2.9) for two different values of the parameters a_0 and L. The blue dashed line denotes the truncated potential with $a_0 = 5.0$ and $L = 50$, while the red dotted line stands for $a_0 = 1.0$ and $L = 7.55$. In panel (b) we display the same potentials, but acted by the laser field at the maximum of its amplitude, which is taken as $E_0 = 0.075$.

truncated potential $V_{tr}^{(1)}(x)$, the long-range tail is eliminated, but the core region is kept practically unaltered, i.e., its field-free eigenenergies are quite similar to those of the long-range potential and it supports several weakly bound states. In contrast, the truncated potential $V_{tr}^{(2)}(x)$ is so short ranged that it can only support two bound states. Throughout, we keep the ground-state energy roughly the same. A list with the eigenvalues for these three potentials is given in Table 3.1.

These truncated potentials, together with the soft-core model (2.7), are illustrated in Fig. 3.4. Panels (a) and (b) show the field-free potential $V(x)$ and the effective potential barrier $V_{eff}(x) = V(x) - xE_0$ when the driving laser field reaches its peak value $E_0 = 0.075$. This field will be employed throughout this section, as it causes more irreversible ionization. For $V_{tr}^{(1)}(x)$, the potential well (core region) is essentially the same, while the long-range tail is significantly reduced. In the presence of the field, however, $V_{eff}(x)$ is practically not affected by the truncation. For the second truncated potential $V_{tr}^{(2)}(x)$, the width of the

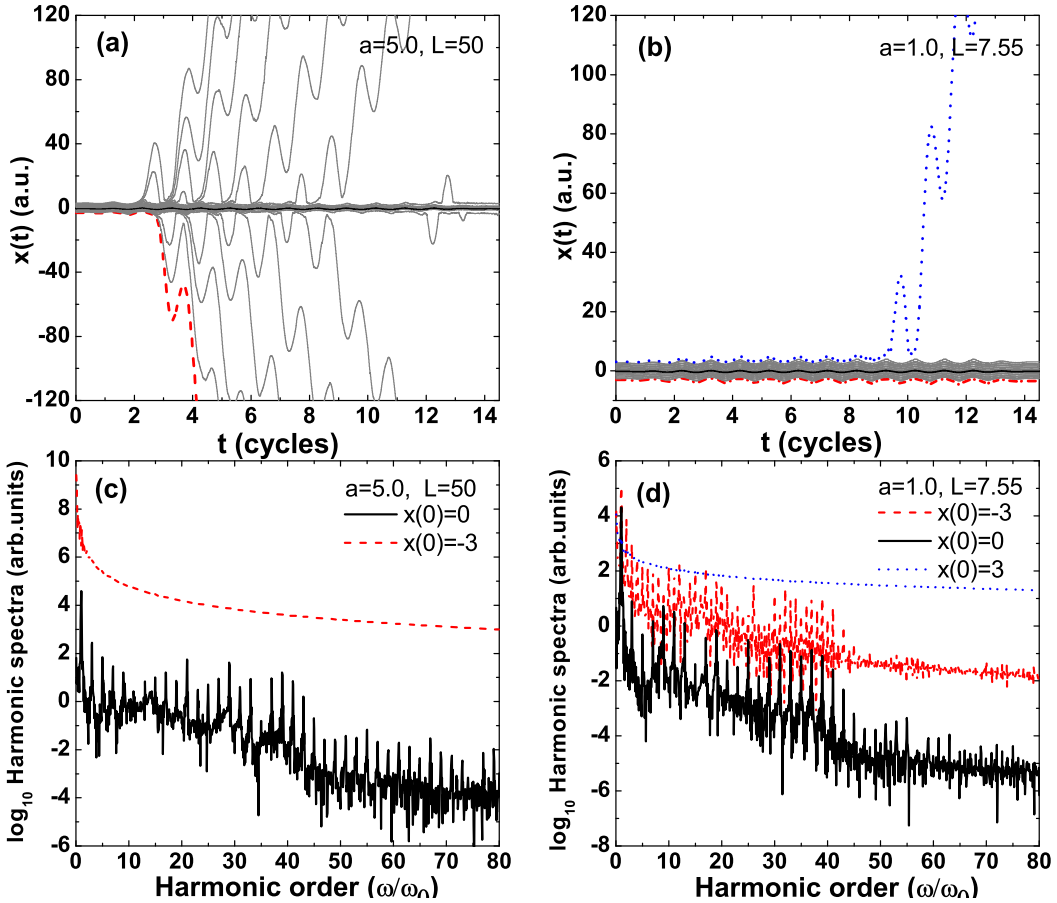

Figure 3.5: Upper panels: Bohmian trajectories obtained from the truncated soft-core potential $V_{sc}(x)$ with two sets of parameters: (a) $a_0 = 5.0$ and $L = 50$, and (b) $a_0 = 1.0$ and $L = 7.55$, in a flat-top trapezoidal pulse with strength $E_0 = 0.075$ and frequency $\omega_0 = 0.057$. Lower panels: HHG spectra corresponding to the trajectories selected from the upper panels. (c) Trajectories starting at $x(0) = 0$ (black solid line) and $x(0) = -3$ (red dashed line). (d) Trajectories starting at $x(0) = 0$ (black solid line), $x(0) = +3$ (dotted blue line) and $x(0) = -3$ (red dashed line).

potential well has decreased remarkably as well as the potential range. This leads to a much higher ionization barrier $V_{eff}(x)$.

In Figs. 3.5(a) and (b), we provide the outcome of the Bohmian-trajectory computation for $V_{tr}^{(1)}(x)$ and $V_{tr}^{(2)}(x)$, respectively. Fig. 3.5(a) shows that, if the core region is kept unaltered, but the long-range tail is truncated, the number of Bohmian trajectories that irreversibly leave the core is larger than that obtained for the long-range potential [see Fig. 3.2(b)]. This is related to $V_{tr}^{(1)}(x)$ being short ranged: once the trajectories are outside the core region, there is no potential tail attracting them towards it. This leads to an increase in the outward probability flow. These results, however, are strikingly different from those obtained for $V_{tr}^{(2)}(x)$. In this latter case, displayed in Fig. 3.5(b), these trajectories occur in a much smaller number, i.e., irreversible ionization is strongly suppressed. This happens as, for the long-range potential and for $V_{tr}^{(1)}(x)$, the many loosely bound states will be strongly coupled to the continuum in the presence of the field. Hence, they provide additional escape pathways for parts of the electronic wave packet. For $V_{tr}^{(2)}(x)$, these channels are absent. This outweighs the absence of a long-range tail.

Similarly to what has been observed for the long-range potential, the spectrum computed from the central trajectory exhibits a plateau followed by a sharp cutoff, while peripheral trajectories produce spectra which decrease monotonically, except for a single peak at the field frequency, $\omega = \omega_0$ [see panels (c) and (d)].

Another interesting question that arises here is that of the role played by the overall shape of the laser pulse. For that reason, we perform a Bohmian trajectory analysis for the long-range potential model (2.7), but assuming now that the driving field is a pulse whose envelope is given by Eq. (2.11).

The outcome of our computation is shown in Fig. 3.6, for two different laser intensities. In the left panels we display the dipole acceleration and the corresponding power spectra obtained from the TDSE, which will be employed as benchmarks. In general, the HHG spectra follow the cutoff law $I_p + 3.17U_p$. However, the resolution of the harmonic peaks is much worse than that obtained for the flat-top trapezoidal pulse. Indeed, only in the cutoff region it is possible to identify the harmonic peaks. This is expected as sharp harmonic peaks stem from the field periodicity: a flat-top trapezoidal pulse contains many identical cycles, whereas a

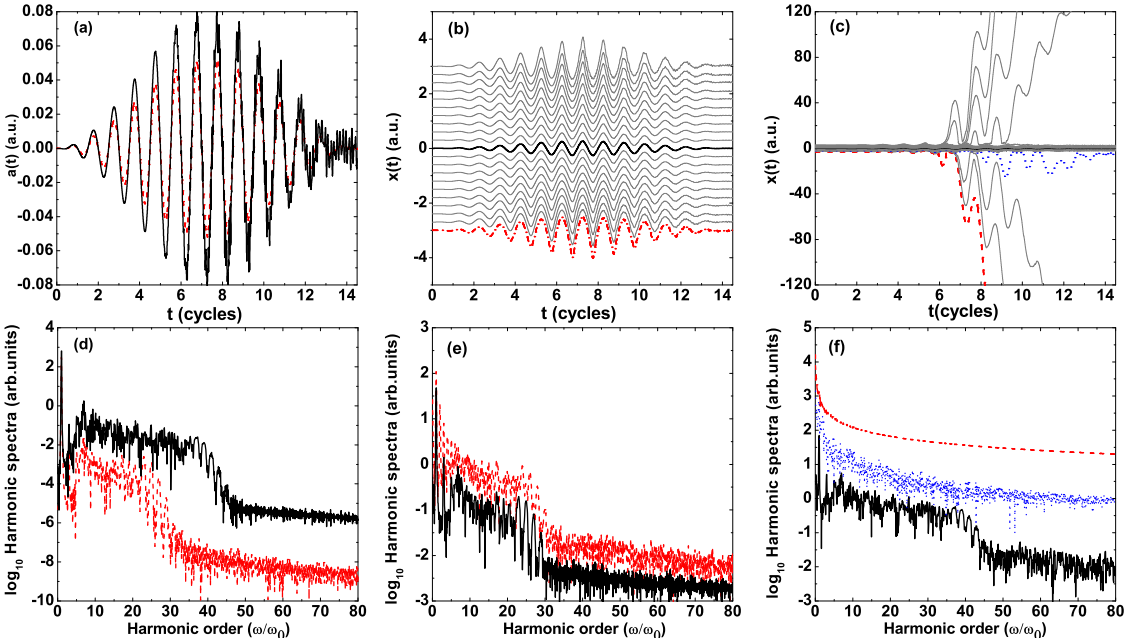

Figure 3.6: Left panels: Dipole acceleration [panel (a)] and the corresponding HHG spectra [panel (d)] computed from the TDSE for a soft-core potential $V_{sc}(x)$ in a $\sin^2$-shaped laser pulse (2.11) with frequency $\omega_0 = 0.057$, and intensities $E_0 = 0.05$ (dashed red line) and $E_0 = 0.075$ (black solid line). Panels (b) and (c): Bohmian trajectories obtained from the same atomic potential and laser field as those used in the left panels, with laser intensities $E_0 = 0.05$ and $E_0 = 0.075$, respectively. Panels (e) and (f): HHG spectra obtained from some trajectories selected from panels (b) and (c). Panel (e) shows the spectra from the trajectories starting at $x(0) = 0$ (black solid line) and $x(0) = -3$ (red dashed line), for $E_0 = 0.05$. Panel (f) exhibits spectra computed from the trajectories starting at $x(0) = 0$ (black solid line), $x(0) = 1.8$ (blue dotted line) and $x(0) = -3$ (red dashed line), for $E_0 = 0.075$.

sinusoidal pulse does not. The remaining panels of the figure exhibit the Bohmian trajectories obtained from this kind of pulse [panels (b) and (c)], with the corresponding spectra [panels (e) and (f)]. For sinusoidal driving pulses, we find the same pattern described previous, namely, a good qualitative agreement between the spectrum obtained from the dipole acceleration and that computed only using

the central Bohmian trajectory of the ensemble. Nonetheless, one could now ask the question of whether a quantitative agreement between the outcome of the TDSE and the results obtained from the Bohmian trajectory computations can be reached. This issue will be addressed in the next chapter.

3.2 Time-frequency analysis

In this section, we wish to investigate how the behavior of Bohmian trajectories compare to those of classical trajectories of an electron in a strong laser field. Furthermore, we would like to look more closely at the nonlocal transfer of information via the phase of the wave function in Bohmian trajectories. Specifically, we alter the flow of the time-dependent wave function far from the core, and assess whether this has an impact on the central trajectory.

With this purpose in mind, we will employ peripheral and central Bohmian trajectories from the long- and short-range potentials $V_{sc}(x)$ and $V_{tr}^{(1)}(x)$. To get a clear comparison we depict the probability density flow for both potentials in Fig. 3.7. This figure shows that the short-range potential $V_{tr}^{(1)}(x)$ [Fig. 3.7(b)] has a larger outward flow when compared to that of long-range potential $V_{sc}(x)$ [Fig. 3.7(a)]. This is because the probability density flow is restricted by the Coulomb tail. This confinement is not present in the short-range scenario as discussed in the previous section.

To extract such trajectories from the phase of the wave function, time-frequency maps need to be employed using the windowed Fourier transform technique (2.49). We have adopted the same window function as in Ref. [128] throughout, i.e., $\sigma = 1/(3\omega_0)$. Fig. 3.8 displays the time-frequency maps for the central and the peripheral Bohmian trajectories highlighted in Fig. 3.7. The upper and lower panels related to the long- and short-range potential $V_{sc}(x)$ and $V_{tr}^{(1)}(x)$, respectively. Note that for better comparison, we have scaled up the maps in panels (a) and (b) by 100 and those in the remaining panels by 10.

The time-frequency maps relating to the central Bohmian trajectory are shown in Figs. 3.8(a) and (b). At a high level, there is full agreement with the TSM,

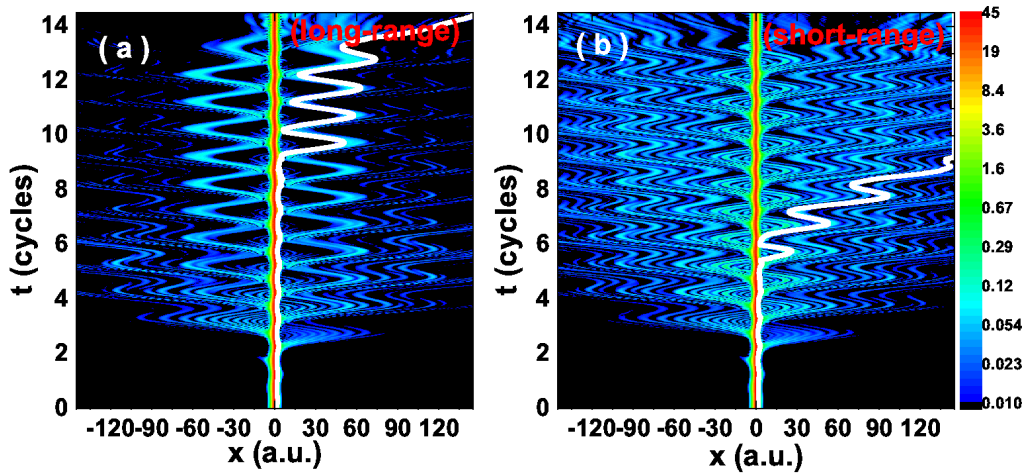

Figure 3.7: Time-evolution of the probability density distribution $|\Psi(x,t)|^2$ in the configuration space for the long-range soft-core potential $V_{sc}(x)$ [panel (a)] and the short-range truncated soft-core potential $V_{tr}^{(1)}(x)$ [panel(b)] in a flat-top trapezoidal field (2.10), with strength $E_0 = 0.075$ and frequency $\omega_0 = 0.057$. For clarity, the peripheral Bohmian trajectories starting at $x(0) = 1.8$ employed in the time-frequency maps of Fig. 3.8 are highlighted by the white curves in this figure. The intensity of the probability density distribution in panels (a) and (b) have been multiplied by 100.

regardless of whether the long- or the short-range potential is used. Indeed, these maps exhibit a series of arches which correspond to the classical return times of an electron ensemble leaving the core, propagating in the continuum and recombining with the parent ion. For clarity, we depict these return times using the curves in Fig. 3.8. Each point on these curves gives the return time of a classical electron in the field of a specific harmonic energy, and thus determine a classical orbit together with the start time t_0 [121]. As discussed in Section 2.3, some discrepancies, however, may occur depending on whether the binding potential has been neglected or included in the classical computations. In the latter case, there are more solutions for the return condition $x(t) = 0$, depending on whether the initial electron velocity is on the same or opposite direction to the field. These solutions have been recently discussed in Ref. [132] within a Coulomb-corrected

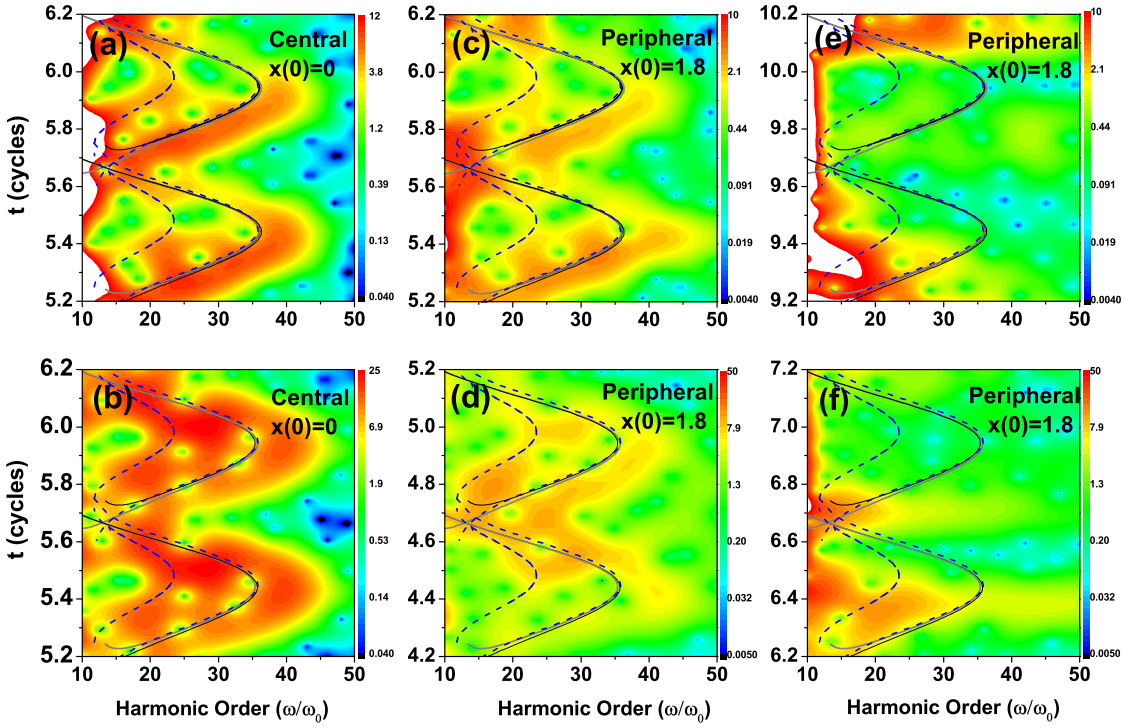

Figure 3.8: Time-frequency maps [using (2.49)] of the central Bohmian trajectory [panels (a) and (b)], and the peripheral trajectory starting at $x(0) = 1.8$ [panels (c) to (f)] for one-dimensional model potentials in a flat-top trapezoidal field (2.10) with frequency $\omega_0 = 0.057$ and strength $E_0 = 0.075$. In panels (a), (c) and (e) the long range soft-core potential $V_{sc}(x)$ (2.7) has been used, while in panels (b), (d) and (f) the truncated potential $V_{tr}^{(1)}(x)$ (2.8) has been considered. The solid and the blue dashed arches in the figure are related to the outcome of the classical-trajectory computations with and without binding potential, respectively. In the classical-trajectory computations with binding potential, the electron with escape velocity v_0 according to section 2.3.1 is considered. The black thin lines account for the solutions obtained using positive values of v_0, while the gray thick lines correspond to the solutions obtained for negative v_0. In the middle panels we consider a temporal window for which the peripheral trajectories are still close to the core [between the 5th and the 6th cycle for $V_{sc}(x)$ and between the 4th and the 5th cycle for $V_{tr}^{(1)}(x)$], while in the right panels we take a time interval for which they have left this region [between the 9th and the 10th cycle for $V_{sc}(x)$ and between the 6th and the 7th cycle for $V_{tr}^{(1)}(x)$].

SFA framework. The lower parts of the arches correspond to the "short" trajectories, along which each classical electron returns before the field crossing, and the upper parts of the arches correspond to the "long" trajectories, along which it returns after the crossing. We find that in the time-frequency maps computed for the long-range potential, the lower parts of the arches are more concentrated. This indicates that contributions to the time-frequency profile is more dominated by the the short classical trajectories. We also observe faint second arches extending up to harmonic energy of approximately $I_p + 1.5U_p$. These arches are associated with even longer classical trajectories with excursion times $t - t_0$ in the order of one and a half cycle.

The flow of the wave function far from the core, can be altered by truncating the tail of the long-range potential. This will have an impact on the time-frequency profiles obtain for the central Bohmian trajectory, which can be seen from Fig. 3.8. Indeed, the upper parts of the arches in these maps will become more intense, which implies that longer classical trajectories will now have more prominent contributions, in agreement with that observed in the literature [128]. From the above we can conclude that, the phase information contained in the innermost part of the wave function can be changed non-locally by altering the flow far away from the core.

The time-frequency profiles of the peripheral Bohmian trajectory starting at $x(0) = 1.8$, depicted in the remaining panels of Fig. 3.8, behave in a rather different way. We have chosen the initial and final times so that the Bohmian trajectories in question are still within, or have just left the core region. An illustration of how the probability flow behaves at such times is provided in Fig. 3.7, for comparison. In case the trajectory is still close to the core, arch-like structures may be identified in the time-frequency maps, as shown in Figs. 3.8(c) and (d), which, once more, correspond to the return times predicted by the TSM. Nonetheless, these structures are more blurred than those observed for the central trajectory. As the Bohmian trajectories move away from the core region, these structures degrade very quickly, and the agreement with the TSM is lost. This can be observed in Figs. 3.8(d) and (f).

3.3 Conclusions

Our studies utilising Bohmian trajectories illustrate that the HHG spectra are primarily produced by the innermost part of the wave function. In fact, a single Bohmian trajectory, the trajectory that starts at $x_0 = 0$, contains all the information necessary to obtain the HHG spectra. This is a stronger statement than that may be concluded using the dipole acceleration, namely, the overlap between the continuum and bound part of the wave function in close vicinity to the core region is important. For peripheral Bohmian trajectories, the situation is markedly different. As long as they perform an oscillatory motion near the core, the plateau and the cutoff is present. If, however, they leave this spatial region, the corresponding spectra will only consist of a fundamental and uniform background. Moreover, the further from $x(0) = 0$ the initial position of a trajectory is, the higher the overall intensity in the spectra will be. Different kinds of driving-field intensities, pulse shapes and binding potentials are considered in order to substantiate that these results are general.

The key to fully understand the results above is to bear in mind that a Bohmian trajectory is a nonlocal entity. In other words, it better resembles a "slice" of the wave function rather than a trajectory in the classical sense. In fact, a Bohmian trajectory only exhibits behavior consistent with those of a classical trajectory in very limited cases, such as for coherent states and very specific ranges of the Mandel parameter [133]. In all the other cases, a Bohmian trajectory evolves upon action of the wave function, which contains information about not only local variations of the potential functions but also global changes of the quantum phase. This implies that the Bohmian trajectory localized in the immediate vicinity of the core may still contain information about the continuum and bound dynamics. Any alterations in the wave function, regardless of being made far from or close to the core, will be transferred nonlocally to the central trajectory via its phase.

This is consistent with the fact that, in quantum and semiclassical models, the trajectories related to the TSM are always extracted from the phase of the wave function. This holds in the commonly used SFA, when these trajectories are obtained from the steepest descent method [20], as well as in other techniques,

such as the HK propagator [26, 28] and the adiabatic approximation [47, 48]. Moreover, our time-frequency maps demonstrate that this phase behaves as an ensemble of unbound classical trajectories. The built up of this phase is affected by any changes in the flow of the wave function far from the core. Our results are also in agreement with the well-known fact that, in spatial terms, HHG takes place at the core. In fact, our time-frequency analysis of peripheral Bohmian trajectories have shown degradation of the above-mentioned profile when the probability density flow moves further away from the core region.

Lastly, our studies also demonstrate why the SFA provides highly satisfactory results. The SFA reduces the influence of the core to a single point, i.e., $x = 0$, and approximates the continuum by Volkov waves. This is an appropriate proxy since the most relevant part of the wave function for HHG is strongly localized. Additional evidence for this resemblance between Bohmian trajectory and the SFA will be provided in the next chapter.

Chapter 4

Bohmian trajectory analysis of HHG: ensemble averages, nonlocality and quantitative aspects

In the previous chapter we have shown that the time-frequency map from the central Bohmian trajectory can be associated with an ensemble of classical trajectories leaving and returning to the core. A legitimate question is which regions of the core must be considered in order to obtain quantitative agreement between the Bohmian-trajectory simulation and the TDSE. As Bohmian trajectories are extracted directly from the TDSE, one expects that both methods should eventually lead to identical outcomes. This leads to the question of whether it is sufficient to include the immediate vicinity of the innermost trajectories or the whole core should be considered?

Furthermore, recently, it has been shown that the short-range potential overestimates the contributions of the long TSM trajectories, as compared to the long-range potential [128]. This is attributed to the spatial extension of the core and to the Coulomb tail. Can we find similar effects using Bohmian trajectories? If so, how can they be understood in the present framework?

Moreover, in the previous chapter we have found that the central Bohmian trajectory is affected by the probability flow far from the core and suggested that this is due to the nonlocal transmission via the phase of the wave function. However, a more detailed study of this nonlocality and how this phase builds up has not been performed.

In addition, we found that the spectrum obtained from the Bohmian trajectory located at the innermost part of the core is qualitatively very similar to that of the dipole acceleration, where a clear plateau and cutoff position is observed at $I_p + 3.17U_p$, rather than the dipole length which normally gives a large background that blurs the plateau and the cutoff. However, in strong-field physics, a wide spread way of eliminating the background introduced by the dipole length in the HHG spectrum is to apply a Hanning filter. A question is what is the underlying meaning of this filter, can an intuitive explanation be obtained from Bohmian trajectories?

In this chapter, we address the questions mentioned above. This chapter is organised as follows. In Section 4.1, we use ensembles of Bohmian trajectories to study the HHG spectrum and show which region is necessary for obtaining the quantitative agreement with that from the TDSE. In Section 4.2, we relate the Bohmian trajectories to those obtained from the SFA using time-frequency analysis. In Section 4.3, by changing the positions of the absorber, we show how the dynamics far from the core affects the central trajectory nonlocally via the phase of the wave function. After that, in Section 4.4, we study the effective dynamics induced by a numerical filter. The main conclusions of this chapter will be provided in Section 4.5.

4.1 HHG spectrum from ensemble Bohmian trajectories

In the previous chapter we have discussed the behavior of individual Bohmian trajectories and their spectra. In this chapter we focus on ensemble average according to Eq. (2.26). If the range of initial conditions sufficiently spans the

whole spatial extent of the wave function probability $|\Psi(x,0)|^2$, this average is formally equivalent to the expectation value of the dipole acceleration (2.24).

Specifically, we investigate which regions within the core must be included for a *quantitative* agreement between the outcome of the TDSE and that from the Bohmian trajectory computations to be reached. For this purpose, we have considered a set of initial conditions obtained from uniformly generated random numbers within a certain interval $[-x_c, x_c]$, symmetric with regard to the origin $x = 0$. These random numbers are multiplied by weights, which are chosen in such a way that the probability density related to the ground state of the soft-core potential, $|\psi_0(x)|^2$, is mimicked. We have gradually varied the range of the aforementioned random-number distribution by changing the boundary x_c, until a quantitative agreement from the TDSE is reached. The total interval has been chosen in such a way that the probability density related to the initial wave function, $\Psi(x,0)$, is recovered up to over 99.8%. For the parameters employed in this work, we have verified that all the relevant probability density is incorporated if we take $x_c = 4.102$. This amounts to fourteen intervals at each side of the origin, $x = 0$, and around $N \approx 1000$ random numbers in total. Each of these numbers thus corresponds to the initial condition for a Bohmian trajectory. These results are displayed in Fig. 4.1 for the time-dependent dipole acceleration computed using the Bohmian trajectory average [Eq. (2.26)]. Overall, the time dependence of all the distributions considered is very similar. What is affected is the amplitude of the time-dependent acceleration. If only the acceleration along the central trajectory is taken (red lines in the figure), we see that this amplitude is up to five times larger than that determined by the acceleration computed using the TDSE. The main effect of increasing the range of the integration around this central trajectory is to decrease this amplitude. Indeed, for both intensities a quantitative agreement is found for $x_c = 2.344$, which corresponds to about 96% of the total probability density. However, if one is interested in a qualitative comparison it is fully legitimate to assume that, as an approximation, the core is a source term located around $x(0) = 0$, as done in the SFA-based models.

In Fig. 4.2, we investigate how increasing the number of ensembles trajectories influences the HHG spectra. Due to the above-mentioned difference in amplitude,

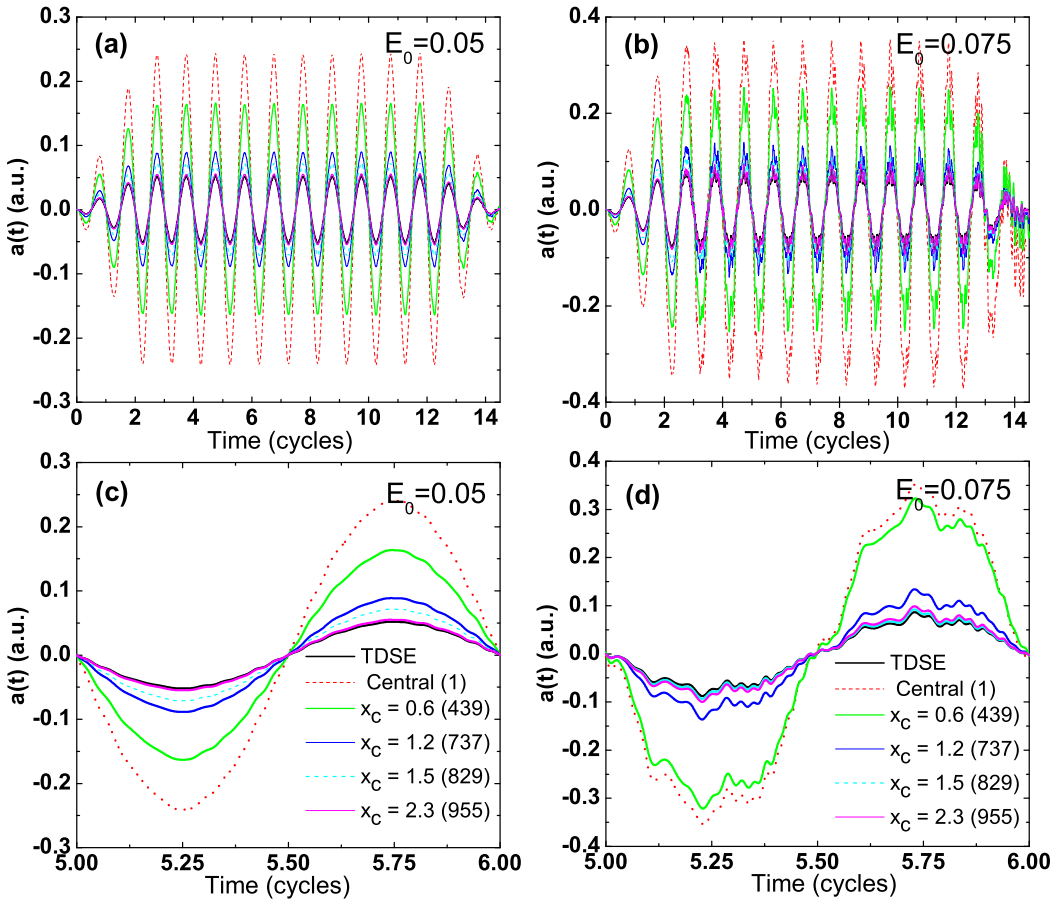

Figure 4.1: Dipole acceleration obtained from a series of sets of Bohmian trajectories randomly distributed within the interval $[-x_c, x_c]$ for a long-range soft-core potential $V_{sc}(x)$ in the external flat-top trapezoidal laser field with frequency $\omega_0 = 0.057$ and two intensities: (a) $E_0 = 0.05$ (left panels) and (b) $E_0 = 0.075$ (right panels). The remaining parameters are the same as those in Fig. 3.2. Enlargements of the behavior of this quantity within one cycle of the pulse are given respectively in panels (c) and (d). The different values of x_c used in our simulations are labeled with different types of colors/line-styles. For details, see the legend in the lower panels (in parenthesis, we provide the total number of Bohmian trajectories used in each case). In all cases, the black sold line represents the result obtained from the TDSE and the red dashed line the result from the central Bohmian trajectory.

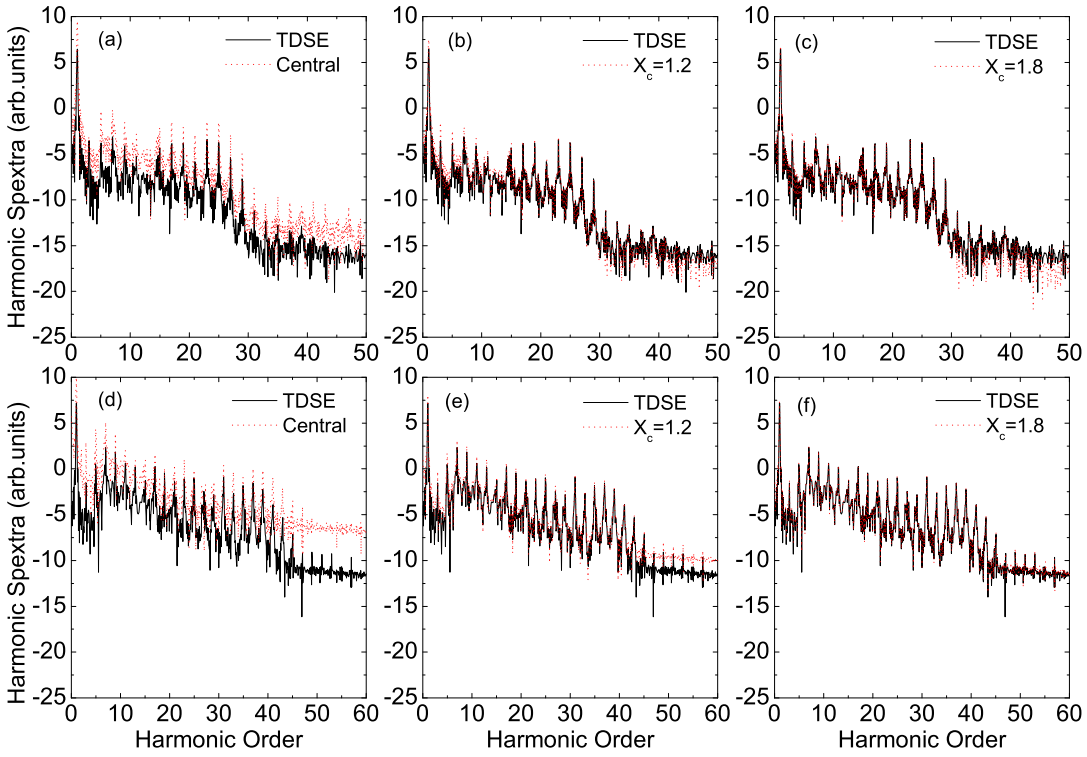

Figure 4.2: HHG spectra of the dipole acceleration obtained from the TDSE (black solid line) and a series of Bohmian trajectories (red dashed line) in which the range of initial conditions have been restricted to the intervals $[-x_c, x_c]$, with: Panels (a) and (d): $x_c = 0$ (central trajectory); panels (b) and (e): $x_c = 1.2$; panels (c) and (f): $x_c = 1.8$. In the upper and lower rows we show the results for the soft-core potential $V_{sc}(x)$ in the flat-top trapezoidal laser field with frequency $\omega_0 = 0.057$ and intensities $E_0 = 0.05$ (upper panels) and $E_0 = 0.075$ (lower panels), respectively.

the harmonics in the spectrum from the central trajectory are several orders of magnitude higher than those from the TDSE [see Figs. 4.2(a) and (d)]. As the spatial range is increased, a reasonable quantitative agreement is reached for the harmonics in the cutoff region. This is already true if 75% of the overall probability density is considered ($x_c = 1.172$). For the below-threshold and low-plateau harmonics, a good agreement is reached only if 90% of the total probability den-

sity is taken ($x_c = 1.8$). Physically, this is consistent with what is known from the strong-field models, i.e., the high-plateau and cutoff harmonics can be reasonably modeled by the SFA, while the lower harmonics are much more influenced by the internal structure of the system, such as excited states.

However, even for the cutoff region an ensemble of Bohmian trajectories must also be taken if quantitative agreement with the TDSE is to be achieved. This can be attributed to the fact that, quantum mechanically, there is a certain spread in the initial position of the electron, which must be considered. Quantitative agreement with the TDSE near the cutoff has also been obtained for an improved SFA model [134], where the steepest-descent method has not been performed, but the continuum-to-continuum transitions have been used. Physically, these modifications introduce a spread in position and momentum. In the TSM view, this suggests that the electron is no longer required to return exactly to the site of its release or leave with vanishing momentum.

4.2 Time-frequency analysis of ensemble trajectories

In Fig. 4.3, we display time-frequency maps obtained for the dipole acceleration considering the central Bohmian trajectory, an ensemble of around 1000 Bohmian trajectories and, for consistency, the expectation value of the dipole acceleration from the TDSE (left, middle and right panels, respectively). For comparison, superimposed to the time-frequency maps, we also display the real parts of the return times t obtained from the HHG transition amplitude in the SFA using the steepest descent method (Section 2.3.2). The times t, together with their ionization times t', are the solutions of the SPEs [Eqs. (2.46)-(2.48)]. The trajectories obtained from these solutions are widely known as quantum orbits [117]. Their real parts are related to the classical trajectories of an electron in a laser field, and form arch-like structures in the time-frequency maps, which merge at the cutoff. The upper part of each curve is related to the "long orbit", along which the electron leaves earlier and returns later, while the lower part of the curve is associated with the "short orbit" (for a similar discussion of these orbits

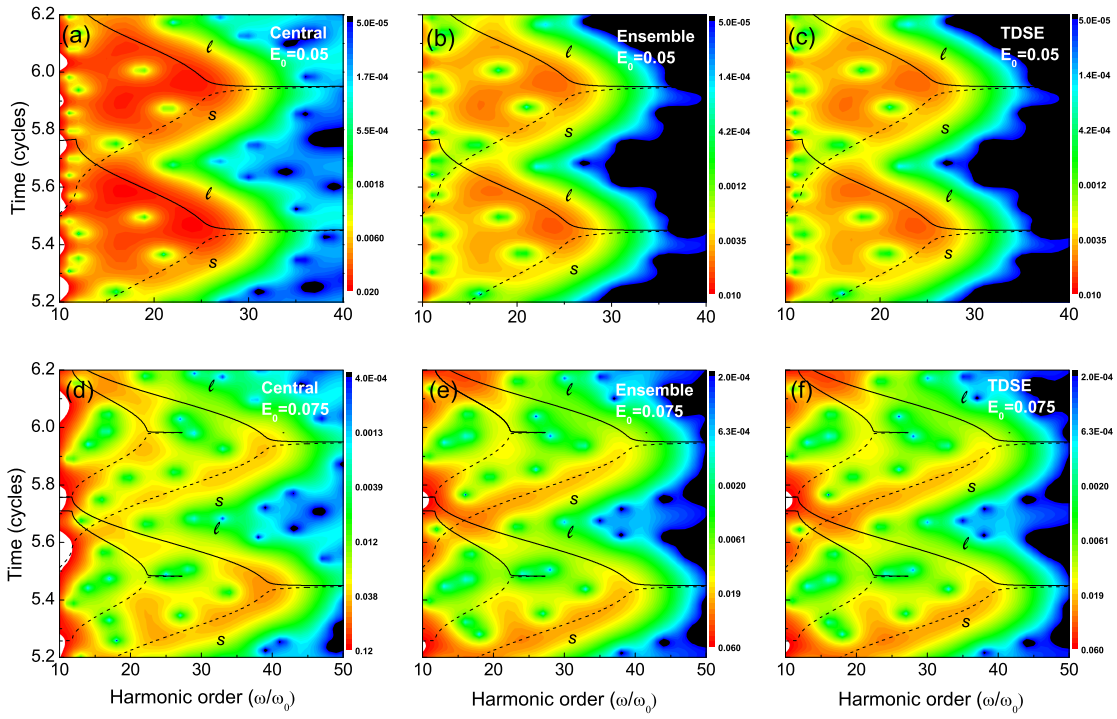

Figure 4.3: Time-frequency maps as functions of the harmonic order computed using the Gabor transform Eq. (2.49) of the dipole acceleration for soft-core potential $V_{sc}(x)$ in flat-top trapezoidal fields of frequency $\omega_0 = 0.057$ and intensities $E_0 = 0.05$ [panels (a) to (c)], and $E_0 = 0.075$ [panels (d) to (f)]. In panels (a) and (d), only the central Bohmian trajectory is considered in order to compute the acceleration $\overline{a}_B(t)$, while in panels (b) and (e) an ensemble of 955 Bohmian trajectories is taken. In panels (c) and (f), we display the results obtained from the TDSE employing the expectation value of the dipole acceleration [Eq. (2.24)]. The black lines in the figure indicate the real parts of the return time t obtained from the SFA, according to Eqs. (2.46)-(2.48). In such equations, we have taken the ionisation potential to be the absolute value of the ground-state binding energy ($I_p = 0.66995$). The dashed lines and the letter s indicate the short orbits, while the solid lines and the letter ℓ indicate the long orbits. In the lower panels, there is a second set of arches at lower energy. These arches correspond to a longer pair of return times. The time is displayed in units of the field cycle, and the yield has been plotted in a logarithmic scale.

can be found in Ref. [120]). In all panels of Fig. 4.3, such arch-like structures are present, both for the ensemble average (2.26) and for the acceleration along the central trajectory. These structures are particularly clear if the driving-field intensity is such that the system is in the tunneling regime [Fig. 4.3(d)]. In this case, the effect of taking an ensemble is that the relative contribution of the long orbit, with regard to that of the short orbit, is suppressed [see Fig. 4.3(e)].

This is consistent with other results in the literature, in which different weights between the signals related to the short and long trajectories have been observed in time-frequency maps [71, 128, 135] and intensity-reciprocal intensity maps [136]. In all cases, there seems to be a strong correlation between the overenhancement of the long trajectory and the core region being strongly localized. An enhancement of the long orbit occurs for short-range potentials, if compared with their long-range counterparts [71, 128], or in the SFA, if compared with the TDSE [135, 136]. This overenhancement is particularly extreme if the steepest-descent method is employed in the SFA [136].

Physically, this may be understood as follows. First, the long orbit is associated with a higher degree of wave packet spreading, which means that it will be more sensitive with regard to spatial propagation, and the uncertainty introduced by the initial momentum and position spreads. If the steepest descent method is used in the SFA, these initial spreads are neglected and the long orbit is over enhanced. Second, for a short-range potential, the initial wave packet is highly localized, the effective barrier is very steep, and there is no Rydberg series. This implies that (1) there will not be a strong mixing between excited states and the continuum in the presence of the field and (2) it will be more difficult for an electron to reach the continuum along the short orbit, whose start times are farther away from the field peak. This will lead to over enhanced contributions of the long orbits in the time-frequency maps.

In the present framework, using only the central Bohmian trajectory or small ensembles around it means that a high degree of localization is being imposed upon the core. This shares similarities with the SFA, for which only a single point at $x = 0$ is used to approximate the core; and with short-range potentials, for

which there are no weakly bound states. In order to reproduce features that depend on the internal structure of the core and to account for its spatial extension, one must employ larger ensembles of Bohmian trajectories (see our discussion of Fig. 4.2). The less localized the initial wave packet is, the more trajectories one must consider.

For lower intensities, in the multiphoton regime, the above mentioned arch-like features are more blurred, as shown in Fig. 4.3(a), in agreement with the results in Ref. [128]. This blurring is related to the appreciable acceleration of the electronic wave packet outside the time intervals predicted by the TSM. These features are present in the SFA if the steepest-descent method is not used [137].

4.3 Altering the absorber

The above-stated results confirm that the phase of the wave function, which is extracted either from the TDSE or from the Bohmian trajectories using time-frequency analysis, mimics the behavior of a classical electron leaving and returning to the core. This shows that the central Bohmian trajectory, even if it is spatially confined, may contain bound and continuum information, and it is not a trajectory in the classical sense. Indeed, it is more as if one were "slicing" the time-dependent wave function, and analyzing how this "slice" evolves near $x = 0$. Based on this line of argument, one expects that, if the phase of the whole wave function is somehow altered or degraded, this will be transmitted non-locally to the central trajectory. Evidence for this nonlocality has been provided in the previous chapter, using long- and short-range potentials. Below we will investigate in more detail how this phase builds up in configuration space.

We will disrupt the propagation of the wave function outside of the core region but avoid absorption of the probability flow within the region for which the dipole acceleration is significant, by moving the absorber from near the boundaries of the integration box to ranges of the coordinate x within the excursion amplitude of a classical electron in the field. This excursion amplitude is given by $\alpha = E_0/\omega_0^2$. The lowest absolute value of x_1 in Eq. (2.21) is around 5 (according to section 4.1, quantitative agreement with the TDSE are expected for orbits starting in the

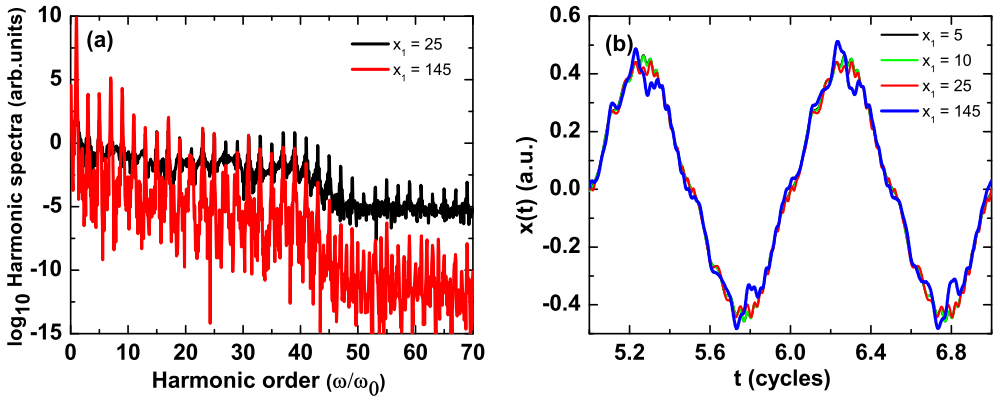

Figure 4.4: Panel (a): HHG spectra computed from the central Bohmian trajectory of the soft-core potential $V_{sc}(x)$ in a flat-top trapezoidal field by placing the absorber at $x_1 = 145$ and $x_1 = 25$. Panel (b): Central Bohmian trajectory as a function of time over two laser cycles, for absorbers placed at varying distances x_1. The frequency and strength of the laser field is $\omega_0 = 0.057$ and $E_0 = 0.075$, respectively. For the parameters employed in this figure, the classical excursion amplitude is $\alpha = 23$.

interval $x \in [-2.3, 2.3]$). For clarity, in Fig. 4.4, we show that, for an absorber placed slightly beyond α, there is already substantial degradation in the spectra, but the plateau and the cutoff are still present [panel (a)]. However, the central Bohmian trajectories, as a function of time, from the absorbers located at different positions look very similar [panel (b)].

The time-frequency maps obtained in this way are presented in Fig. 4.5 for the higher strength employed in Fig. 4.3. In this figure, the patterns associated with the longer orbits become increasingly suppressed and deteriorate as the absorber is moved towards the core. For instance, if the absorber is placed slightly beyond the classical excursion amplitude, the arch corresponding to the longer SFA return times, which extends to around the 25^{th} harmonic, becomes fainter. This holds for the time-resolved spectra of the central Bohmian trajectory [Fig. 4.5(a)], the acceleration along the central trajectory [Fig. 4.5(b)] and the outcome of the TDSE [Fig. 4.5(c)]. The same behavior is observed for the feature associated

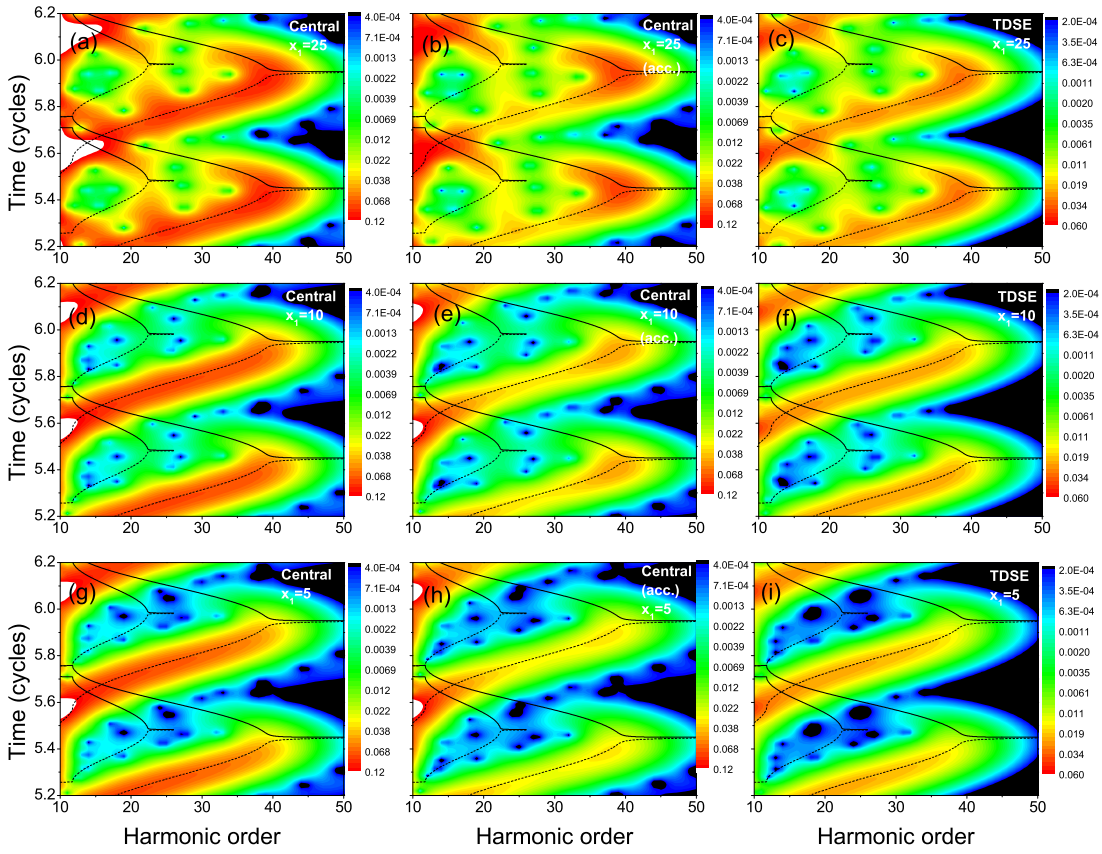

Figure 4.5: Time-frequency maps as functions of the harmonic order computed using the Gabor transform [Eq. (2.49)] for a soft-core potential $V_{sc}(x)$ in a flat-top trapezoidal field with frequency $\omega_0 = 0.057$ and strength $E_0 = 0.075$. For the upper, middle and lower panels we have placed the absorber given by Eq. (2.22) at $x_1 = 25$ [panels (a) to (c)], $x_1 = 10$ [panels (d) to (f)] and $x_1 = 5$ [panels (g) to (i)], respectively. In the left, middle and right panels we have computed the Gabor transforms of the central Bohmian trajectory [panels (a), (d) and (g)], of the dipole acceleration along the central Bohmian trajectory [panels (b), (e) and (h)], and of the dipole acceleration obtained from the TDSE [panels (c), (f) and (i)], respectively. The black lines in the figure indicate the real parts of the solutions of the SPEs for the return time t. The dashed lines correspond to the short orbits in a pair, while the solid lines give the long orbits.

with the long trajectory belonging to the shortest pair. If the absorber is made active slightly below the middle of the classical excursion amplitude ($x_1 = 10$) of the electron, the above-mentioned features will be very weak, as shown in the middle panels of Fig. 4.5. For an absorber starting immediately after the core region ($x_1 = 5$), all the features in the time-frequency maps associated with the longer trajectories are substantially reduced [Figs. 4.5(g) to (i)]. Fig. 4.5 shows that the probability density that leaves the core region plays a very important role in influencing the phase of the wave function. Throughout, the absorber is extremely smooth, so the probability density flow is disrupted but not eliminated and full absorbtion only occurs for the boundaries. For a sharper absorber, the signal related to the short orbit would also be eliminated.

4.4 Effective dynamics induced by numerical filters

Finally, we will address the effective dynamics induced by filters or window functions, which are often used to stress some particular aspects in the corresponding spectra. For example, a widespread way of eliminating the background introduced by the dipole length in the harmonic spectra is to apply a Hann (Hanning) filter,

$$w(t) = 0.5 \left[1 - \cos\left(\frac{2\pi t}{\tau_f}\right)\right] = \sin^2\left(\frac{\pi t}{\tau_f}\right). \tag{4.1}$$

This filter is specially useful to force (artificially) the time-dependent function $\mathscr{D}(t)$ and its derivative to start at zero and decay to zero at the end of the simulation in a smooth fashion. With it, Eq. (2.22) reads as

$$I_w(\omega) = \left| \int \mathscr{D}(t) w(t)\, e^{-i\omega t} dt \right|^2. \tag{4.2}$$

A legitimate question related to this kind of spectra is therefore if they can be associated with a certain dynamical behavior of the system. If $\mathscr{D}(t)$ refers to the expectation values $\bar{x}(t)$ or $\bar{a}(t)$ of the dipole length or acceleration, then the effective values $\bar{x}_{\text{eff}}(t) = w(t)\bar{x}(t)$ and $\bar{a}_{\text{eff}}(t) = w(t)\bar{a}(t)$ say very little about the behavior of an effective wave function that suits such values. In contrast,

if $\mathscr{D}(t)$ refers to the Bohmian trajectories, one can reconstruct effective dynamics, since (i) $x_{\text{eff}}(t) = w(t)x(t)$ is a trajectory (actually, just the product of the actual Bohmian trajectory and the window function) and, as seen above, (ii) an ensemble of such trajectories would allow us to understand how the effective wave function (or probability density) would flow in the configuration space.

In order to show the reconstruction procedure, in Fig. 4.6 we have considered two trajectories for each of the cases shown in Fig. 3.2. For lower intensities, the trajectories start and end at their initial positions and therefore the window function just stresses this fact. Note that $w(t)$ produces a reset of the trajectory to zero and therefore the effective trajectory has to be shifted so that the initial position coincides with that of the respective Bohmian trajectory. The effect of $w(t)$ on the Bohmian trajectory is just to make it evolve around the shape of this function [see the trajectory starting at $x(0) = -3$, for example, in panel (a)]. In the case of low strength and trajectories starting at $x(0) = 0$, the spectra look essentially the same [see panel (c)]. If the initial position is $x(0) \neq 0$ [such as $x(0) = -3$, displayed in panel (e)], the filter leads to a visible reduction in the background. Physically, this happens because of the constraint imposed by the filter upon the final position $x_i(\tau_f)$ of the Bohmian trajectory $x_i(t)$ in question. This reduction can be easily spotted in the frequency region beyond the cutoff.

For higher driving-field intensity, however, the filter leads to more dramatic effects. In the case of confined trajectories, the same comments as for low intensities hold, as seen in panel (b) regarding the trajectory dynamics, or in panel (d) regarding their spectra (although the background is remarkably lower). For the trajectories associated with irreversible ionization, though, dynamics is very different: the Bohmian trajectories go out of the core region, but the effective trajectories obtained with filter come back to their initial positions after undergoing longer excursions far away. Accordingly, not only the corresponding spectra display more interference features, but also the continuous background decreases in several orders of magnitude, as seen in panel (f).

In Figs. 4.7, we show the whole ensemble reconstructed trajectories and time-dependent probability density distribution of the wave function in the configura-

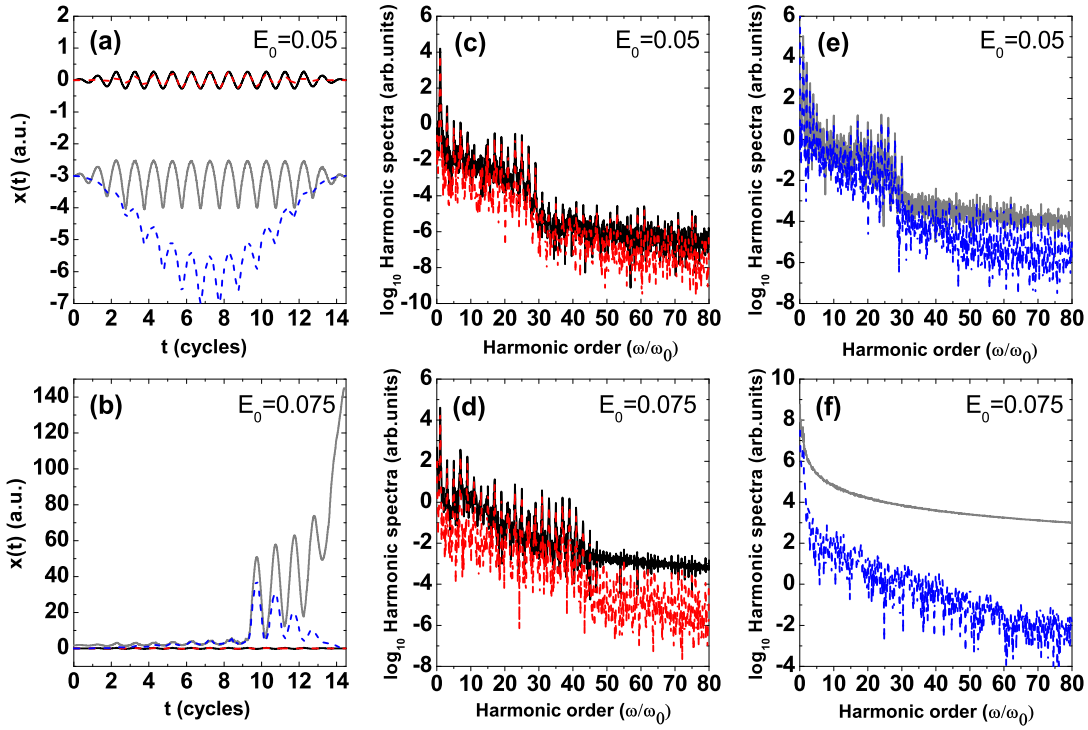

Figure 4.6: Bohmian trajectories obtained from the soft-core potential $V_{sc}(x)$ in a flat-top trapezoidal field with frequency $\omega_0 = 0.057$ and intensities: (a) $E_0 = 0.05$ (upper panels) and (b) $E_0 = 0.075$ (lower panels). In panel (a) the trajectories start at $x(0) = 0$ (black solid line) and $x(0) = -3$ (gray dotted line); the respective reconstructed trajectories with Hanning filter are denoted with the red dashed line and the blue dash-dotted line. In panel (b) the trajectories start at $x(0) = 0$ (black solid line) and $x(0) = 1.8$ (gray dotted line); the respective reconstructed effective trajectories are denoted with the red dashed line and the blue dash-dotted line. The HHG spectra for each trajectory and its effective homologous are given in the right four panels. For the low field strength ($E_0 = 0.05$): (c) for $x(0) = 0$ and (e) for $x(0) = -3$. For the high field strength ($E_0 = 0.075$): (d) for $x(0) = 0$ and (f) for $x(0) = 1.8$. Colors/line-styles are in correspondence with the trajectories displayed at the respective left panels.

tion space from Bohmian trajectories. Once again if the filter is present, however, they are forced back to their initial position after undergoing longer excursions far

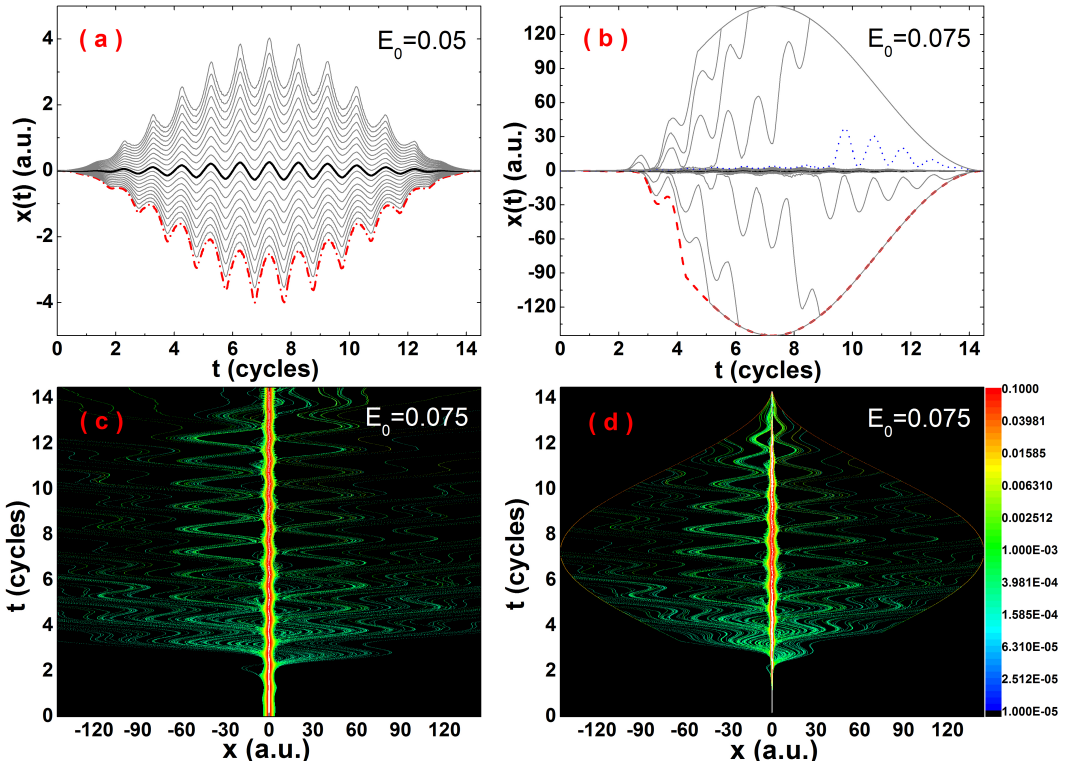

Figure 4.7: Upper panels: Flow of Bohmian trajectories obtained from the reconstruction procedure described in this section, for a soft-core potential $V_{sc}(x)$ in a flat-top trapezoidal field with frequency $\omega_0 = 0.057$ and amplitudes: (a) $E_0 = 0.05$ and (b) $E_0 = 0.075$. As a starting point we considered the Fourier transforms $x(\omega)$ of each trajectory convoluted with the Hanning filter (4.1). Lower panels: time-dependent probability density reconstructed from an ensemble of 5000 Bohmian trajectories. Panels (c) and (d) have been computed for $E_0 = 0.075$ without and with the Hanning filter, respectively. To facilitate a direct comparison, we have used the same axes scales and the same fonts to designate different types of trajectories as those in Figs. 3.2(a) and (b).

away [see Fig. 4.7(b)]. This has a major influence on the flow of the probability density, displayed in Figs. 4.7(c) and (d). If the filter is used, this probability density returns to the core at the end of the pulse, while in the absence of the filter there would be irreversible ionization.

4.5 Conclusions

In this chapter we have applied Bohmian mechanics to assess the influence of specific regions in configuration space on HHG. We have employed ensembles around the central Bohmian trajectory, starting at $x(0) = 0$, which has been found to yield HHG spectra with clear plateau and cutoff. If the ensemble average (2.25) is taken, these features are masked by the Bohmian trajectories associated with the probability-density flow far from the core. Furthermore, in the present framework, the TSM manifests itself in the phase of the wave function. This phase mimics the behavior of an ensemble of classical electron trajectories leaving and returning to its parent ion. Time-frequency analysis shows that this pattern is present in the probability flow that remains at the core.

Nevertheless, the probability flow leaving and returning to the core does influence how this phase builds up. In fact, by deliberately placing absorbing boundaries in the spatial regions within the ranges of excursion amplitudes of a classical electron, but outside the core region, we have degraded the phase of the whole wave function. This has influenced both the HHG spectrum and the time-frequency maps of the central Bohmian trajectory, and the degradation has occurred as expected from the TSM. In fact, the first sets of features to be eliminated from the time-frequency maps as the absorber increasingly approaches the core correspond to the trajectories with longer excursion times. These changes are transmitted nonlocally, as the probability density flow associated with the central Bohmian trajectory never leaves the core region. Since Bohmian trajectories are in fact slices of the wave function, they will always depend on the behavior associated with the whole wave function, regardless of the positions occupied by the probability density in configuration space. Hence, if the wave function is altered far from the core, all the slices will be different. One should note that the probability-density flow could have been altered in other ways such as by employing inhomogeneous media [129, 130]. However, moving boundaries allow the systematic deconstruction of the flow in the desired spatial range.

Our results also show that a spatially extended core is paramount for obtaining good agreement with the TDSE, even if this spatial extension is small. This

holds not only for the low plateau and below-threshold harmonics, but also for the cutoff energy region. This implies that an initial wave-packet spread in position space is necessary for an accurate description of the problem. From a Bohmian trajectory perspective, this spread manifests itself as an uncertainty in the initial conditions $x_i(0)$ [58]. This is consistent with recent studies in which the SFA has been improved to include this spread [134, 137]. Its fully quantum mechanical version, without resorting to the steepest-descent method, has shown very good agreement with the TDSE in the cutoff region. In the time-frequency maps, neglect of the initial position spread causes an over-enhancement in the signal related to the long SFA trajectory [135, 136]. We have identified a similar effect in our computations only the central Bohmian trajectory is considered. An important issue here is nonlocality. In the full quantum mechanical version of the SFA, the time-dependent wave function is described as a coherent superposition of the ground state and the continuum, which is approximated by field-dressed plane waves. In this case, the continuum is also nonlocal. Due to the approximations involved, however, the phase picked up by the time-dependent wave function is different from that of the full TDSE. Bohmian trajectories consider the full phase, but may restrict the initial spread in position space.

We also revisited the reasons for the acceleration form of the dipole operator being preferable when computing HHG spectra. We have found that the dipole acceleration effectively works as a filter that removes from the statistics Bohmian trajectories far away from the core. These trajectories are over-emphasized in the expectation value of the dipole length. The filter, such as a Hanning filter, is commonly used when computing HHG spectra from the dipole length. This has been demonstrated by back-transforming the spectra of individual Bohmian trajectories in which this filter has been employed.

Finally, we would like to elaborate on the advantages and disadvantages of Bohmian trajectories. On one hand, since Bohmian trajectories contain all phase information related to the full time-dependent Hamiltonian, both the driving field and the binding potential are accounted for. They may thus be used to probe the time-dependent wave function in specific regions in configuration space, and phenomena associated with this wave function, such as the example provided in this

thesis. They can also be employed for visualization purposes in order to access how the time-dependent probability density flow behaves in particular spatial regions, e.g., near the core or far from it. On other hand, these trajectories are highly nonlocal entities. Therefore, if one is interested in information related to the phase of the wave function, and not the probability-density flow, one needs to employ additional resources such as time-frequency maps or quasiprobabilities in phase space. Another advantage is that, in principle, Bohmian trajectories may be used for reconstructing the time-dependent probability flow or parts thereof. In practice, however, a huge obstacle to this reconstruction is that, according to the present scheme, it is first necessary to solve the full TDSE in order to obtain these trajectories. This is particularly problematic for systems with many degrees of freedom. However, a real effort to overcome this obstacle and construct Bohmian trajectories without the need for the TDSE solution has been reported in Ref. [138].

Part II

Initial value representations (IVRs)

Nowadays, the accurate description of dynamical processes in complex molecular systems has become a hot topic in modern physics and chemistry. The classical method refers to the numerical solution of the classical mechanical equations of an ensemble of interacting atoms and molecules, and is proven to be an useful tool to describe these processes in many systems, such as isolated molecules, biopolymers, liquids and surfaces [139–142]. However, atoms and molecules actually exhibit quantum behavior and cannot be explained by the classical equations of motion. For instance, the zero-point energy [143–145], bound state energies [146–148], scattering and photodissociation resonances [149–154], coherence phenomena [155–158] or tunneling [159] effects are absent in classical mechanics. A full quantum mechanical method can address all of the above issues. However, to obtain an explicit quantum solution of complex systems with many degrees of freedom is extremely computational intense and almost unfeasible [160–162].

To overcome the above problem, several supplementary theoretical methods have been developed to model the quantum effects. One of these methods is the mixed quantum-classical method, in which several important degrees of freedom are treated by quantum mechanics while the remaining are treated by classical mechanics. This method has been successfully applied to a variety of applications [163–167]. However, because it describes various degrees of freedom using a combination of quantum and classical mechanics, this intrinsic inconsistency limits its wide application [168].

Other approaches that have recently attracted much interest are semiclassical methods based on classical trajectories, which are semiclassical approximations of the Feynman propagator [169] and treat all of the degrees of freedom semiclassically. Compared to quantum mechanical calculations, semiclassical concepts can often provide a more qualitatively intuitive understanding of the dynamics. For example, it has been shown that many features in simple molecular absorption spectra can be explained by semiclassical dynamics [170–172]. Moreover, much work [77, 159, 173–180] in the early 1970s has shown that in contrast to classical approaches, semiclassical methods are, in principle, capable of describing essentially all quantum effects in molecular dynamics, such as interference (coherence), tunneling (Although, since 1990s, there has been some debate on whether

semiclassical method, based on classical trajectories, can be applied to the model of tunneling, and if so, to which extent. More discussions related to this can be found in the Refs. [181–184].) and selection rules due to identical particle symmetry, and quantization of bounded motions since they all ultimately arise from the superposition of probability amplitudes, which is contained in semiclassical description [168].

Those methods (semiclassical methods), based on classical trajectories, have been used successfully for many years to describe molecular dynamics, because they can overcome the exponential increase of the computational effort with the number of coupled degrees of freedom in quantum basis-set calculations. For instance, in suitable cases, they might be applied to treat the dynamics of large systems with dozens of degrees of freedom [185]. However, until recently, the practical applicability of rigorous semiclassical methods was limited to small molecules or systems in reduced dimensionality (typically with two to three degrees of freedom) [159, 160, 171, 172, 177]. There are various reasons for the limitation of their applications depending on the method applied. For instance, for the VVG propagator [79, 79, 81], which is the most straight forward semiclassical approximation to the Feynman path integral [169], the restriction to small systems is mainly due to the fact that this propagator is based on classical trajectories that are determined by both initial and final positions. The trajectories required for the computation are in terms of boundary conditions, they are nonunique and must be found by a numerical search. This would be a severe numerical challenge for multidimensional systems [185]. Another problem of this method is that it breaks down at the turning points of the classical trajectories (caustic condition [185]) where the VVG propagator diverges numerically, this property limits the accuracy of the results using the VVG propagator.

Fortunately, these kinds of problems can be overcome by the IVR method, which was firstly proposed by Miller [77] in the context of classical S-matrix theory. It converts the nonlinear boundary value or the "root search" problem into an integrand over the initial conditions and specifies the trajectories uniquely. The most successful IVR approach is the HK propagator formulation [82, 83], in which an additional prefactor depending on the elements of the monodromy ma-

trix of the trajectory is included for each member of the swarm and ensures the semiclassical nature of the approximation. Furthermore, the HK propagator does not require the trajectory searches and the integrations are easier to perform. Several trajectory-based methods motivated by the HK propagator have been developed in recent years, such as the ab initio multiple spawning method (AIMS) [186]; Gaussian-based methods inspired by the multiconfigurational time-dependent Hartree method (MCTDH) [187], including Gaussian multiconfigurational time-dependent Hartree method (G-MCTDH) [188] and variational multiconfigurational Gaussians method (vMCG)[189]; and the trajectory-based CCS method [85–97] developed by Shalashilin and Child. These methods have different main features: adaptive basis sets can be employed to the AIMS, and the Gaussians on two different potential energy surfaces become decoupled, therefore to keep the coupling the basis set must be increased and can become rather large in the time propagation; the G-MCTDH uses the MCTDH and regular basis for a few most important degrees of freedom and Gaussian CSs for the remaining; similar to the AIMS, the vMCG expresses the wave function as a superposition of frozen Gaussian CSs and the trajectories are determined through the variational principle on all the parameters of the wave function, such as the phase space positions and their amplitudes; the CCS method is a method lying between AIMS and vMCG, the trajectories used in the CCS method are independent from each other, just like the classical trajectories, hence, it is much cheaper than the AIMS and vMCG methods. More discussions about the relations and differences of these methods can be found in the Ref. [190].

Part II of this thesis mainly focuses on the IVR methods, namely, the HK propagator and the CCS method. The two methods are applied to study the phase space dynamics in Chapter 6. In Chapter 7, the CCS method is employed to study the HHG spectrum. One important aspect of the CCS method is that the CSs form a continuous basis, which casts the TDSE into an exact integro-differential form for the CS amplitudes, in which the Hamiltonian appears as a kernel rather than a matrix as used in other IVR methods. Furthermore, by working on a trajectory guided basis which moves not under the bare classical Hamiltonian, but under the CS average of the suitably ordered quantum operator $H_{ord}(z^*, z) = \langle z|H|z\rangle$, the kernel may be reduced to a small smooth function.

Quantum effects are accounted in the CCS method, though to a lesser extent than the fully variational trajectories [190]. Another attractive advantage of the CCS method is that the smoothness of the integro-differential kernel allows Monte Carlo sampling of the trajectory swarm, scales quadratically with the number of degrees of freedom M as $N \sim M^2$, and therefore significantly reduces the number of initial basis vectors. This is in sharp contrast to the exponential growth of the number of basis functions $N = l^M$, where, l is the number of grid points. Consequently, the CCS approach can be easily applied to high dimensional systems without marked increase in computational difficulty, for instance, to polyatomic molecules or small clusters [89, 91], which would not be possible with the TDSE.

Chapter 5

Basic theory of the coupled coherent states (CCS) method

In 1926, immediately after the birth of quantum mechanics, Schrödinger introduced the concept of what is now called "coherent states" in connection with the classical states of the quantum harmonic oscillator [191]. This concept was subsequently applied to the study of the quantum mechanical measurement process by Neumann [192]. The first modern and most important application of CSs were introduced by Glauber in the 1960s [193] to study the electromagnetic correlation functions in quantum optics by constructing the eigenstates of the annihilation operator of the harmonic oscillator, and a generalization of Glauber's CSs has been suggested by Sudarshan and Glauber [193–196]. Almost at the same time, Klauder constructed a set of continuous states which contained the basic ideas of CSs for arbitrary Lie groups [197]. Thereafter, many attempts to build different kinds of CSs have been made, various kinds of generalized CSs and their properties can be found in Ref. [198] and the references therein.

About two decades ago, Klauder [199] and Majumdar [200] made significant progresses in constructing generalized CSs. Based on the construction procedure proposed by Klauder, Fox established and studied the genuine Gaussian generalized CSs for the hydrogen atom [201]. This kind of CSs can provide a general means for the construction of the Husimi-Wigner distribution [202] and be employed to illustrate the quantum and classical correspondence. They have also been applied recently beyond the simple harmonic oscillator and standard

Coulomb potential systems, to diverse quantum systems [203, 204]. Undoubtedly, CSs have versatile potential applications and have obtained an important role in both quantum optics and quantum chemistry.

Based on Glauber's definition of CSs, this chapter describes the main theory behind the CCS method and is organised as follows. The definition of CSs is given in Section 5.1 and the corresponding properties of the CSs are shown in Section 5.2. Section 5.3 carries out the derivation of the CS wave function in the coordinate space. In section 5.4, an arbitrary wave function in the coherent states representation (CSR) is given, the relation between the CSR wave function and the coordinate representation (CR) wave function are also discussed. In Section 5.5, the basic equations of the CSR wave function are listed. Finally, discrete representations of the CCS equations, and the propagation of CSR wave function are displayed in Sections 5.6 and 5.7, respectively.

5.1 Definition of the coherent states (CSs)

Following Glauber's work, a CS of harmonic oscillator can be defined as eigenstate of the annihilation operator $\hat{z}$ with eigenvalue z, which is

$$\hat{z}|z\rangle = z|z\rangle, \tag{5.1}$$

Because $\hat{z}$ is an non-hermitian operator, the eigenvalue z is not necessary real, it can be any complex value.

Expressing this state in terms of the photon number state $|n\rangle$:

$$|z\rangle = \sum_{n=0}^{\infty} \alpha_n |n\rangle, \tag{5.2}$$

where α_n denotes the probability amplitude of finding n photons in the CS $|z\rangle$, which can be obtained through the following procedure.

By inserting this expression into Eq. (5.1) and applying

$$\hat{z}|n\rangle = \sqrt{n}|n-1\rangle, \tag{5.3}$$

one can obtain

$$\hat{z}|z\rangle = \sum_{n=0}^{\infty} \alpha_n \sqrt{n}|n-1\rangle = \sum_{n=0}^{\infty} z\alpha_n|n\rangle. \tag{5.4}$$

Multiply $\langle m|$ to the left of the above equation and with the help of the orthonormality property of the number states, one can obtain

$$\alpha_{m+1}\sqrt{m+1} = z\alpha_m, \tag{5.5}$$

which is equivalent to

$$\alpha_{m+1} = z\frac{\alpha_m}{\sqrt{m+1}}. \tag{5.6}$$

Therefore,

$$\alpha_n = \frac{z^n}{\sqrt{n!}}\alpha_0. \tag{5.7}$$

Combining Eq. (5.7) with the normalisation condition of the CS

$$\langle z|z\rangle = \sum_{n,m=0}^{\infty} \langle m|n\rangle = \sum_{n=0}^{\infty} |\alpha_n|^2 = 1, \tag{5.8}$$

one can obtain

$$\sum_{n=0}^{\infty} \frac{|z|^{2n}}{n!}|\alpha_0|^2 = 1. \tag{5.9}$$

Hence,

$$\alpha_0 = \exp\left[-|z|^2/2 + i\theta\right], \tag{5.10}$$

where θ is the phase of α_0, which depends on z and in the standard definition of CS is selected as zero [205]. The corresponding CS of Eq. (5.2) reads as

$$|z\rangle = \exp\left(-\frac{|z|^2}{2}\right)\sum_{n=0}^{\infty}\frac{z^n}{\sqrt{n!}}|n\rangle. \tag{5.11}$$

5.2 The properties of CSs

5.2.1 Non-orthogonality

One property of the CS defined above is that, in general, two CSs are not orthogonal. From the definition of the CS (5.11), we can see that, for two arbitrary CSs

$|z_i\rangle$ and $|z_j\rangle$, the overlap between them is

$$\begin{aligned}\langle z_i|z_j\rangle &= \exp\left(-\frac{1}{2}|z_i|^2-\frac{1}{2}|z_j|^2\right)\sum_{n,m=0}^{\infty}\frac{\left(z_i^*\right)^m z_j^n}{\sqrt{m!n!}}\langle m|n\rangle \\ &= \exp\left(-\frac{1}{2}|z_i|^2-\frac{1}{2}|z_j|^2\right)\sum_{n=0}^{\infty}\frac{\left(z_i^* z_j\right)^n}{n!} \\ &= \exp\left(-\frac{1}{2}|z_i|^2-\frac{1}{2}|z_j|^2+z_i^* z_j\right).\end{aligned} \tag{5.12}$$

Note that, in the above derivation the orthogonality of the number states is employed. The absolute value square of the overlap is given by

$$\begin{aligned}|\langle z_i|z_j\rangle|^2 &= \exp\left(-\frac{1}{2}|z_i|^2-\frac{1}{2}|z_j|^2+z_i^* z_j\right)\exp\left(-\frac{1}{2}|z_i|^2-\frac{1}{2}|z_j|^2+z_i z_j^*\right) \\ &= \exp\left(-|z_i-z_j|^2\right).\end{aligned} \tag{5.13}$$

From this we can see that the CSs do not form an orthogonal set, the overlap between any two CSs is given by a Gaussian, the larger the separation the smaller the overlap.

5.2.2 Completeness

Another property of the CS is the completeness, this can be demonstrated by studying the operator

$$\hat{I}=\frac{1}{\pi}\int|z\rangle\langle z|\mathrm{d}^2 z. \tag{5.14}$$

In order to describe the above integral we introduce the differential element of area in the z plane

$$\mathrm{d}^2 z=\mathrm{dRe}(z)\mathrm{dIm}(z)=|z|\mathrm{d}|z|\mathrm{d}\theta. \tag{5.15}$$

Note that, in the above equation, $\mathrm{Re}(z)$ and $\mathrm{Im}(z)$ denote the real and imaginary part of z, respectively, and the complex parameter $z=|z|\exp(i\theta)$ describes the eigenvalue of a CS.

Inserting Eq. (5.11) into (5.14) we obtain

$$\hat{I}=\frac{1}{\pi}\sum_{n,m=0}^{\infty}\frac{1}{\sqrt{m!n!}}\int_0^{\infty}|z|^{m+n+1}\exp\left(-|z|^2\right)\mathrm{d}|z|\int_{-\pi}^{\pi}\exp\left[-i(m-n)\theta\right]|n\rangle\langle m|\mathrm{d}\theta. \tag{5.16}$$

With the help of

$$\int_{-\pi}^{\pi} \exp\left(im\theta\right) \mathrm{d}\theta = \delta_{m,0}, \tag{5.17}$$

the double integral above can be reduced to

$$\hat{I} = \sum_{n=0}^{\infty} \frac{1}{n!} \int_{0}^{\infty} |z|^{2n} \exp\left(-|z|^2\right) \mathrm{d}|z|^2 |n\rangle\langle n|. \tag{5.18}$$

Since

$$\int_{0}^{\infty} x^n \exp(-x) \mathrm{d}x = \Gamma(n+1) = n! \tag{5.19}$$

and the completeness relation of the number states

$$\sum_{n=0}^{\infty} |n\rangle\langle n| = 1, \tag{5.20}$$

Eq. (5.18) can be reduced to 1. The operator (5.14)

$$\hat{I} = \frac{1}{\pi} \int |z\rangle\langle z| \mathrm{d}^2 z = 1 \tag{5.21}$$

is a completeness relation of the CSs, and is also known as the identity operator.

5.2.3 Minimum uncertainty

If we introduce a pair of Hermitian operators $\hat{q}$ and $\hat{p}$ to represent the coordinate and momentum of the harmonic oscillator, which are written as

$$\hat{q} = \sqrt{\frac{1}{2\gamma}} \left(\hat{z}^\dagger + \hat{z}\right), \tag{5.22}$$

$$\hat{p} = -i\hbar\sqrt{\frac{\gamma}{2}} \left(\hat{z}^\dagger - \hat{z}\right), \tag{5.23}$$

where $\gamma = m\omega/\hbar$; correspondingly, we can get

$$\hat{q}^2 = \frac{1}{2\gamma} \left(\hat{z}^\dagger + \hat{z}\right)^2 = \frac{1}{2\gamma} \left(\hat{z}^{\dagger 2} + \hat{z}^2 + 2\hat{z}^\dagger \hat{z} + 1\right), \tag{5.24}$$

$$\hat{p}^2 = -\frac{\gamma\hbar^2}{2} \left(\hat{z}^\dagger - \hat{z}\right)^2 = -\frac{\gamma\hbar^2}{2} \left(\hat{z}^{\dagger 2} + \hat{z}^2 - 2\hat{z}^\dagger \hat{z} - 1\right). \tag{5.25}$$

Note that, the commutation relation $\left[\hat{z}, \hat{z}^{\dagger}\right] = 1$ is applied in the above equations.

One can easily get the expectation value of these operators (5.22-5.25):

$$\langle z|\hat{q}|z\rangle = \sqrt{\frac{2}{\gamma}}\mathrm{Re}(z), \tag{5.26}$$

$$\langle z|\hat{p}|z\rangle = \hbar\sqrt{2\gamma}\mathrm{Im}(z), \tag{5.27}$$

$$\langle z|\hat{q}^2|z\rangle = \frac{1}{2\gamma}\left(z^{*2} + z^2 + 2z^*z + 1\right) = \frac{1}{2\gamma}\left[4\mathrm{Re}^2(z) + 1\right], \tag{5.28}$$

$$\langle z|\hat{p}^2|z\rangle = -\frac{\gamma\hbar^2}{2}\left(z^{*2} + z^2 - 2z^*z - 1\right) = \frac{\gamma\hbar^2}{2}\left[4\mathrm{Im}^2(z) + 1\right]. \tag{5.29}$$

Therefore,

$$\left(\triangle q\right)^2 = \langle\hat{q}^2\rangle - \langle\hat{q}\rangle^2 = \frac{1}{2\gamma}, \tag{5.30}$$

$$\left(\triangle p\right)^2 = \langle\hat{p}^2\rangle - \langle\hat{p}\rangle^2 = \frac{\gamma\hbar^2}{2}, \tag{5.31}$$

and CSs are states with a minimum uncertainty relationship

$$\left(\triangle q\right)^2\left(\triangle p\right)^2 = \frac{\hbar^2}{4}. \tag{5.32}$$

5.3 CSs in the coordinate representation (CR)

Make a simple ansatz, Eqs. (5.22) and (5.23) can be written as

$$\hat{z} = \sqrt{\frac{\gamma}{2}}\hat{q} + \frac{i}{\hbar}\sqrt{\frac{1}{2\gamma}}\hat{p}, \tag{5.33}$$

$$\hat{z}^{\dagger} = \sqrt{\frac{\gamma}{2}}\hat{q} - \frac{i}{\hbar}\sqrt{\frac{1}{2\gamma}}\hat{p}. \tag{5.34}$$

In order to find the wave function for the CSs, we rewrite the definition of Eq. (5.1) as

$$\left(\sqrt{\frac{\gamma}{2}}\hat{q} + \frac{i}{\hbar}\sqrt{\frac{1}{2\gamma}}\hat{p}\right)|z\rangle = z|z\rangle. \tag{5.35}$$

If we multiply both sides from the left by $\langle q'|$, an eigenbra of $\hat{q}$, we obtain

$$\langle q'|\sqrt{\frac{\gamma}{2}}\hat{q} + \frac{i}{\hbar}\sqrt{\frac{1}{2\gamma}}\hat{p}|z\rangle = z\langle q'|z\rangle. \tag{5.36}$$

Because the momentum can be presented by a derivative operator, i.e., $\langle q'|p = -i\hbar(\mathrm{d}/\mathrm{d}q')\langle q'|$, we can find the coordinate wave function $\langle q'|z\rangle$ that obeys the following differential equation

$$\frac{\mathrm{d}}{\mathrm{d}q'}\langle q'|z\rangle = \left(-\gamma q' + \sqrt{2\gamma}z\right)\langle q'|z\rangle. \tag{5.37}$$

The solution of the above equation is

$$\langle q'|z\rangle = N\exp\left(-\frac{\gamma}{2}q'^2 + \sqrt{2\gamma}zq'\right), \tag{5.38}$$

where N is the normalisation factor of the wave function, which can be obtained through

$$\int |\langle q'|z\rangle|^2 \mathrm{d}q' = 1. \tag{5.39}$$

From (5.38) we can see

$$\begin{aligned} |\langle q'|z\rangle|^2 &= |N|^2\exp\left[-\gamma q'^2 + \sqrt{2\gamma}(z+z^*)q'\right] \\ &= |N|^2\exp\left\{-\left[\sqrt{\gamma}q' - \frac{(z+z^*)}{\sqrt{2}}\right]^2 + \frac{(z+z^*)^2}{2}\right\}, \end{aligned} \tag{5.40}$$

with the help of

$$\int_{-\infty}^{\infty}\exp(x-\alpha)^2\mathrm{d}x = \sqrt{\pi}, \tag{5.41}$$

and integration of Eq. (5.40) one obtains

$$\int |\langle q'|z\rangle|^2\mathrm{d}q' = |N|^2\sqrt{\frac{\pi}{\gamma}}\exp\left[\frac{(z+z^*)^2}{2}\right]. \tag{5.42}$$

Hence,

$$N = \left(\frac{\gamma}{\pi}\right)^{1/4}\exp\left[-\frac{(z+z^*)^2}{4} + i\phi\right], \tag{5.43}$$

where ϕ is an arbitrary real phase. With no loss of generality, we can choose $i\phi = -1/4\,(z^2 - z^{*2})$ [206], so that

$$N = \left(\frac{\gamma}{\pi}\right)^{1/4}\exp\left(-\frac{|z|^2 + z^{*2}}{2}\right). \tag{5.44}$$

This is because

$$|N|^2 = \sqrt{\frac{\gamma}{\pi}}\exp\left(-\frac{|z|^2 + z^{*2} + |z|^2 + z^2}{2}\right) = \sqrt{\frac{\gamma}{\pi}}\exp\left[-\frac{(z+z^*)^2}{2}\right], \tag{5.45}$$

which satisfies Eq. (5.43). Hence,

$$\langle q'|z\rangle = \left(\frac{\gamma}{\pi}\right)^{1/4} \exp\left(-\frac{\gamma}{2}q'^2 + \sqrt{2\gamma}q'z - \frac{1}{2}|z|^2 - \frac{1}{2}z^2\right), \tag{5.46}$$

considering Eqs. (5.26) and (5.27), the above wave function can be written as

$$\langle q'|z\rangle = \left(\frac{\gamma}{\pi}\right)^{1/4} \exp\left[-\frac{\gamma}{2}(q'-q)^2 + \frac{i}{\hbar}p\,(q'-q) + \frac{i}{2\hbar}pq\right]. \tag{5.47}$$

One should bear in mind that in the above equation the eigenvalue of the operator $\hat{z}$, denoted as

$$z = \sqrt{\frac{\gamma}{2}}q + \frac{i}{\hbar}\sqrt{\frac{1}{2\gamma}}p \tag{5.48}$$

is applied. In order to avoid confusion, we replace q' by an normal coordinate notation x in our later work, hence, the wave function of CSs in the CR is written as

$$\langle x|z\rangle = \left(\frac{\gamma}{\pi}\right)^{1/4} \exp\left[-\frac{\gamma}{2}(x-q)^2 + \frac{i}{\hbar}p\,(x-q) + \frac{i}{2\hbar}pq\right]. \tag{5.49}$$

5.4 Wave function in the coherent state representation (CSR)

In the CSR, the wave function $\Phi(z,t)$ for an arbitrary wave function $|\Psi(t)\rangle$ can be calculated by projecting the wave function onto the CS, i.e.

$$\Phi(z,t) = \langle z|\Psi(t)\rangle. \tag{5.50}$$

Using the identity operator Eq. (5.21), an arbitrary wave function $|\Psi(t)\rangle$ can be calculated by using the wave function $\Phi(z,t)$ through

$$|\Psi(t)\rangle = \frac{1}{\pi}\int |z\rangle\langle z|\Psi(t)\rangle \mathrm{d}^2z = \frac{1}{\pi}\int |z\rangle\Phi(z,t)\mathrm{d}^2z, \tag{5.51}$$

with the phase space element $\mathrm{d}^2z = \mathrm{d}q\mathrm{d}p/2\hbar$, which can be obtained through Eqs. (5.26) and (5.27). For instance, in the coordinate space, the wave function $\Psi(x,t)$ can be calculated through

$$\Psi(x,t) = \langle x|\Psi(t)\rangle = \frac{1}{\pi}\int \langle x|z\rangle\langle z|\Psi(t)\rangle \mathrm{d}^2z = \frac{1}{\pi}\int \langle x|z\rangle\Phi(z,t)\mathrm{d}^2z. \tag{5.52}$$

Vice versa, the CSR wave function $\Phi(z,t)$ can be obtained from the CR wave function $\Psi(x,t)$ through

$$\Phi(z,t) = \int \langle z|x\rangle\langle x|\Psi(t)\rangle \mathrm{d}x = \int \langle z|x\rangle \Psi(x,t)\mathrm{d}x. \tag{5.53}$$

where $\langle z|x\rangle$ is the conjugate of Eq. (5.49).

5.5 Basic equations for the CSR wave function

Starting from the TDSE

$$\frac{\mathrm{d}|\Psi(t)\rangle}{\mathrm{d}t} = -\frac{i}{\hbar}\hat{H}|\Psi(t)\rangle, \tag{5.54}$$

the basic equation that a CSR wave function satisfies is as follows

$$\frac{\mathrm{d}\langle z|\Psi(t)\rangle}{\mathrm{d}t} = \langle \dot{z}|\Psi(t)\rangle + \langle z|\dot{\Psi}(t)\rangle = \frac{1}{\pi}\int \left[\langle \dot{z}|z'\rangle - \frac{i}{\hbar}\langle z|\hat{H}|z'\rangle\right]\langle z'|\Psi\rangle \mathrm{d}^2 z', \tag{5.55}$$

where we use the identity operator (5.21) to obtain the second equality. If the CSs are time-independent, the first term on the right side of Eq. (5.55) is zero, and this equation can be reduced to

$$\frac{\mathrm{d}\langle z|\Psi(t)\rangle}{\mathrm{d}t} = \frac{1}{\pi}\int -\frac{i}{\hbar}\langle z|\hat{H}|z'\rangle\langle z'|\Psi\rangle \mathrm{d}^2 z'. \tag{5.56}$$

If the CSs are time-dependent,

$$\begin{aligned}\frac{\mathrm{d}|z\rangle}{\mathrm{d}t} &= \frac{\mathrm{d}}{\mathrm{d}t}\left[\exp\left(-\frac{|z|^2}{2}\right)\sum_{n=0}^{\infty}\frac{z^n}{\sqrt{n!}}|n\rangle\right] \\ &= -\frac{1}{2}\frac{\mathrm{d}(z^*z)}{\mathrm{d}t}|z\rangle + \frac{\mathrm{d}z}{\mathrm{d}t}\exp\left(-\frac{|z|^2}{2}\right)\sum_{n=0}^{\infty}\frac{nz^{n-1}}{\sqrt{n!}}|n\rangle,\end{aligned} \tag{5.57}$$

and

$$\frac{\mathrm{d}\langle z|}{\mathrm{d}t} = -\frac{1}{2}\frac{\mathrm{d}(z^*z)}{\mathrm{d}t}\langle z| + \frac{\mathrm{d}z^*}{\mathrm{d}t}\exp\left(-\frac{|z|^2}{2}\right)\sum_{n=0}^{\infty}\frac{n(z^*)^{n-1}}{\sqrt{n!}}\langle n|, \tag{5.58}$$

so that

$$\begin{aligned}\langle \dot{z}|z'\rangle &= -\frac{1}{2}\frac{\mathrm{d}(z^*z)}{\mathrm{d}t}\langle z|z'\rangle + \frac{\mathrm{d}z^*}{\mathrm{d}t}\exp\left(-\frac{|z|^2}{2}\right)\sum_{n=0}^{\infty}\frac{n(z^*)^{n-1}}{\sqrt{n!}}\langle n|\exp\left(-\frac{|z'|^2}{2}\right)\sum_{n'=0}^{\infty}\frac{z^{n'}}{\sqrt{n'!}}|n'\rangle \\ &= -\frac{1}{2}\frac{\mathrm{d}(z^*z)}{\mathrm{d}t}\langle z|z'\rangle + \frac{\mathrm{d}z^*}{\mathrm{d}t}z'\exp\left(z^*z' - \frac{|z|^2}{2} - \frac{|z'|^2}{2}\right) \\ &= -\frac{1}{2}\frac{\mathrm{d}(z^*z)}{\mathrm{d}t}\langle z|z'\rangle + \frac{\mathrm{d}z^*}{\mathrm{d}t}z'\langle z|z'\rangle \\ &= \langle z|z'\rangle\left[\frac{\mathrm{d}z^*}{\mathrm{d}t}z' - \frac{1}{2}\left(z\frac{\mathrm{d}z^*}{\mathrm{d}t} + \frac{\mathrm{d}z}{\mathrm{d}t}z^*\right)\right].\end{aligned} \tag{5.59}$$

Then the Schrödinger equation in the CSR can be reduced to

$$\frac{\mathrm{d}\langle z|\Psi(t)\rangle}{\mathrm{d}t} = \frac{1}{\pi}\int\langle z|z'\rangle\left[\frac{i}{\hbar}\frac{\mathrm{d}S_z}{\mathrm{d}t} - \frac{i}{\hbar}\delta^2 H_{ord}(z^*,z')\right]\langle z'|\Psi(t)\rangle\mathrm{d}^2z', \tag{5.60}$$

where

$$S_z = \int\left[\frac{i\hbar}{2}\left(z^*\frac{\mathrm{d}z}{\mathrm{d}t} - \frac{\mathrm{d}z^*}{\mathrm{d}t}z\right) - H_{ord}(z^*,z)\right]\mathrm{d}t \tag{5.61}$$

is the classical action along the trajectory, and

$$\delta^2 H_{ord}(z^*,z') = H_{ord}(z^*,z') - H_{ord}(z^*,z) - \frac{\partial H_{ord}(z^*,z)}{\partial z}(z'-z) \tag{5.62}$$

couples different CSs $|z\rangle$ and $|z'\rangle$, with $\frac{H_{ord}(z^*,z)}{\partial z} = -\frac{i}{\hbar}\frac{\mathrm{d}z^*}{\mathrm{d}t}$. $H_{ord}(z^*,z)$ is the ordered Hamiltonian which in general, for two different CSs $|z\rangle$ and $|z'\rangle$, is defined as

$$\langle z|\hat{H}|z'\rangle = \langle z|\hat{H}_{ord}\left(\hat{z}^\dagger,\hat{z}\right)|z'\rangle = \langle z|z'\rangle H_{ord}\left(z^*,z'\right), \tag{5.63}$$

with

$$\begin{aligned}\hat{H}_{ord}\left(\hat{z}^\dagger,\hat{z}\right) &= \frac{\hat{P}_x^2}{2m} + V(\hat{x}) \\ &= \frac{1}{2m}\left[\frac{i}{\hbar}\sqrt{\frac{\gamma}{2}}\left(\hat{z}^\dagger - \hat{z}\right)\right]^2 + V\left[\sqrt{\frac{1}{2\gamma}}\left(\hat{z}^\dagger + \hat{z}\right)\right].\end{aligned} \tag{5.64}$$

Physically, Eq. (5.62) allows for quantum interference to occur. Because of the CSs form a non-orthogonal basis, these off-diagonal terms are non-vanishing.

In fact,

$$\begin{aligned}\frac{\mathrm{d}z}{\mathrm{d}t} &= \sqrt{\frac{\gamma}{2}}\dot{q} + \frac{i}{\hbar}\frac{1}{\sqrt{2\gamma}}\dot{p} \\ &= \sqrt{\frac{\gamma}{2}}\frac{\partial H_{ord}(p,q)}{\partial p} - \frac{i}{\hbar}\frac{1}{\sqrt{2\gamma}}\frac{\partial H_{ord}(p,q)}{\partial q} \\ &= -\frac{i}{\hbar}\left[\frac{\partial H_{ord}(z^*,z)}{\partial p}\frac{\partial p}{\partial z^*} + \frac{\partial H_{ord}(z^*,z)}{\partial q}\frac{\partial q}{\partial z^*}\right].\end{aligned} \tag{5.65}$$

Note that, in Eq. (5.65), the following Hamiltonian equations

$$\begin{aligned}\dot{q} &= \frac{\partial H(p,q)}{\partial p}, \\ \dot{p} &= -\frac{\partial H(p,q)}{\partial q}\end{aligned} \tag{5.66}$$

and

$$\begin{aligned}\frac{\partial q}{\partial z^*} &= \sqrt{\frac{1}{2\gamma}}, \\ \frac{\partial p}{\partial z^*} &= i\hbar\sqrt{\frac{\gamma}{2}}\end{aligned} \tag{5.67}$$

are applied.

Because of

$$\frac{\partial H_{ord}(z^*,z)}{\partial z^*} = \frac{\partial H_{ord}(z^*,z)}{\partial p}\frac{\partial p}{\partial z^*} + \frac{\partial H_{ord}(z^*,z)}{\partial q}\frac{\partial q}{\partial z^*}, \tag{5.68}$$

Eq. (5.65) can be simplified as

$$\frac{\mathrm{d}z}{\mathrm{d}t} = -\frac{i}{\hbar}\frac{\partial H_{ord}(z^*,z)}{\partial z^*}. \tag{5.69}$$

Similarly, one can get

$$\frac{\mathrm{d}z^*}{\mathrm{d}t} = \frac{i}{\hbar}\frac{\partial H_{ord}(z^*,z)}{\partial z}. \tag{5.70}$$

From Eq. (5.60) one can rewrite the general solution of the CSR wave function in the form of

$$\Phi(z,t) = C(z,t)\exp\left(\frac{i}{\hbar}S_z\right). \tag{5.71}$$

Inserting Eq. (5.71) into Eq. (5.60), the equation for $C(z,t)$ can be written as

$$\frac{\mathrm{d}C(z,t)}{\mathrm{d}t} = -\frac{i}{\pi\hbar}\int\langle z|z'\rangle\delta^2 H_{ord}(z^*,z')C(z',t)\exp\left[\frac{i}{\hbar}\left(S_{z'} - S_z\right)\right]\mathrm{d}^2 z'. \tag{5.72}$$

Eqs. (5.55), (5.56), (5.60) and (5.72) are the basic equations in the CSR, which are all integro-differential equations.

5.6 Discrete representations of the CCS equations

5.6.1 C expression of the wave function in the CSR

In the numerical calculation the integral in the basic equations above is replaced by a sum. For instance, Eq. (5.56) is written as

$$\frac{\mathrm{d}\Phi_i}{\mathrm{d}t} = -\frac{i}{\hbar}\sum_{i=1}^{n} H_{ij}\Phi_j \frac{\Delta^2 z_j}{\pi} \tag{5.73}$$

where $\Phi_i = \Phi(z_i, t)$, $H_{ij} = \langle z_i|\hat{H}|z_j\rangle$, and $\Delta^2 z_j$ is the weight which depends on the quadrature used. The simplest form of the weight is given by

$$\Delta^2 z_j = \frac{\Delta q_j \Delta p_j}{2\hbar} = \frac{\Delta q \Delta p}{2\hbar}, \tag{5.74}$$

where Δq_j and Δp_j are the step sizes on the q and p axes, respectively. The last equality in Eq. (5.74) is only valid for equal spacing grids on both q and p axes (In this case, Δq and Δp are two different constants.).

In the above discrete form, the following non-unitary discrete identity operator is applied

$$\hat{I} = \frac{1}{\pi}\int |z\rangle\langle z|\mathrm{d}^2 z \simeq \sum_{j=1}^{n} |z_j\rangle\langle z_j| \frac{\Delta^2 z_j}{\pi}, \tag{5.75}$$

the same discretisation of (5.75) has been used in the short time semiclassical HK propagator on regular static phase space grids [207, 208]. In fact, on regular grids, the accuracy of the trapezoidal quadrature for Gaussian integrals or the sensitivity to the values of the sum strongly influences the validity of Eq. (5.75). Some of the criteria about how to choose the spacing Δq and Δp have been studied by Burant and von Neumann [192, 208]. Specific discussions on how to choose these parameters have been studied by Shalashilin on the test of hybrid mechanics [209–211] and short time CS propagation [207]. Therein, the Morse oscillator dynamics is propagated through Eq. (5.56) on a finite static grid.

By using the non-unitary identity operator in Eq. (5.75), the wave function

Eq. (5.51) is written as

$$|\Psi(t)\rangle = \sum_{i=1}^{n} |z_i\rangle\langle z_i|\Psi(t)\rangle \frac{\Delta^2 z_i}{\pi}. \tag{5.76}$$

The basic CCS equations (5.60) and (5.72) will be written as

$$\frac{\mathrm{d}\Phi_i}{\mathrm{d}t} = \sum_{j=1}^{n} \langle z_i|z_j\rangle \left[\frac{i}{\hbar}\frac{\mathrm{d}S_i}{\mathrm{d}t} - \frac{i}{\hbar}\delta^2 H_{ord}\left(z_i^*, z_j\right)\right] \Phi_j \frac{\Delta^2 z_j}{\pi} \tag{5.77}$$

and

$$\frac{\mathrm{d}C_i}{\mathrm{d}t} = -\frac{i}{\hbar}\sum_{j=1}^{n} \langle z_i|z_j\rangle \delta^2 H_{ord}\left(z_i^*, z_j\right) C_j \exp\left[\frac{i}{\hbar}\left(S_j - S_i\right)\right] \frac{\Delta^2 z_j}{\pi}, \tag{5.78}$$

where $S_i = S(z_i, t)$, and $C_i = C(z_i, t)$.

In the matrix form, Eq. (5.78) reads

$$\dot{\mathbf{C}} = -\frac{i}{\hbar}\mathbf{E}^*\left(\Omega \cdot \delta^2 H\right)\Delta^2\mathbf{Z}\mathbf{E}\mathbf{C} = -\frac{i}{\hbar}\mathbf{E}^*\delta^2\mathbf{H}\Delta^2\mathbf{Z}\mathbf{E}\mathbf{C} \tag{5.79}$$

where $\mathbf{C}$ is a $1 \times n$ column matrix, the others are $n \times n$ matrices. $\mathbf{E}$ and $\Delta^2\mathbf{Z}$ are diagonal matrices with elements

$$\mathbf{E}_{ij} = \delta_{ij} \exp\left(\frac{i}{\hbar} S_i\right) \tag{5.80}$$

and

$$\Delta^2\mathbf{Z}_{ij} = \delta_{ij}\frac{\Delta^2 z_i}{\pi}, \tag{5.81}$$

$\delta^2\mathbf{H}$ is given by

$$\delta^2\mathbf{H}_{ij} = \Omega_{ij}\delta^2 H_{ord}(z_i^*, z_j). \tag{5.82}$$

Although the norm conservation is used as one of the important criteria to describe the accuracy of the propagation, the norm $\langle\Psi(t)|\Psi(t)\rangle$ obtained from the discretisation of Eq. (5.75) is not automatically conserved and this weakens its wide application in the CCS approach. Fortunately, the norm can be preserved by choosing the following discrete representation of the identity in a finite non-orthogonal basis [92]:

$$\hat{I} = \sum_{ij} |z_i\rangle \left(\Omega^{-1}\right)_{ij} \langle z_j|. \tag{5.83}$$

Here, Ω^{-1} is the inverse of the overlap Ω with elements $\Omega_{ij} = \langle z_i | z_j \rangle$, and $\left(\Omega^{-1}\right)_{ij}$ are the corresponding matrix elements.

Replacing the identity operator Eqs. (5.75) by (5.83), Eq. (5.76)-(5.78) can be rewritten as:

$$|\Psi(t)\rangle = \sum_{i=1,j=1}^{n} |z_i\rangle \left(\Omega^{-1}\right)_{ij} \langle z_j|\Psi(t)\rangle = \sum_{i=1,j=1}^{n} |z_i\rangle \left(\Omega^{-1}\right)_{ij} \Phi_j, \tag{5.84}$$

$$\frac{\mathrm{d}\Phi_i}{\mathrm{d}t} = \sum_{i=1,j=1}^{n} \Omega_{ij} \left[\frac{i}{\hbar}\frac{\mathrm{d}S_i}{\mathrm{d}t} - \frac{i}{\hbar}\delta^2 H_{ord}(z_i^*, z_j)\right] \left(\Omega^{-1}\right)_{jk} \Phi_k, \tag{5.85}$$

and

$$\frac{\mathrm{d}C_i}{\mathrm{d}t} = -\frac{i}{\hbar} \sum_{i=1,j=1}^{n} \Omega_{ij} \delta^2 H_{ord}\left(z_i^*, z_j\right) \left(\Omega^{-1}\right)_{jk} C_j \exp\left[\frac{i}{\hbar}\left(S_k - S_i\right)\right]. \tag{5.86}$$

Very similar to Eq. (5.79), one can write Eq. (5.86) in the following matrix form:

$$\dot{\mathbf{C}} = -\frac{i}{\hbar}\mathbf{E}^* \left(\Omega \cdot \delta^2 \mathbf{H}\right) \Omega^{-1}\mathbf{E}\mathbf{C} = -\frac{i}{\hbar}\mathbf{E}^* \delta^2 \mathbf{H} \Omega^{-1}\mathbf{E}\mathbf{C}. \tag{5.87}$$

5.6.2 D expression of the wave function in the CSR

In fact, the coefficients C_i can be obtained through a different integral representation. We show proofs of this in the following.

Using Eqs. (5.51) and (5.71), one can write the wave function as

$$|\Psi(t)\rangle = \int |z'\rangle C(z', t) \exp\left(\frac{i}{\hbar} S_{z'}\right) \frac{\mathrm{d}^2 z'}{\pi}. \tag{5.88}$$

Starting from the TDSE (5.54) and closing it with $\langle z|$, instead of Eq. (5.55), one obtains

$$\begin{aligned}
&\int \left[\langle z|\dot{z}'\rangle C(z', t) + \langle z|z'\rangle \left(\frac{\mathrm{d}C(z', t)}{\mathrm{d}t} + \frac{i}{\hbar}\frac{\mathrm{d}S_{z'}}{\mathrm{d}t} C(z', t)\right)\right] \exp\left(\frac{i}{\hbar} S_{z'}\right) \frac{\mathrm{d}^2 z'}{\pi} \\
&= -\frac{i}{\hbar} \int \langle z|\hat{H}|z'\rangle C(z', t) \exp\left(\frac{i}{\hbar} S_{z'}\right) \frac{\mathrm{d}^2 z'}{\pi} \\
&= -\frac{i}{\hbar} \int \langle z|z'\rangle H_{ord}(z^*, z') C(z', t) \exp\left(\frac{i}{\hbar} S_{z'}\right) \frac{\mathrm{d}^2 z'}{\pi}.
\end{aligned} \tag{5.89}$$

Similar to Eq. (5.59), one can get

$$\langle z|\dot{z}'\rangle = \langle z|z'\rangle \left[z^* \frac{\mathrm{d}z'}{\mathrm{d}t} - \frac{1}{2}\left(z' \frac{\mathrm{d}z'^*}{\mathrm{d}t} + \frac{\mathrm{d}z'}{\mathrm{d}t} z'^* \right) \right]. \tag{5.90}$$

Inserting this equation into Eq. (5.89) and rearranging it, the following formula can be obtained

$$\begin{aligned} &\int \langle z|z'\rangle \frac{\mathrm{d}C(z',t)}{\mathrm{d}t} \exp\left(\frac{i}{\hbar} S_{z'}\right) \frac{\mathrm{d}^2 z'}{\pi} \\ &= -\frac{i}{\hbar} \int \langle z|z'\rangle \delta^2 H'^*_{ord}(z^*, z') C(z',t) \exp\left(\frac{i}{\hbar} S_{z'}\right) \frac{\mathrm{d}^2 z'}{\pi}, \end{aligned} \tag{5.91}$$

where

$$\delta^2 H'^*_{ord}(z^*, z') = H_{ord}(z^*, z') - H_{ord}(z'^*, z') - \frac{\partial H_{ord}(z'^*, z')}{\partial z'^*}(z^*, z'^*) \tag{5.92}$$

is different from $\delta^2 H_{ord}(z^*, z')$ in Eq. (5.62).

In order to obtain the discrete form of Eq. (5.91), it is necessary to make a simple ansatz and replace $C(z',t)$ by a new notation $D(z',t)$. Thus the corresponding discrete form of the wave function Eq. (5.88) can be written as

$$|\Psi(t)\rangle = \sum_{i=1}^{n} |z_i\rangle D_i \exp\left(\frac{i}{\hbar} S_i\right). \tag{5.93}$$

By comparing (5.93) to Eq. (5.84), one can obtain the relation between coefficients D_i and C_j in the form of

$$D_i \exp\left(\frac{i}{\hbar} S_i\right) = \sum_{j=1}^{n} \left(\Omega^{-1}\right)_{ij} C_j \exp\left(\frac{i}{\hbar} S_j\right). \tag{5.94}$$

The discrete representation of Eq. (5.91) is written as (details are given in the appendix)

$$\sum_{j}^{n} \langle z_i|z_j\rangle \dot{D}_j e^{\frac{i}{\hbar} S_j} = -\frac{i}{\hbar} \sum_{j}^{n} \langle z_i|z_j\rangle \delta^2 H'^*_{ord}(z_i^*, z_j) D_j e^{\frac{i}{\hbar} S_j} \tag{5.95}$$

or

$$\frac{\mathrm{d}D_k}{\mathrm{d}t} = -\frac{i}{\hbar} \sum_{ij}^{n} \left(\Omega^{-1}\right)_{ki} \left(\Omega_{ij} \cdot \delta^2 H'^*_{ord}(z_i^*, z_j)\right) D_j \exp\left[\frac{i}{\hbar}(S_j - S_k)\right], \tag{5.96}$$

with the discrete form of Eq. (5.92)

$$\delta^2 H'^*_{ord}(z_i^*, z_j) = H_{ord}(z_i^*, z_j) - H_{ord}(z_j^*, z_j) - \frac{\partial H_{ord}(z_j^*, z_j)}{\partial z_j^*}(z_i^* - z_j^*). \quad (5.97)$$

The corresponding matrix forms of (5.95) and (5.96) are given by

$$\Omega \mathbf{E}\dot{\mathbf{D}} = -\frac{i}{\hbar}\left(\Omega \cdot \delta^2 H'^*\right)\mathbf{E}\mathbf{D} = -\frac{i}{\hbar}\delta^2 \mathbf{H}'^* \mathbf{E}\mathbf{D}, \quad (5.98)$$

and

$$\dot{\mathbf{D}} = -\frac{i}{\hbar}\mathbf{E}^*\Omega^{-1}\left(\Omega \cdot \delta^2 H'^*\right)\mathbf{E}\mathbf{D} = -\frac{i}{\hbar}\mathbf{E}^*\Omega^{-1}\delta^2 \mathbf{H}'^* \mathbf{E}\mathbf{D}, \quad (5.99)$$

where $\mathbf{D}$ is a $1 \times n$ column matrix, the others are $n \times n$ matrices. Ω is the overlap matrix and Ω^{-1} is its corresponding inverse matrix. $\mathbf{E}$ is a diagonal matrix as defined previously, and

$$\delta^2 \mathbf{H}'^*_{ij} = \Omega_{ij}\delta^2 H'^*_{ord}(z_i^*, z_j). \quad (5.100)$$

Through numerical calculations, we found that this new expression, instead of C_i, can effectively avoid the singularity problem of the inverse of the overlap Ω^{-1} matrix during the time propagation. In fact, from Eq. (5.93) we can see that instead of calculating the inverse of the overlap in Eq. (5.84) at each time step, one only needs the inverse of the overlap at the very beginning of the time propagation in order to obtain the initial coefficient $D_i(0)$ from $C_i(0)$ through Eq. (5.94). At the same time, this expansion will also improve numerical computing efficiency. In fact, as has been pointed out by Burant [208], the algorithm (5.93) relates to an operator $\sum_{i=1}^{n}|z_i\rangle\langle z_i|$ which yields a scaling of $\approx n^2$, this is more favorable than (5.84) which relates to (5.83) and yields a scaling of n^3.

5.7 Propagation of the CSR wave function

From the previous statement we can see that several quantities have to be computed before obtaining the wave function, namely the time-dependent z_i, S_i and C_i or D_i, and all of them are related to the Hamiltonian in the CSR. Once the Hamiltonian and their initial values are obtained, these quantities can be determined by using the 4^{th} order Runge-Kutta method. This method is briefly

sketched below [112].

Consider an initial value problem expressed as

$$\dot{x} = f(x, t), \tag{5.101}$$

where x is an unknown function, either a scalar or a vector of time t, with the initial value $x(t_0) = x(0)$. Here, in our computation, x is related to the time-dependent z_i, S_i and D_i (or C_i). During the numerical calculation, assume that the time step is Δt, the time-dependent $x(t)$ can be obtained through

$$x(t_0 + \Delta t) = x(0) + \frac{\Delta t}{6}(r_1 + 2r_2 + 2r_3 + r_4), \tag{5.102}$$

where r_1, r_2, r_3 and r_4 are defined as

$$\begin{aligned} r_1 &= f(x(0), t_0), \\ r_2 &= f(x(0) + \Delta t/2r_1, t_0 + \Delta t/2), \\ r_3 &= f(x(0) + \Delta t/2r_2, t_0 + \Delta t/2), \\ r_4 &= f(x(0) + \Delta t r_3, t_0 + \Delta t). \end{aligned} \tag{5.103}$$

The initial $z_i(0)$ are constructed through Eq. (5.48) by choosing a group of initial conditions $(q_i(0), p_i(0))$, which is also called the initial sampling. Theoretically, the initial sampling used to sample the basis of the CSs can be selected randomly, however, the better it is selected, the more accurate the initial wave function will be represented. For example, if the initial wave function used for the propagation is a Gaussian wave packet itself, i.e. $|\Psi(0)\rangle = |z_c\rangle$, the initial sampling can be selected centered around the maximum of this initial wave function from a Gaussian distribution

$$F(z) \propto \exp\left(\alpha |z - z_c|^2\right). \tag{5.104}$$

where α is a "compression" parameter describing the width of the basis set distribution. More details about how to select the initial sampling through this distribution can be found from Refs. [95, 190], and how to choose the initial sampling for our simulation will be shown in Chapter 7. Furthermore, from Eq. (5.61) one can see that the initial $S_i(0) = 0$. However, $C_i(0)$ depends on the initial wave function $\Psi(x, 0)$ and can be obtained from Eqs. (5.53) and (5.71). Several computational methods can be applied and specific examples relating to this are discussed in the rest of this thesis.

Chapter 6

Phase-space dynamics of a wave packet in strong fields with IVRs

As has been pointed out in the introduction of the second part of this thesis, the IVR methods have been widely applied to many areas of science, but only a small number of publications in strong-field physics were reported. Particularly, the HK propagator has been applied to the computation of the HHG spectra in [26–28], the CCS method has been employed for the simulation of NSDI and constructing electron momentum distributions in [96, 98, 99]. In order to apply these methods widely, major challenges must be overcome. For instance, in the HK propagator, the tunnel ionization may not be properly accounted for, since the trajectories used for the construction of the time-dependent wave function are real and therefore they cannot cross the classically forbidden regions in phase space.

In fact, since the 1990s, there has been considerable debates about whether semi-classical IVR methods, such as the HK propagator can be employed to model tunneling, and if so, to what extent [181–184]. Spath and Miller have employed IVR methods to obtain tunneling probabilities which are dependent on a Gaussian width parameter entering their expressions [212]. Grossmann and Heller found that the tunneling probabilities are dependent on the center positions of Gaussians describing initial and final asymptotic states for scattering. If the initial center is moved far away from the barrier there is no tunneling. For a moderate displacement of the initial center from the barrier top, a qualitative

description of tunneling and the dependency of the tunneling rate on energy can be obtained [182]. Kay has explicitly noted that the straightforward applications of the IVR method failed for the treatment of the tunneling dynamics in systems such as the 1D double well [213]. On the other hand, because CCS is a basis-set quantum method, this method can be in principle employed to model tunneling. However, in order to properly model tunneling, special effort must be made for the selection of a suitable trajectory-guided basis .

As mentioned in the introduction of this thesis, tunneling is important in strong-field physics. The atomic potential is modified by the presence of the laser field, which forms a potential barrier that the initial wave packet has to tunnel through (the first step of the TSM in HHG processes). In order to circumvent the tunneling problem in HHG, initial electronic wave packets starting far away from the core have been studied in Refs. [26–28]. However, if the initial wave packet is placed at the origin, one may ask whether the over-the-barrier dynamics is sufficient for the modeling of strong-field wave packet dynamics. This is a legitimate question, especially if one considers that classical models, in which an ensemble of classical electrons being released in the continuum at different times within a field cycle was used to mimic the behavior of the electronic wave packet, have been hugely successful in reproducing a number of features in ATI [31] and NSDI [29, 30]. In some of these methods, tunnel ionization has been mimicked by employing the quasi-static Ammosov-Delone-Krainov (ADK) tunneling rate, which may explain the success. However, there exist purely classical models where the electron ensemble is left to propagate without the need for any ad-hoc quantum mechanical ingredients. To illustrate this, we perform a systematic analysis of the dynamics of an electronic wave packet in a strong field, with particular focus on ionization, and on what is left out by IVRs. This analysis is performed in phase space, for reduced dimensionality models, under the assumption that the electronic wave packet is initially bound. As a benchmark, full solutions from the TDSE are used for comparison.

Specifically, this chapter is organised as follows. Section 6.1 briefly sketches the derivation of the HK propagator and outlines the similarities and differences between quantum and semiclassical IVRs. Section 6.2 shows a brief comparison

between the CCS and the classical trajectories. In Section 6.3, we have a closer look at how the time-dependent wave packet overcomes the potential barrier resulting from the combined action of the external field and the binding potential. For this purpose, the quasiprobability distributions in phase space, from both the HK and the CCS methods, are employed to study the 1D model potential in a static field. Finally, Section 6.4 shows the conclusions.

6.1 Semiclassical IVRs

Although quantum mechanics is usually in coordinate or momentum space, it can also be formulated in phase space. Exclude the quantum IVR method (the CCS) present in the previous chapter, in this section we briefly present the semiclassical IVR method, namely, the HK propagator, in the phase space.

In the phase space, the HK wave function is expressed as [82]

$$|\Psi_{\mathrm{HK}}(t)\rangle = \iint |q,p\rangle R(t,q_0,p_0)\langle q_0,p_0|\Psi(0)\rangle \mathrm{e}^{\frac{\mathrm{i}}{\hbar}S_{\mathrm{cl}}} \frac{\mathrm{d}q_0\mathrm{d}p_0}{2\pi}, \tag{6.1}$$

where $|q,p\rangle$ represents a CS whose expression in coordinate representation is given by

$$\langle x|q,p\rangle = \left(\frac{\gamma}{\pi}\right)^{1/4} \exp\left[-\frac{\gamma}{2}(x-q)^2 + \frac{\mathrm{i}}{\hbar}p(x-q)\right], \tag{6.2}$$

which differs from Eq. (5.49) employed in the CCS approach by a phase factor, and

$$R(t,q_0,p_0) = \frac{1}{2^{1/2}}\left(m_{pp} + m_{qq} - \mathrm{i}\hbar\gamma m_{qp} + \frac{\mathrm{i}}{\hbar\gamma}m_{pq}\right)^{1/2} \tag{6.3}$$

is given in terms of the elements $m_{uv} = \partial u/\partial v_0$ of the monodromy matrix, which is composed of the derivatives of the final variables q, p with regard to their initial values q_0, p_0. In Eq. (6.1), the action reads as

$$S_{\mathrm{cl}}(q,p) = \int (p\dot{q} - H_{\mathrm{cl}})\, dt, \tag{6.4}$$

where

$$H_{\mathrm{cl}} = H_{\mathrm{cl}}(p,q) = \frac{p^2}{2} + V(q) + qE(t) \tag{6.5}$$

is the classical Hamiltonian corresponding to (5.64), in which the operators $\hat{x}$, $\hat{p}$ have been replaced by the phase-space variables q, p. The initial wave packet considered here is

$$\langle q_0, p_0|\Psi(0)\rangle = \exp\left\{ -\frac{\gamma}{4}(q_\alpha - q_0)^2 - \frac{1}{4\gamma}(p_\alpha - p_0)^2 + \frac{\mathrm{i}}{2\hbar}(p_\alpha + p_0)(q_0 - q_\alpha)\right\}. \quad (6.6)$$

Originally, the HK propagator has been derived differently [82]. Nonetheless, both the CCS method and the HK propagator can be derived from the same source. By employing the local quadratic approximation, which only takes into account the first and second terms in the Taylor expansion of the potential energy around a specific trajectory, the HK propagator can be obtained from (5.91) [92]. This allows to use classical trajectories instead of those driven by the quantum averaged Hamiltonian $H_{\mathrm{ord}}(z^*, z)$ and also to calculate the integrals in (5.91) analytically. More details about this can be referred to Ref. [92] and the references therein, here we only provide a brief sketch of the main results.

Based on the quadratic approximation stated above the resulting HK wave function may then be represented as

$$|\Psi_{\mathrm{HK}}(t)\rangle = \int |z\rangle \sqrt{M_{zz}} \mathrm{e}^{\frac{\mathrm{i}}{\hbar} S_z^{\mathrm{cl}}} \langle z_0|\Psi(0)\rangle \frac{\mathrm{d}^2 z_0}{\pi}, \quad (6.7)$$

where $\sqrt{M_{zz}}$ denotes the HK prefactor in the z notation. In this notation M_{zz} is a single element of the monodromy (or stability) matrix

$$\mathbf{M} = \begin{pmatrix} M_{zz} & M_{zz^*} \\ M_{z^*z} & M_{z^*z^*} \end{pmatrix}, \quad (6.8)$$

which describes how stable the dynamics around a specific trajectory is. The monodromy matrix elements in this representation are related to those in the p, q representation as

$$\begin{aligned} M_{zz} &= \frac{1}{2}(m_{qq} + m_{pp} - \mathrm{i}\hbar\gamma m_{qp} + \frac{i}{\hbar\gamma} m_{pq}), \\ M_{zz^*} &= \frac{1}{2}(m_{qq} - m_{pp} + \mathrm{i}\hbar\gamma m_{qp} + \frac{i}{\hbar\gamma} m_{pq}), \\ M_{z^*z} &= \frac{1}{2}(m_{qq} - m_{pp} - \mathrm{i}\hbar\gamma m_{qp} - \frac{i}{\hbar\gamma} m_{pq}), \\ M_{z^*z^*} &= \frac{1}{2}(m_{qq} + m_{pp} + \mathrm{i}\hbar\gamma m_{qp} - \frac{i}{\hbar\gamma} m_{pq}). \end{aligned} \quad (6.9)$$

The evolution of the monodromy matrix is given by the matrix of second derivatives of the Hamiltonian

$$\frac{\mathrm{d}\mathbf{M}}{\mathrm{d}t} = -\frac{i}{\hbar}\begin{pmatrix} \partial^2 H_{cl}/\partial z^*\partial z & \partial^2 H_{cl}/\partial z^{*2} \\ -\partial^2 H_{cl}/\partial z^2 & -\partial^2 H_{cl}/\partial z^*\partial z \end{pmatrix}\begin{pmatrix} M_{zz} & M_{zz^*} \\ M_{z^*z} & M_{z^*z^*} \end{pmatrix}. \tag{6.10}$$

For the HK propagator, the time-dependent wave function is once again expressed in terms of Gaussians in phase space (details have been discussed in Refs. [82, 83, 214, 215]). Following the original work [82], rather than labeled by a single complex number z in the CCS method, the HK propagator normally expresses these Gaussians by two real numbers p and q [see Eq. (6.1)]. In the p, q-notation, comparing the Gaussian (6.2) with (5.49), one can see that the phase prefactor i$pq/2\hbar$ in (5.49) has been removed. In fact, this is due to that i$pq/2\hbar$ in (5.49) is compensated by the different form of the classical action (6.4) as opposed to that of (5.61).

Although the CCS method and HK propagator share the same origin, they are different in several ways. Apart from trivial notations, there are three main differences:

(1) The CCS representation is formally an exact basis-set technique. The coupled quantum equations are used for the coefficients $D_z(t)$, which can be obtained simply by substitution of (5.93) into the Schrödinger equation to propagate the wave function (5.93). In contrast, in the HK theory an analytical semiclassical formula with elements of the monodromy or stability matrix is applied to obtain the coefficients. These expressions result from the so called local quadratic approximation, which only takes into account the first and second terms in the Taylor expansion of the potential energy around a specific trajectory, and assumes that only the coupling of CSs near this trajectory is important. Physically, this implies that each trajectory in the swarm employed in the HK method contributes independently, while in the CSR the trajectories are coupled through the amplitudes $D_z(t)$. Indeed, for each trajectory there is one prefactor, which depends only on the information carried by that specific trajectory.

(2) On a more technical level, the CCS approach is often used in conjunction with various basis-set expansion algorithms, it generates additional basis functions and reprojects the wave function on the new basis-sets. These adaptive basis-set technique allow the CCS method to describe complicated features of the dynamics more efficiently. Reprojection has also been used in conjunction with the HK method, however, this is much less common [207, 208].

(3) The trajectories of the Gaussian CSs in the HK method are purely classical, while in CCS the trajectory of a CS is driven by the Hamiltonian $\langle z|\hat{H}|z\rangle$. This latter Hamiltonian is the average of the quantum Hamiltonian with regard to the CSs, and takes into account the local zero-point energy and further corrections due to commutators. This makes all wells more shallow and lowers all potential barriers. The CCS and HK trajectories are identical only in the case of a harmonic potential.

For the first difference, it can be easily understood from the main theory of CCS in Chapter 5. The application of the reprojection in the second difference, will be fully discussed in the next chapter. In the following section we give an example to show the difference between the CCS trajectory and the HK trajectory in the coordinate and momentum space.

6.2 The CCS and classical trajectories

In order to show the differences between the CCS and the classical trajectories, we take a 1D model potential in an external laser field as an example. In theoretical physics, the most widely used 1D model potential is the soft-core potential, because it can remove the singularity of the Coulomb potential. However, unfortunately, even though the CCS can effectively treat the singularity appearing in the 3D Coulomb potential, the 1D form of it or the soft-core potential can not be treated analytically in the CSR (this is discussed in the next chapter and the Appendix). Thus a short-range Gaussian potential $V_g(x) = -e^{-\lambda x^2}$ will be used to replace the soft-core potential $V_{sc}(x) = -\frac{a}{\sqrt{x^2+b}}$ for the 1D simulation in this thesis. Despite of being a simple expression, it contains all of the main physical features appearing in strong-field physics phenomena.

The corresponding 1D Hamiltonian is written as

$$\hat{H} = \frac{\hat{P}^2}{2m} + V_g(\hat{x}) + \hat{x}E(t), \tag{6.11}$$

where, the first term is the kinetic energy, the second term is the 1D Gaussian potential, and the last term is the interaction between the electron and the external laser field $E(t)$ (Note that, the sign preceding $xE(t)$ used in Eq. (2.6) is "-", rather than "+". However, the main results will not be changed regardless of the sign convention.). The kinetic energy in the CSR can be written in the following form

$$\begin{aligned}
\langle z_i|\frac{\hat{P}^2}{2m}|z_j\rangle &= -\frac{\hbar^2\gamma}{4m}\langle z_i|\hat{z}^{\dagger 2} - \hat{z}^\dagger\hat{z} - \hat{z}\hat{z}^\dagger + \hat{z}^2|z_j\rangle \\
&= -\frac{\hbar^2\gamma}{4m}\langle z_i|\hat{z}^{\dagger 2} - 2\hat{z}^\dagger\hat{z} - 1 + \hat{z}^2|z_j\rangle \\
&= -\frac{\hbar^2\gamma}{4m}(z_i^{*2} - 2z_i^* z_j - 1 + z_j^2)\langle z_i|z_j\rangle.
\end{aligned} \tag{6.12}$$

Note that in the above derivation, the following commutator is applied

$$\left[\hat{z}_i, \hat{z}_j^\dagger\right] = \delta_{ij}. \tag{6.13}$$

In the CSR, the 1D Gaussian potential is represented as (the derivation of this can be referred to the 3D Gaussian potential in the CSR, which is shown in the Appendix)

$$\langle z_i|e^{-\lambda x^2}|z_j\rangle = \langle z_i|e^{-\frac{\lambda\hbar}{2m\omega}\left(\hat{z}^{\dagger 2}+\hat{z}^2+2\hat{z}^\dagger\hat{z}+1\right)}|z_j\rangle \quad = -\left(\frac{\gamma}{\gamma+\lambda}\right)^{1/2} e^{-\frac{\lambda\gamma}{\gamma+\lambda}\rho^2}\langle z_i|z_j\rangle \tag{6.14}$$

For the 1D system, the last laser field term of Hamiltonian in the CSR can be easily obtained as

$$\langle z_i|\hat{x}E(t)|z_j\rangle = \langle z_i|\sqrt{\frac{\hbar}{2m\omega}}(\hat{z}^\dagger + \hat{z})E(t)|z_j\rangle = \rho E(t). \tag{6.15}$$

Note that, in Eqs. (6.14) and (6.15), $\rho = \frac{z_i^* + z_j}{\sqrt{2\gamma}}$. Therefore, the $H_{ord}(z_i^*, z_j)$ related

to the CCS trajectory (5.69) can be written as

$$\begin{aligned} H_{ord}(z_i^*, z_j) &= -\frac{\hbar^2\gamma}{4m}(z_i^{*2} - 2z_i^* z_j - 1 + z_j^2) - \left(\frac{\gamma}{\gamma+\lambda}\right)^{1/2} e^{-\frac{\lambda\gamma}{\gamma+\lambda}\rho^2} + \rho E(t) \\ &= \frac{\hbar^2\gamma}{4m} + \frac{p^2}{2} - \left(\frac{\gamma}{\gamma+\lambda}\right)^{1/2} e^{-\frac{\lambda\gamma}{\gamma+\lambda}\rho^2} + \rho E(t). \end{aligned} \tag{6.16}$$

Considering the diagonal part ($i = j$) of Eq. (6.16), one can obtain the derivative of CS z_i

$$\begin{aligned} \frac{\mathrm{d}z_i}{\mathrm{d}t} &= -\frac{i}{\hbar}\frac{\partial H_{ord}(z_i^*, z_i)}{\partial z_i^*} \\ &= -\frac{i}{\hbar}\left[-\frac{\hbar^2\gamma}{2m}z_i^* + \frac{\hbar^2\gamma}{2m}z_i + \frac{\sqrt{2}\gamma\lambda}{(\gamma+\lambda)^{3/2}}\rho e^{-\frac{\lambda\gamma}{\lambda+\gamma}\rho^2} + \frac{E(t)}{\sqrt{2\gamma}}\right]. \end{aligned} \tag{6.17}$$

Applying the 4^{th} order Runge-Kutta method to this equation, one might get the time evolution of z_i. The time-dependent CCS trajectory and momentum are represent as

$$q = \sqrt{\frac{1}{2\gamma}}\,(z + z^*) \tag{6.18}$$

and

$$p = i\hbar\sqrt{\frac{\gamma}{2}}\,(z - z^*)\,. \tag{6.19}$$

Corresponding time-dependent classical trajectory and momentum can be obtained from

$$\dot{p} = -\partial H_{cl}(p, q)/\partial q \tag{6.20}$$

and

$$\dot{q} = \partial H_{cl}(p, q)/\partial p, \tag{6.21}$$

where

$$H_{cl}(p, q) = \frac{p^2}{2} - \exp\left(-\lambda q^2\right) + qE_0 \tag{6.22}$$

is the classical Hamiltonian.

Fig. 6.1 shows the trajectories obtained through the CCS Eqs. (6.18) and (6.19) and the classical (HK) computation (6.20) and (6.21), with the same initial position and momentum for a 1D Gaussian potential in an external laser field. For the sake of clarity, we will provide a few definitions which have been introduced

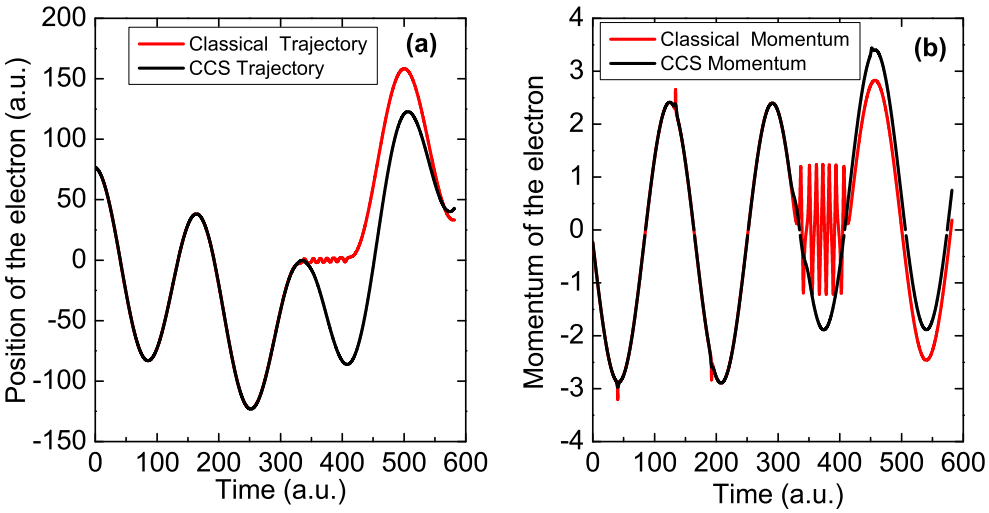

Figure 6.1: Time-dependent trajectories and momentum of the 1D Gaussian potential: $V_g(x) = -\exp(-0.5x^2)$ from both the CCS and the classical solutions, in the external laser field $E(t) = E_0 \cos(\omega_0 t)$ with $E_0 = 0.1$, $\omega_0 = 0.0378$. Panel (a) shows the trajectories from both the CCS (the black line) and the classical solution (the red line) with the initial position $q_0 = 76.72464472$. Panel (b) shows the corresponding momentum with the initial value $p_0 = -0.232201645$.

in Ref. [26], where van de Sand and Rost showed for the HK propagator is used, there are two types of trajectories whose interference leads to the HHG plateau. The first type of trajectories are the regular trajectories, which are not slowed down when passing the nucleus (i.e. $x = 0$), and the second are the time-delayed trajectories. The time-delayed trajectories can be further divided into two subgroups: the "trapped" trajectories, which get trapped over a fraction of a field cycle and oscillate around the nucleus [the red line shown in panel (a)]; and the "stranded" trajectories (this is not shown in the present figure), which are on top of the barrier of the effective potential $V_{eff}(x,t) = V(x) + xE(t)$ [where, $E(t)$ is the external laser field] and just slow down but not get trapped as they pass the nucleus.

From this figure we can clearly see that the "trapped" trajectory, which is ad-

vocated in [26], is obtained from the classical computation with high frequency oscillations around the end of the 2nd laser cycle (around 330 a.u., the laser cycle is $2\pi/\omega_0 \simeq 166.2$). We note that with the same initial condition, the trajectory from the CCS is quite different, the CCS trajectory is not "trapped". Before the trajectory is trapped by the core, the CCS result has a perfect agreement with that from HK, however difference between the two methods starts to appear after the trajectory is trapped. At the same time, from the time-dependent momentum in panel (b) we can see that before the trapping, the positions of the spikes observed in momentum coincide under both the HK and CCS methods. The main difference is that the spikes from the CCS computation are not so sharp, and high frequency oscillations similar to those presented in the classical results are absent in the CCS computation [panel (b)]. Comparing panel (b) to panel (a), one can find that the spikes only appear at the time when the position of the trajectory equals zero, hence, our understanding of these spikes in the time-dependent momentum are due to the immediate increase in attraction force between the nucleus and the electron as the electron passes the core. The reason why the spikes from CCS are not so sharp as those in the classical computation might be a result of introducing quantum corrections of the Hamiltonian by the CCS method. Comparing Eqs. (6.9) and (6.15), we can find an effective energy shift $\gamma/4$ and a shift of

$$\Delta V_g(q) = V_g(q) \left[\left(\frac{\gamma}{\gamma + \lambda} \right)^{1/2} \exp\left\{ \frac{\lambda^2 q^2}{\gamma + \lambda} \right\} - 1 \right] \tag{6.23}$$

in the binding potential between $H_{ord}(p, q)$ and $H_{cl}(p, q)$, where $V_g(q)$ is the 1D Gaussian potential. For discussions of these shifts see [88].

6.3 Phase-space dynamics

In this section, we wish to analyse the different ionization mechanisms in phase space. According to the quasi static tunneling picture, a low frequency time-dependent field and the binding potential together determine an effective potential barrier

$$V_{eff}(x, t) = V_g(x) + xE(t), \tag{6.24}$$

whose maximum is given by $V_{eff}(x_s, t)$ at the coordinate x_s, where, the value of x_s can be calculated through $\partial V_{eff}(x,t)/\partial x|_{x=x_s} = 0$. If the total electron energy is larger than this value, it may escape via over-the-barrier ionization. If the total energy is smaller, tunneling is expected to be the dominant ionization mechanism.

6.3.1 Phase portraits and classical trajectory analysis

With the above aim in mind, both the classical trajectories used to construct the wave function in Eq. (6.1) and the CCS trajectories [from Eq. (6.17)] applied to construct the wave function (5.88) are analysed in the phase space. For simplicity, only the electron exposed to a static field is studied. In Fig. 6.3, we present

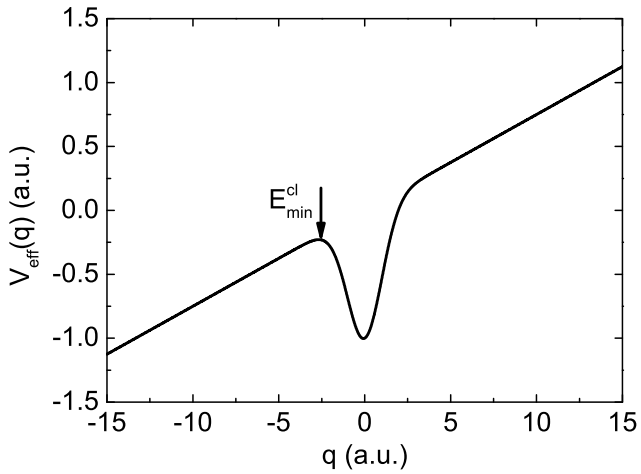

Figure 6.2: Schematic plot of the effective potential of the 1D Gaussian potential $V_g(q) = \exp(-0.5q^2)$ in the static field, with strength $E_0 = 0.075$. E^{cl}_{min} is the minimal energy that the electron needs to escape via over-the-barrier ionisation, which is also used to define the classical separatrix in Fig. 6.3. Similar definition of the CCS separatrix can be obtained from the effective potential in the CSR.

the phase portrait of the system for the Hamiltonian (6.11) in static fields with different intensities. The left panels in this figure show that a separatrix, defined by the condition $p^2/2 + V_g(q) + E_0 q = E^{cl}_{min}$ with E^{cl}_{min} the classical minimal

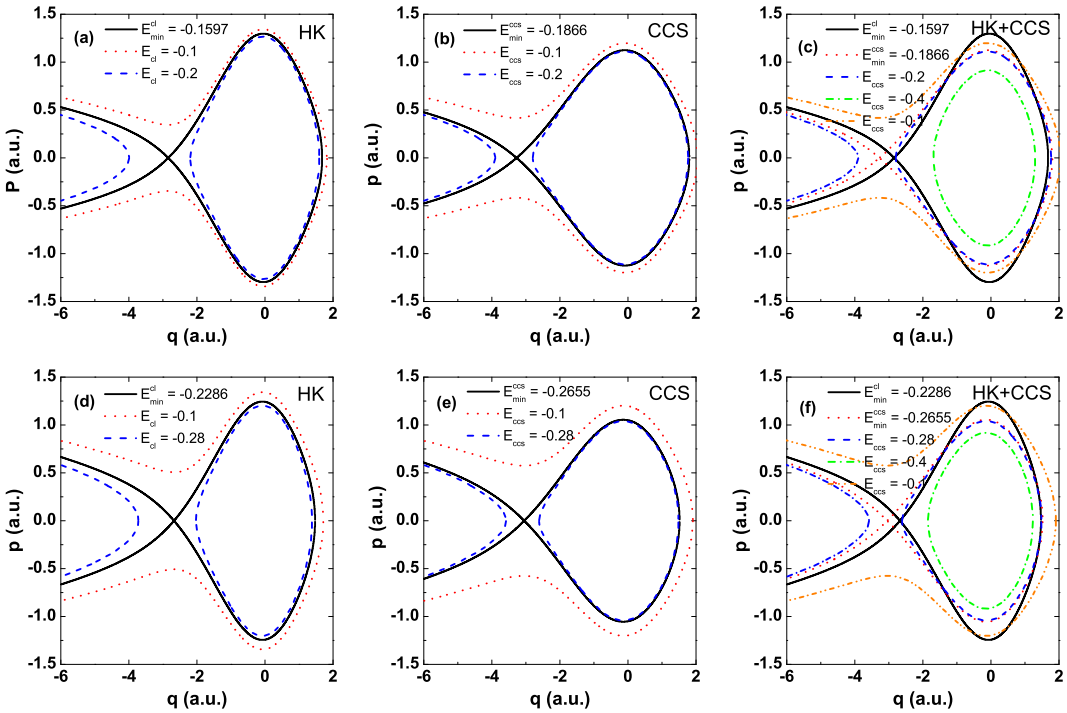

Figure 6.3: Phase portrait of the 1D Gaussian potential $V_g(q) = \exp(-0.5q^2)$ defined from the classical and CCS methods. The left panels are the classical trajectories used in the computation of the HK propagator, in which, the solid black lines are the separatrix with minimal energy; the middle panels are the trajectories from the CCS, the solid black line in these panels are the separatrix defined from the CCS; in the right panels, we combine the trajectories from both the classical (HK) and the CCS computation, the black solid and the red dot lines are the corresponding separatrices from these two methods (i.e., the solid black lines in the left and middle panels, respectively). Here, two different static fields are considered, in the upper panels is $E_0 = 0.05$, in the lower panels is $E_0 = 0.075$.

energy necessary for the electron to undergo over-the-barrier ionization, crossing at $(q, p) = (q_s, 0)$. The illustration related to the E^{cl}_{min} is shown in Fig. 6.2.

For energies E below the separatrix energy the dynamics can be either bound

or unbound depending on whether the spatial coordinate of the orbit is larger or smaller than that of the saddle point $(q_s, 0)$. This means that an orbit with $E_{cl} < E_{min}^{cl}$ will remain unbound if its initial spatial coordinate q_0 lies on the left-hand side of the saddle point, and that it will remain bound if q_0 lies on the right-hand side of q_s and never crosses this region. On the other hand, orbits with $E > E_{min}^{cl}$ will remain unbound regardless of the initial value of their spatial coordinates.

Furthermore, from Fig. 6.3, one can see that the CCS trajectories behave differently from those obtained from classical computation. As shown in the middle panels of this figure, if the separatrix is however defined through the Hamiltonian in the CSR instead of the classical Hamiltonian, similar behaviors to those found in the left panels will be observed. Namely, the trajectories with energy lower than the minimal energy E_{min}^{ccs}, defined by the CCS method, will not cross the forbidden region. Consequently, the trajectories with energy higher than the minimal energy will remain in the "unbound" region. Note that, the "bound" and "unbound" refer to the energy of a trajectory defined in the CSR being lower or higher than the separatrix energy, which is different from the classical definition.

If we define the separatrix using the classical Hamiltonian, different behaviors will appear. As presented in the right panels of Fig. 6.3, several kinds of properties can be observed. First, some of the trajectories with energies less than E_{min}^{ccs} in the CCS definition will cross the separatrix. If the initial positions of this kind of trajectories are on the left hand side of the CCS separatrix, they will remain in this region and not cross either the CCS or the classical separatrix [the left part of the blue dash lines shown in panels (c) and (f)]. On the other hand, if the initial positions of the trajectories are on the right hand side of the CCS separatrix, depending on the initial energy of the trajectories, while some of them [the green dash dot lines in panels (c) and (f)] will remain bound in the classical definition, some of them [the right part of the blue dash lines in panels (c) and (f)] will cross the forbidden region defined by the classical Hamiltonian. This occurs even though they are still "bound" in the CCS definition and propagate along a closed orbit. Furthermore, trajectories with energy larger than or equal to E_{min}^{ccs} can be divided into two groups. 1) Those that can cross the classical separatrix

(including the CCS separatrix). For instance, the orange dash dot dot lines in the right panels of Fig. 6.3 and those trajectories with energies between E_{min}^{ccs} and E_{min}^{cl} (not shown in this figure), can propagate from the unbound region to the bound region, as well as evolve from the bound region to the unbound region. 2) And those that have much higher energies, remain in the unbound region and will never cross into the bound region (they are not shown in this figure). This means that tunneling, which is forbidden in the classical computation, is possible under the CCS method. This is because quantum correction of the Hamiltonian is introduced in $H_{ord}(z^*, z)$, which, compared to the classical Hamiltonian, has an energy shift (6.23).

6.3.2 Wigner quasiprobabilities

We now employ the Wigner quasiprobability distribution (also known as the Wigner function) to relate the above picture to the wave packet propagation in phase space [216]. This function is defined as

$$W(q,p) = \frac{1}{\pi}\int_{-\infty}^{+\infty} \mathrm{d}y \Psi^*(q+y)\Psi(q-y)\exp[2\mathrm{i}py], \tag{6.25}$$

where $\Psi(x)$ is the wave function obtained from either the TDSE or CCS in the coordinate space. If Eq. (6.25) is integrated over the momentum or position space, the corresponding probability densities are recovered. Strictly speaking, the Wigner distribution cannot be associated with a propability density, since it can exhibit both positive and negative values, while the probability density represents the possibility of finding an electron in a specific region which is always a nonnegative value. Nonetheless, it does give an intuitive picture of the wave packet dynamics in phase space, and provides valuable information about momentum-position correlation. In order to access the dynamics of ionization [217], rescattering [218, 219], double ionization [220] and HHG [221], Wigner distributions have been used in strong-field physics and widely employed in quantum optics. A tail, which has been associated with ionization, in Refs. [217] and [221], was identified as a common feature in Wigner distribution.

To make the above mentioned tail visually clearer and study why the tail is present in the HK method, in Fig. 6.4 we present the modulus square of the

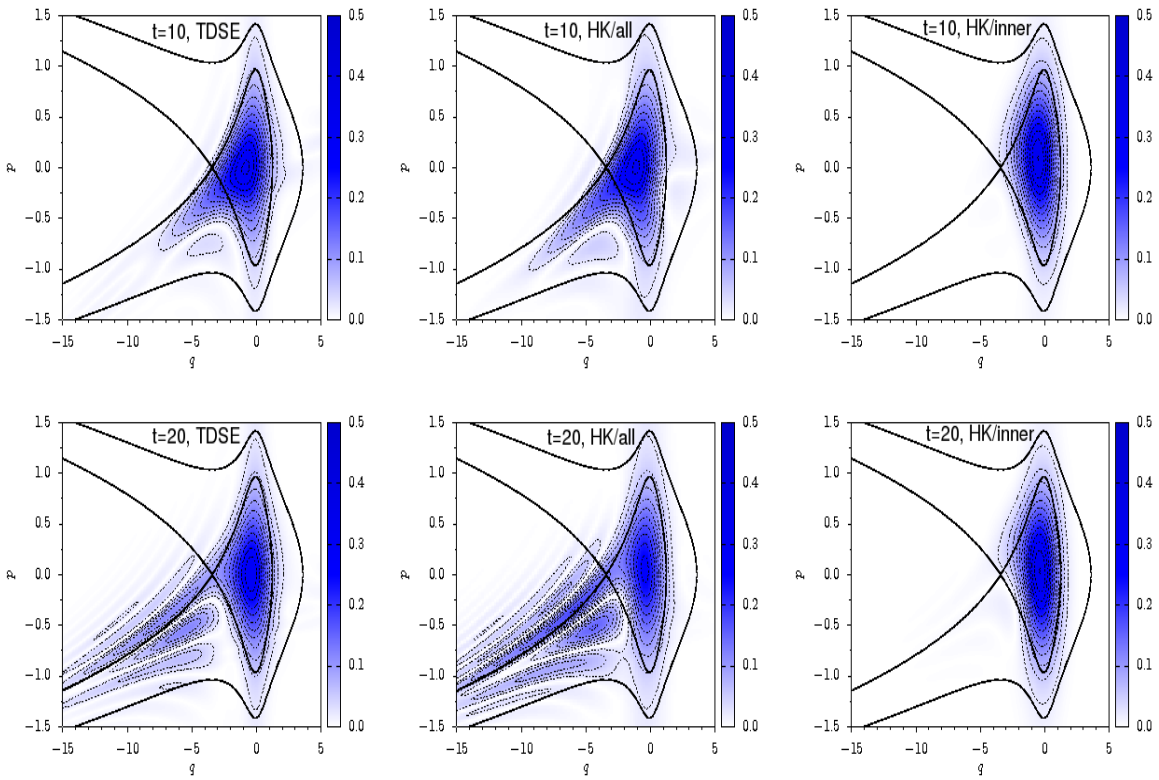

Figure 6.4: Modulus square of the Wigner quasiprobability distributions computed using a static field with the strength $E_0 = 0.075$ for a 1D soft-core potential $V_{sc} = -\frac{1}{\sqrt{x^2+1}}$ using the TDSE (the left panels) and the HK (the middle and right panels) for $t = 10$ (the upper panels) and $t = 20$ (the lower panels). The main difference between the middle and the right panels is that the trajectories whose initial coordinates (q_0, p_0) lie outside the bound phase-space region are not included in the right panels. The thicker lines show the separatrix and the phase space trajectory for $E = 0$. The initial wave packet used for the propagation is $\Psi(x, 0) = \left(\frac{\gamma}{\pi}\right)^{1/4} \exp\left(-\frac{\gamma}{2}x^2\right)$, with $\gamma = 0.5$.

Wigner quasiprobability distributions from both the TDSE and the HK propagator, respectively. From this figure one can clearly see that the time propagation of the wave packet, and particular the shape of the Wigner function, are strongly influenced by the separatrix. Throughout, the figure shows a distinct tail in the Wigner functions leaving the bound phase-space region. For short times the tail

follows the separatrix from below, as shown in the upper left and middle panels. This strongly suggests that the continuum is reached by over-the-barrier ionization: the electronic wave packet does not leave the core with vanishing momentum, but rather with the minimum necessary momentum to overcome $V_{eff}(q_s)$. As time progresses, interference fringes start to build up on the left-hand side just above the separatrix. These fringes have been identified in [217], for a delta-potential model in a static field, and in [218, 221] for long- and short-range potentials in time-dependent fields, and have been associated with the quantum interference of ionization processes occurring at different times. Apart from this, there is a pronounced tail now following the separatrix from above. This implies that parts of the wave packet are reaching the continuum with lower energy than that required for over-the-barrier ionization to occur. In other words, tunnel ionization may be taking place, both for the TDSE and the HK wave packets. Near $q = q_s$, the momentum at this tail is even approximately vanishing, in agreement with the model in [217]. A decrease in the momentum associated with the tail is intuitively expected as, physically, the components of the wave packet with lower energy will take longer to reach the barrier [183].

All of the features mentioned above are present in both the TDSE and the HK propagator computations. This is not surprising, as it is known that the HK propagator is capable of reproducing such effects. However, it seems that the semiclassical propagator allows the wave packet to cross classical forbidden regions. In other words, classical trajectories corresponding to over-the-barrier energy appear to mimic transmission through a barrier for $E < E^{cl}_{min}$. This is not obvious, as these trajectories do not violate any phase-space constraints, or cross classically forbidden regions.

We have however verified that the trajectories whose initial coordinates (q_0, p_0) lie outside the bound phase-space region lead to the tail in the Wigner distributions. For clarity, in the right panels of Fig. 6.4 we show the Wigner function computed from the HK propagator without these trajectories. In this figure, both the above-mentioned tail and the interference fringes are absent. These findings are in agreement with the results in [222], in which a nonlocal behavior of the Wigner function around separatrices has been observed for an inverted harmonic

oscillator, and with those in [223], which find that the transmission coefficient associated with a parabolic barrier is related to the quantum-mechanical weight of all classical trajectories with enough energy to go over the barrier. The disappearance of the fringes in the Wigner functions around $p = 0$ for $q < q_s$ also indicates that the Wigner function is non-local.

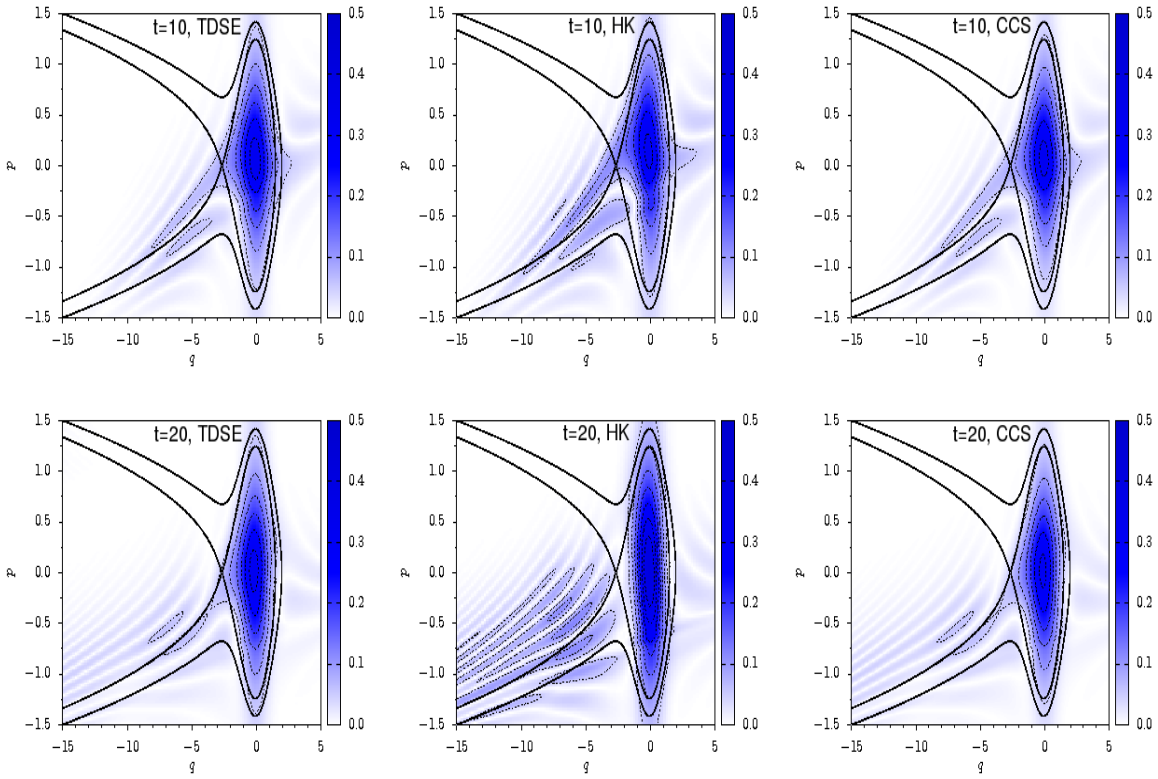

Figure 6.5: Modulus square of the Wigner quasiprobability distributions computed using a static field with the strength $E_0 = 0.075$ and the 1D Gaussian potential, using the TDSE, the HK propagator and the CCS method (left, middle and right panels, respectively). The upper and lower panels correspond to $t = 10$ and $t = 20$, respectively. Thicker lines show the separatrix and the phase-space trajectory for $E = 0$ from the classical computation. For the HK propagator and the CCS method we employ 10^7 and 1600 trajectories with reprojection, respectively.

Now we investigate the Gaussian potential and an initial wave packet $\psi(x,0) = \left(\frac{\gamma}{\pi}\right)^{1/4} \exp\left(-\frac{\gamma}{2}x^2\right)$ with $\gamma = 1$. For a short-range potential, the effective potential barrier is much steeper than for the soft-core potential and there is no Rydberg series. Hence, tunneling is expected to be dominant for the parameter range examined. Furthermore, we will perform a direct comparison of the results from the CCS method to those from the TDSE and the HK methods.

In Fig. 6.5, we display snapshots of $W^2(q,p)$ computed with the TDSE, the HK propagator and the CCS method (left, middle and right panels, respectively) using a static field. For $t = 10$ (upper panels) there is very good agreement between the outcomes of all approaches, with a distinct tail in the quasiprobability distribution following the separatrix from above. This behavior holds even for the results obtained using the semiclassical HK propagator. Physically, this suggests that there will be a nonvanishing probability density leaving the core with $|p| < |p_{min}|$. For $t = 20$, a longer tail extending to far beyond the core region and interference fringes are present in all cases. For these longer times, there appears to be less agreement between the HK propagator computation and the TDSE results. This is also the case (as we show separately in Fig. 6.6) with the standard CCS method, as in this region anharmonicities associated with the binding potential become more important. In order to overcome this problem, it is necessary to perform a periodic reprojection of the trajectories onto a set of regular grids. With the reprojection (we discuss this in detail in next chapter), a good, better than the HK propagator, agreement with the TDSE can be achieved through the CCS approach.

Once again, the better agreement between the CCS method and the TDSE is due to the fact that the trajectories employed in the HK propagator never cross the separatrix, while those used in the CCS method do. The quantum correction of the Hamiltonian is introduced in the CCS approach because of the application of the commutator and averaging the potential over a Gaussian CS basis, which leads to the lowering of the barrier and is effectively equivalent to partially taking tunneling into account.

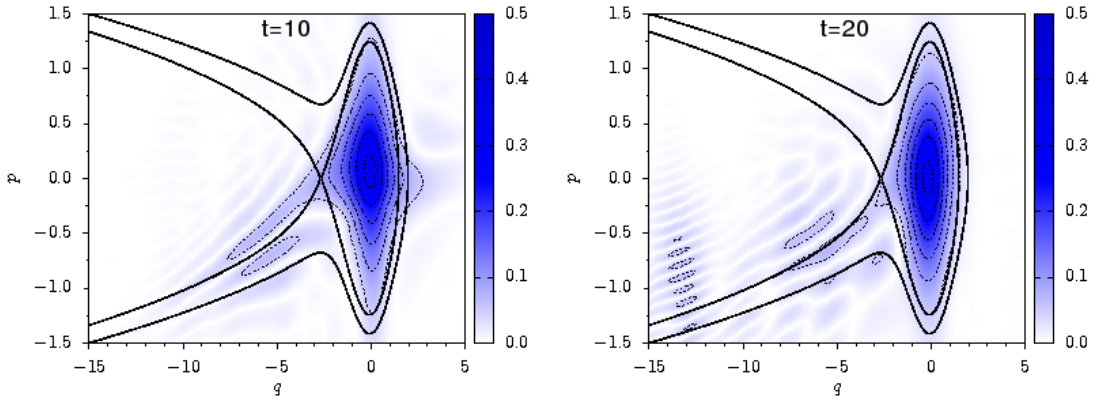

Figure 6.6: Modulus square of the Wigner quasiprobability distributions corresponding to the right panels of Fig. 6.5, but without the reprojection of the wave function to the initial grid. On the left hand side is the result from $t = 10$, and on the right hand side is that from $t = 20$.

6.4 Conclusions

In this chapter we have assessed the suitability of quantum and semiclassical IVRs, exemplified by the CCS method and the HK propagator respectively, for modeling the dynamics of an electronic wave packet in a strong field, assuming the wave packet is initially bound. By using a time-dependent laser field, we found that the trajectories used to construct the CCS wave function are different from those ones used in the HK propagator. Although the trajectories show a similar behavior and match very well up to about two laser cycles, the subsequent high frequency oscillations of the trajectory around the nucleus under the HK method does not appear in the CCS computation. This is because the trajectories of a CS are driven by the ordered Hamiltonian, which is the average of the quantum Hamiltonian with regard to the CSs, and this makes all wells more shallow and lowers all potential barriers. Through the phase portrait and trajectories analysis we find that the forbidden region defined in classical mechanics, cannot be crossed by the classical trajectories, while it can be crossed by the trajectories defined in the CCS method.

Applying Wigner quasiprobability distributions, we find that if the classical tra-

jectories starting outside the bound phase-space region are taken into consideration, the common feature of the presence of the tails in Wigner distribution can be observed. Depending on the momenta associated with these tail, it may be related to over-the-barrier or tunneling ionization. Similar tails have been identified in the literature, using either a zero range potential [217, 219] or the TDSE [221]. Therein, focus has been placed on how this tail behaves outside the core region, and on its agreement with classical trajectories as defined by the strong-field recollision model [16]. In this work, we place more emphasis on the position-momentum correlation in the vicinity of the core as evidence for different ionization mechanisms. On the other hand, if the classical trajectories starting outside of the bound phase-space region are removed, the tails in the Wigner functions disappear. This implies that they are an essential, and fully classical ingredient for reproducing these tails in the context of a semiclassical IVR. Furthermore, the disappearance of the tails in the Wigner function also support the assumption that the Wigner function is non-local.

Through direct comparison of the Wigner function, we find that good agreement with the full solution of the TDSE can be obtained from both the HK and the CCS IVRs. Our results also indicate that the HK propagator does not fully account for tunneling and over-the-barrier reflections. However, it is able to partly reproduce features associated with the wave packet crossing classically forbidden regions, despite of the fact that the trajectories employed in its construction always obey classical phase-space constraints. Moreover, we show that the CCS method represents a fully quantum IVR and accurately reproduces the results of a standard TDSE solver.

Chapter 7

Applications of the CCS method

In the previous chapter, the CCS method has been employed to the study of the phase-space dynamics of a wave packet, in this chapter we focus on how the CCS method may be applied to strong field physics. Specifically, this chapter is organised as follows. In order to define the initial values of the ensemble CSs used for the time propagation, we briefly show how to select the initial values in Section 7.1. To test the stability and convergency of the CCS method, we study the autocorrelation function (ACF) in Section 7.2. In Section 7.3, the reprojecting technique mentioned in Chapter 6, which periodically reprojects the wave function to a set of regular grids, is applied to solve the convergency problem of the CCS method. After that, in Section 7.4, we show how to calculate the dipole acceleration in the CSR. Finally, the HHG spectra obtained from different kinds of potentials, such as from the 1D Gaussian potential, 3D Gaussian potential and 3D Coulomb potential, are shown separately and compared in Section 7.5. The conclusions of this chapter are shown in Section 7.6.

7.1 Initial sampling

As mentioned in Section 5.7, theoretically, the initial sampling (initial values) used to construct the initial CSs and the time propagation can be selected randomly. However, in practice, we found that the results and accuracy of the CCS method strongly depend on the initial sampling, and therefore significant attention has to be paid to it. Especially for a 1D system, the results become very sensitive to initial sampling during the time propagation, because the transverse

wave packet spreading which leads to an over-enhancement of the interference effects is absent. For example, for a 1D system, if the initial sampling is generated through the normal distribution (as we mentioned in Section 5.7), very few CSs can be applied, otherwise the normalisation will diverse during the time propagation after a very short period of time. The main reason for that is that in a 1D simulation, the initial CSs obtained from a normal random number generator are too localised to sufficiently describe the wave function, during the time propagation, which might cause the divergence. Hence, if more CSs need to be considered, some technical changes are necessary to modify the parameters between different CSs in order to avoid this divergence. However, as the spacing between the CSs increases, most CSs move far away from the origin, which means that these CSs will propagate as free particles in the laser field and will contribute very little to the wave function. One of the effective ways to solve this divergence problem is to use a set of grid points with equal spacing, where the spacing can be adjusted according to the number of CSs employed (the more CSs are used, the larger the spacing is selected), and the initial norm of the wave function can be used as a criteria for selection of the spacing.

Specifically, the main initial sampling used for the simulation in this chapter is a set of 80×20 grids, symmetrically distributed around $(q, p) = (q_c, p_c)$ with spacing $\mathrm{d}q = 1.75\sqrt{2/\gamma}, \mathrm{d}p = 1.75\sqrt{2\gamma}$ in the (q, p) phase space. In fact, more CSs can be considered, however, this sampling appears to be large enough to reproduce the phenomena we are interested in the strong laser field, especially for the 1D system where our testing shows good quantitative agreement with the TDSE.

7.2 Autocorrelation function (ACF)

In order to test the convergence of the CCS method, we first consider the ACF $\langle\Psi(0)|\Psi(t)\rangle$, which in the coordinate space reads as

$$\int \Psi^*(x,0)\Psi(x,t)\mathrm{d}x, \tag{7.1}$$

where, $\Psi^*(x,0)$ and $\Psi(x,t)$ are the initial wave function and the wave function at time t, respectively.

The ACF in the CCS expression is obtained as following

$$\begin{aligned}\langle\Psi(0)|\Psi(t)\rangle &= \sum_i D_i^*(0)\exp\left[-\frac{i}{\hbar}S_i(0)\right]\langle z_i(0)|z_j(t)\rangle\sum_j D_j(t)\exp\left[\frac{i}{\hbar}S_j(t)\right] \\ &= \sum_{ij} D_i^*(0)\exp\left[-\frac{i}{\hbar}S_i(0)\right](\Omega_{0t})_{ij}\sum_j D_j(t)\exp\left[\frac{i}{\hbar}S_j(t)\right].\end{aligned} \tag{7.2}$$

Note that, two discrete CSR wave functions $|\Psi(t)\rangle$ (5.93) at time 0 and t are applied in (7.2). The corresponding matrix form of (7.2) is

$$\langle\Psi(0)|\Psi(t)\rangle = \mathbf{D}^{0*\top}\mathbf{E}^{0*}\Omega_{0t}\mathbf{D}\mathbf{E}, \tag{7.3}$$

where $\mathbf{D}^0$ is defined as the initial value of $\mathbf{D}$ and $\mathbf{D}^{0*\top}$ is the corresponding conjugate transpose matrix of $\mathbf{D}^0$, Ω_{0t} is the overlap between CSs at the time $t = 0$ and t, the definition of $\mathbf{D}$ and $\mathbf{E}$ are the same as those defined in Chapter 5.

Fig. 7.1 illustrates the real, imaginary and absolute values of the ACFs from the TDSE and the CCS method of the 1D Gaussian potential $V_g(x) = -\exp(-\lambda x^2)$ (in this thesis $\lambda = 0.5$ is selected, which corresponds to the ionisation energy $I_p = 0.594$) in an external laser field, with the initial sampling described in Section 7.1. The initial wave function applied here is a Gaussian wave packet [25–28]

$$\Psi(x,0) = \left(\frac{\gamma}{\pi}\right)^{1/4}\exp\left[-\frac{\gamma}{2}(x-q_c)^2 + \frac{i}{\hbar}p_c(x-q_c)\right], \tag{7.4}$$

centered at (q_c, p_c), and γ is defined as the width of the wave packet, which can be the same as that defined in the CSs. Apart from facilitating the implementation of IVR, this initial choice can also simplify the analytical computation. Because in the CR, a CS is also defined as a Gaussian wave packet (5.49), this initial wave function can be reduced in the same way as that of the CS in the CR to $\langle x|z_c\rangle$, as long as $p_c = 0$. The definition of z_c is

$$z_c = \sqrt{\frac{\gamma}{2}}q_c - \frac{i}{\hbar}\sqrt{\frac{1}{2\gamma}}p_c. \tag{7.5}$$

In Fig. 7.1 (a), we show the real part of the ACF. It is evident that a good quantitative agreement with the TDSE can be achieved through the CCS method

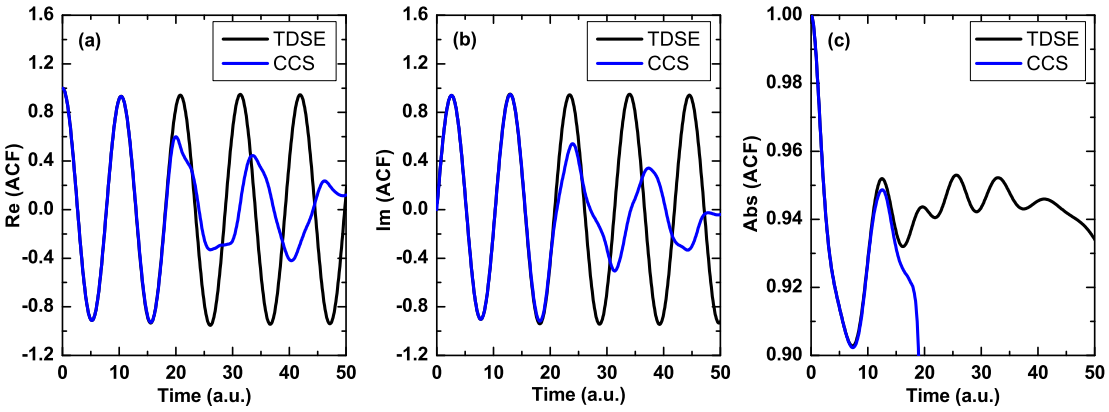

Figure 7.1: From the left to the right are the real, imaginary and absolute values of the ACF from the 1D Gaussian potential $V_g(x) = -\exp(-\lambda x^2)$ where $\lambda = 0.5$, with the initial wave packet Eq. (7.4) starting from the origin $(q_c, p_c) = (0, 0)$ and $\gamma = 1.0$, in an external laser field. The laser field employed here is $E(t) = E_0 \cos(\omega_0 t)$, with strength $E_0 = 0.1$ and frequency $\omega_0 = 0.05$. The black lines are the results from the TDSE, and the blue lines are those from the CCS computation.

for short time propagations (up to 20 a.u). However, after this time period the agreement between the two methods disappears quickly, a series of irregular oscillations and decrease of the amplitudes start to manifest. Similar problems are also found in the imaginary and absolute values of the ACF, especially for the absolute values where the disagreement becomes obvious very quickly.

In Fig. 7.2 we show the time-dependent wave function $|\Psi(x,t)|^2$ from both the CCS method and the TDSE. The wave function $\Psi(x,t)$ from the CCS method is calculated through

$$\Psi(x,t) = \langle x|\Psi\rangle = \sum_{i=1}^{n} \langle x|z_i\rangle d_i \exp\left(\frac{i}{\hbar} S_i\right). \tag{7.6}$$

As shown in this figure, the results from the CCS method match very well with those from the TDSE for a short time period up to 20 a.u.. From 30 a.u. onwards differences start to appear and intensify until the end of the propagation. In fact, from this figure we can see that the mismatch between the wave func-

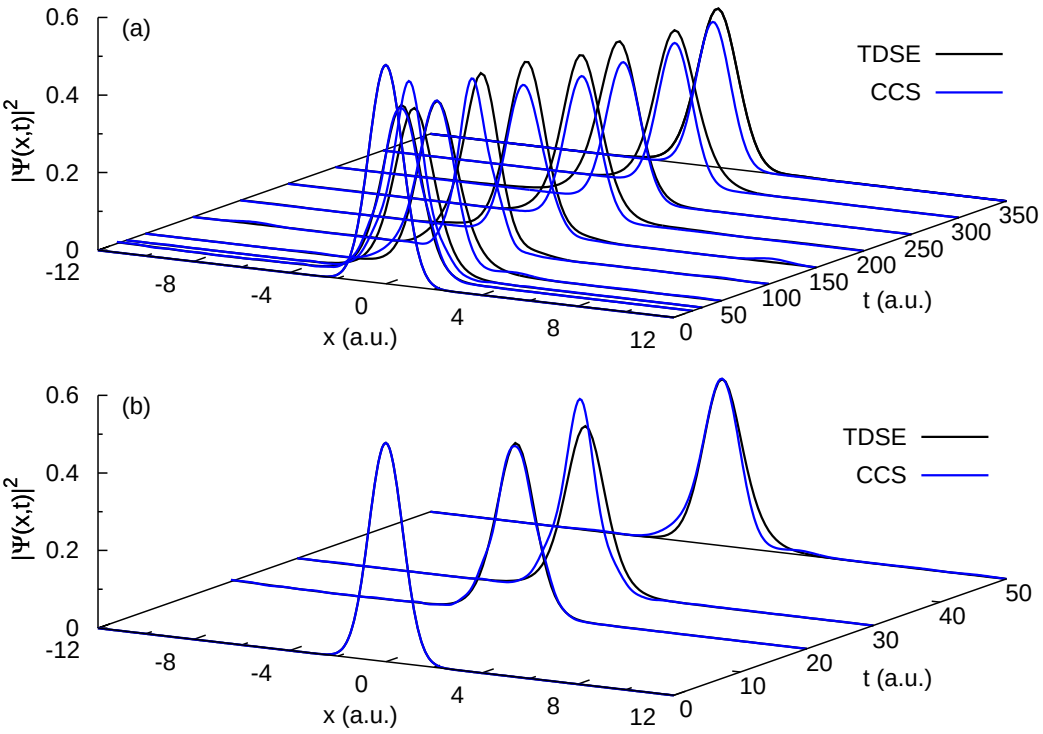

Figure 7.2: Panel (a): Time-dependent wave function from the TDSE and the CCS method, corresponding to Fig. 7.1. Panel (b): a snapshot of Panel (a). The black solid lines are the $|\Psi(x,t)|^2$ from the TDSE at different times; the blue solid lines are the corresponding results from the CCS method without the reprojection of the wave function.

tions is consistent with the ACF shown in Fig. 7.1. At the same time, from this figure one can clearly see that the CCS method works for short time propagation, but some numerical or convergency problems have to be resolved for long time propagation. In fact, as mentioned in the Ref. [207], Gaussian wave packet techniques in general, are accurate for short time propagations. The main problem is that for a longer time period the coupling between different CSs cannot persist, consequently, the trajectories will start to behave as free particles in propagation afterwards, and the overlap between the wave function trajectories and the initial grid points will be too small for the CCS dynamics to be calculated accurately. As mentioned in Section 7.1, one of the ways to overcome this problem is to choose an initial sampling which is large enough so that all of the required phase

space can be covered. However, in practice, this is very inefficient. The larger the space is, the more expensive the propagation will be. A similar and effective way to overcome this problem is one that has been applied in Refs. [207, 208], namely, performing a periodic reprojection of the trajectories onto static grids. This eliminates the need of using a huge space. Through our simulations, we find that the grid stated in Section 7.1 is large enough and produces observables that converge well to the accurate results (see below).

7.3 Reprojection of the wave function

Specifically, there are 4 steps to reproject the wave function to the initial grid.

(1) Use the 4^{th} order Runge-Kutta method stated in Section 5.7 to propagate Eqs. (5.69), (5.61), (5.96) and (5.93) from t_0 to t_1, one can obtain $z_i\left(t_1\right)$, $S_i\left(t_1\right)$, $d_i\left(t_1\right)$ and the wave function $|\Psi\left(t_1\right)\rangle$,

(2) Initialise the new *'initial'* $z_i'(0)$ and $S_i'(0)$ at time t_1 as $z_i(0)$ and $S_i(0) = 0$, respectively.

(3) Reproject the wave function to the initial CSs $|z_i\left(0\right)\rangle$ or $|z_i'\left(0\right)\rangle$, by combining Eqs. (5.71) and (5.93). The new *'initial'* $C_i'(0)$ can then be obtained through

$$\begin{aligned} C_i'(0) &= \langle z_i(0)|\Psi\left(t\right)\rangle \\ &= \sum_j \langle z_i(0)|z_j\left(t\right)\rangle d_j(t) \exp\left[\frac{i}{\hbar} S_j(t)\right]. \end{aligned} \tag{7.7}$$

(4) Calculate the new *'initial'* $d_i'(0)$ through Eq. (5.94) and the new *'initial'* $C_i'(0)$. After these steps one can go back to step (1) and continue the propagation.

Fig. 7.3 shows the recalculation of the ACF, corresponding to Fig. 7.1, with the reprojection of the wave function to the initial grids. From this we can see that instead of the dramatic decrease of the amplitudes and irregular oscillations in the real, imaginary as well as absolute value parts of the ACF from the CCS method,

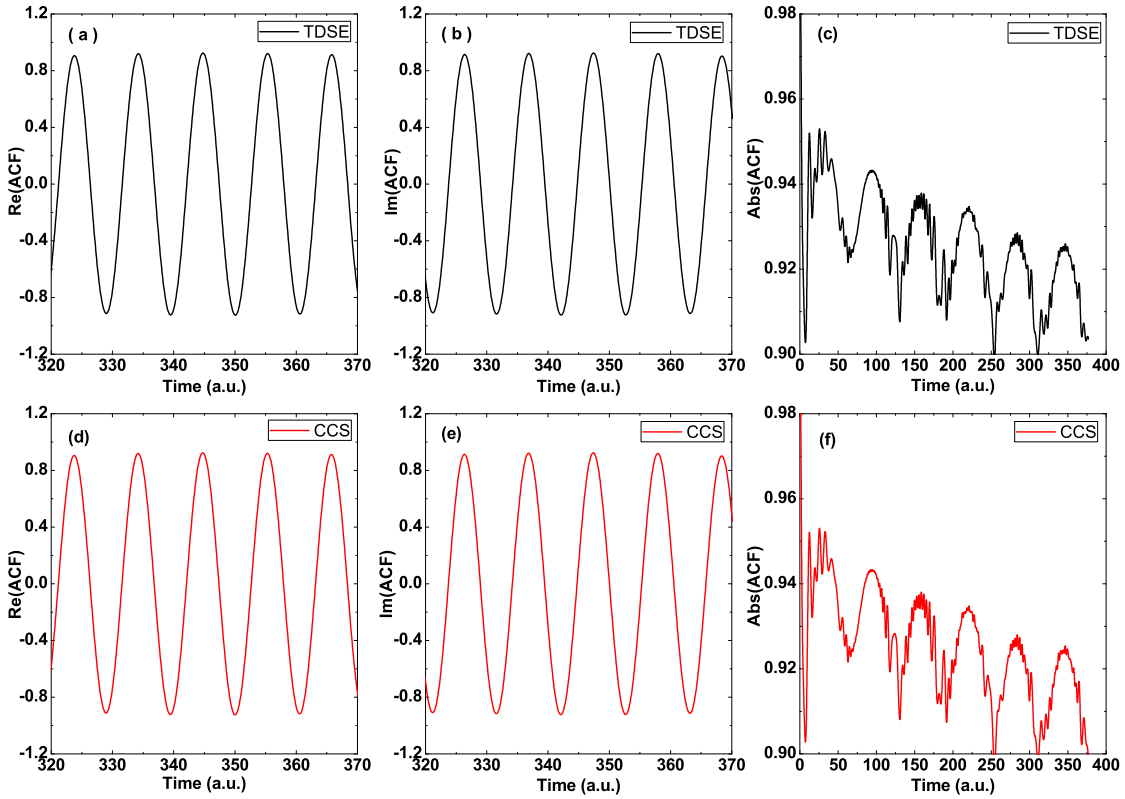

Figure 7.3: ACFs from the TDSE and the CCS approach with the same initial sampling, as that used in Fig. 7.1, but with reprojection of wave function during the whole time propagation applied at each atomic unit. The 1D Gaussian potential $V_g(x) = -\exp(-\lambda x^2)$, where $\lambda = 0.5$, with initial wave packet (7.4) starts from the origin $(q_c, p_c) = (0, 0)$ with $\gamma = 1.0$, and the external laser field $E(t) = E_0 \cos(\omega_0 t)$ with strength $E_0 = 0.1$ and frequency $\omega_0 = 0.05$ are considered. The black solid lines are the results from the TDSE, the red solid lines are the results from the CCS approach. From left to right the real, imaginary and absolute values of the ACFs are displayed.

regular amplitudes and oscillations are presented in the new results. Good quantitative agreement for longer time propagations between the CCS approach and the TDSE is present until the end of the external laser field. The consistence between the two methods can also be seen directly from the new time-dependent

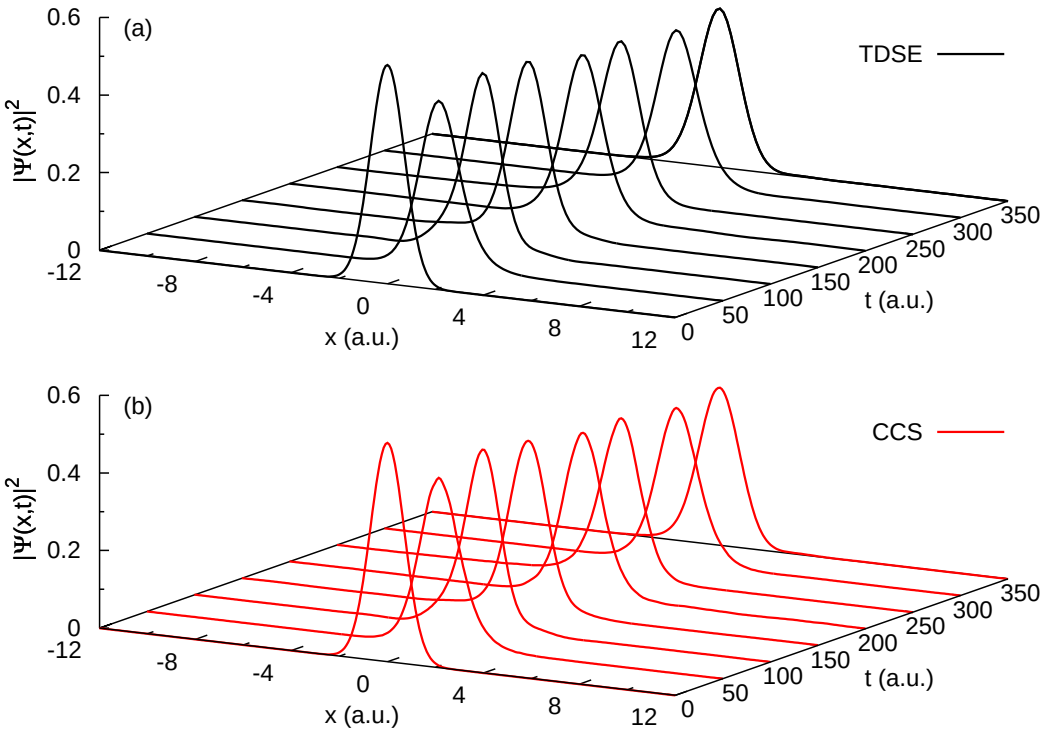

Figure 7.4: Time-dependent wave function from the TDSE and the CCS methods corresponding to Fig. 7.3. The black solid lines are the $|\Psi(x,t)|^2$ from the TDSE at different times; the red solid lines are the corresponding results from the CCS method with reprojection of the wave function.

wave function at every 50 atomic units, until the switch off of the laser field, as shown in Fig 7.4.

7.4 Dipole acceleration in the CSR

An interesting "observable" that can be used to extract the wave function information is the HHG spectrum, which is obtained through the Fourier transform of the dipole

$$S(\omega) \sim \int \mathscr{D}(t) \exp(-i\omega t) \mathrm{d}t, \tag{7.8}$$

where $\mathscr{D}(t)$ denotes the expectation value of the dipole operator $\hat{\mathscr{D}}$, and can be calculated through

$$\mathscr{D}(t) = \langle \Psi(t) | \hat{\mathscr{D}} | \Psi(t) \rangle. \tag{7.9}$$

Inserting the discrete CSR wave function Eq. (5.93) into (7.9), the expectation of dipole can be rewritten as

$$\begin{aligned} \langle \Psi(t) | \hat{\mathscr{D}} | \Psi(t) \rangle &= \sum_{i=1,j=1}^{n} D_i^* \exp\left(-\frac{i}{\hbar} S_i\right) \langle Z_i | \hat{\mathscr{D}} | Z_j \rangle D_j \exp\left(\frac{i}{\hbar} S_j\right) \\ &= \sum_{i=1,j=1}^{n} D_i^* \exp\left(-\frac{i}{\hbar} S_i\right) \langle Z_i | Z_j \rangle \mathscr{D}_{ij} D_j \exp\left(\frac{i}{\hbar} S_j\right) \\ &= \sum_{i=1,j=1}^{n} D_i^* \exp\left(-\frac{i}{\hbar} S_i\right) (\Omega_{ij} \cdot \mathscr{D}_{ij}) D_j \exp\left(\frac{i}{\hbar} S_j\right). \end{aligned} \tag{7.10}$$

In matrix form, this is written as

$$\mathscr{D}(t) = \mathbf{D}^{*\top} E^* (\Omega \cdot \mathscr{D}) \mathbf{E} \mathbf{D}, \tag{7.11}$$

where $\mathbf{D}$ is a column vector with elements D_i (coefficient of the CS), and $\mathbf{D}^{*\top}$ is the corresponding conjugate transpose matrix, $\mathscr{D}$ is a $n \times n$ matrix of dipole in the CSR (where, n is the size of the CSs), and the definition of other symbols are the same as previous.

The dipole operator, whose expectation value is employed to compute the harmonic spectra, may be expressed in the length, velocity and acceleration forms [56, 57]. In the length form, the dipole moment is very large in regions far away from the core; hence, the dynamics of such regions is over-emphasised. In the velocity form, there is no preferential spatial region. In the acceleration form, the region close to the core is probed, this is the spatial region in which, according to the TSM, HHG occurs. These forms can be computed employing Heisenberg equations. In this section, we only consider the dipole acceleration $\mathscr{D}_{jk}^{(a)}$ along the laser field direction. The derivation of the dipole acceleration related to different kinds of potentials will be shown in detail in the Appendix.

If the re-normalisation of the wave function is considered, the normalised dipole moment in Eq. (7.11) can be replaced by $\mathscr{D}(t)/N(t)$. Where, $N(t)$ is the norm

of the wave function, which in the CSR, can be calculated through

$$\begin{aligned} N(t) &= \langle \Psi(t) | \Psi(t) \rangle \\ &= \sum_{i=1,j=1}^{n} D_i^* \exp\left(-\frac{i}{\hbar} S_i\right) \langle Z_i | Z_j \rangle D_j \exp\left(\frac{i}{\hbar} S_j\right) \\ &= \sum_{i=1,j=1}^{n} D_i^* \exp\left(-\frac{i}{\hbar} S_i\right) \Omega_{ij} D_j \exp\left(\frac{i}{\hbar} S_j\right). \end{aligned} \tag{7.12}$$

The corresponding matrix form is

$$N(t) = \mathbf{D}^{*\top} E^* \Omega \mathbf{E} \mathbf{D}. \tag{7.13}$$

7.5 HHG spectrum

7.5.1 HHG spectrum from 1D Gaussian potential

In this section we focus on the study of HHG spectra, starting with the simple 1D Gaussian potential. In order to have an intuitive comparison, results obtained from the TDSE are adopted as benchmark.

According to the Ehrenfest theorem the dipole acceleration matrix element of the 1D Gaussian potential in the CSR is

$$\begin{aligned} -\langle z_i | \nabla V_G(x) | z_j \rangle &= \langle z_i | - 2\lambda x e^{-\lambda x^2} | z_j \rangle \\ &= -2\lambda \left(\frac{\gamma}{\pi}\right)^{1/2} \int \langle z_i | x \rangle \langle x | x e^{-\lambda x^2} | z_j \rangle \mathrm{d}x \\ &= -2\lambda \left(\frac{\gamma}{\pi}\right) \int x e^{-\lambda x^2} e^{-\gamma (x-\rho)^2} \mathrm{d}x \langle z_i | z_j \rangle \\ &= -2\lambda \left(\frac{\gamma}{\pi}\right) \int x e^{-(\gamma+\lambda)\left(x - \frac{\gamma}{\gamma+\lambda}\rho\right)^2} \mathrm{d}x \langle z_i | z_j \rangle \\ &= -2\lambda \left(\frac{\gamma}{\gamma+\lambda}\right)^{3/2} \rho e^{-\frac{\lambda\gamma}{\lambda+\gamma}\rho^2} \langle z_i | z_j \rangle. \end{aligned} \tag{7.14}$$

This dipole acceleration can also be obtained through

$$\begin{aligned} -\langle z_i | \nabla V_G(x) | z_j \rangle &= -\nabla_\rho \langle z_i | V_G(x) | z_j \rangle \\ &= -2\lambda \left(\frac{\gamma}{\gamma+\lambda}\right)^{3/2} \rho e^{-\frac{\lambda\gamma}{\lambda+\gamma}\rho^2} \langle z_i | z_j \rangle, \end{aligned} \tag{7.15}$$

where $\rho = \frac{z_i^* + z_j}{\sqrt{2\gamma}}$. Through the calculation, shown in Fig. 7.5, of the dipole acceleration and the corresponding HHG spectra with clean plateau and cutoff (expected from the TSM located at $I_p + 3.17U_p$) one can see that a good quantitative agreement between the CCS approach and the TDSE results has been achieved. The acceleration roughly follows the field and exhibits a series of high-frequency oscillations. These oscillations, together with spatial localization, are responsible for the HHG plateau. Similar oscillations have also been identified and discussed in previous publications using the TDSE computations and the HK propagator [25–28] for an initial wave packet starting far from the core. They have been associated with the interference between different types of electron trajectories returning to the core. They have also been studied in a different context, namely the adiabatic approximation [47, 48] and Bohmian trajectories as described in the first part of this thesis [71, 72].

One legitimate question that arises here is whether the CCS method also holds for other laser fields and whether the pulse shape influences the propagation. In order to address this, we use the reprojecting CCS method to consider the same initial wave packet as that used in Figs. 7.1-7.5, but in a 2-cycle sine square laser field with form

$$E(t) = E_0 \sin^2\left(\frac{\omega_0 t}{2N}\right) \sin(\omega_0 t), \tag{7.16}$$

as has been applied in Ref. [68]. The outcome of our computation is shown in Fig. 7.6. In the upper panels we display the dipole acceleration and the corresponding HHG spectrum obtained from the TDSE, which are employed as benchmarks. In general, the dipole acceleration roughly follows the laser field and similar high-frequency oscillations to those found in Fig. 7.5 are observed. The HHG spectrum exhibits a clean plateau followed by a sharp cutoff at $I_p + 3.17U_p$. The remaining panels of the figure display the dipole acceleration from the CCS method [panel(c)], and the corresponding spectrum [panel (d)]. For the sine square pulse, the same results as described previously are observed, namely, a good quantitative agreement between the CCS method and the TDSE for both dipole acceleration and HHG spectrum.

One may now ask whether a quantitative agreement between the CCS method and the TDSE can be achieved for other kind of initial wave functions. For instance,

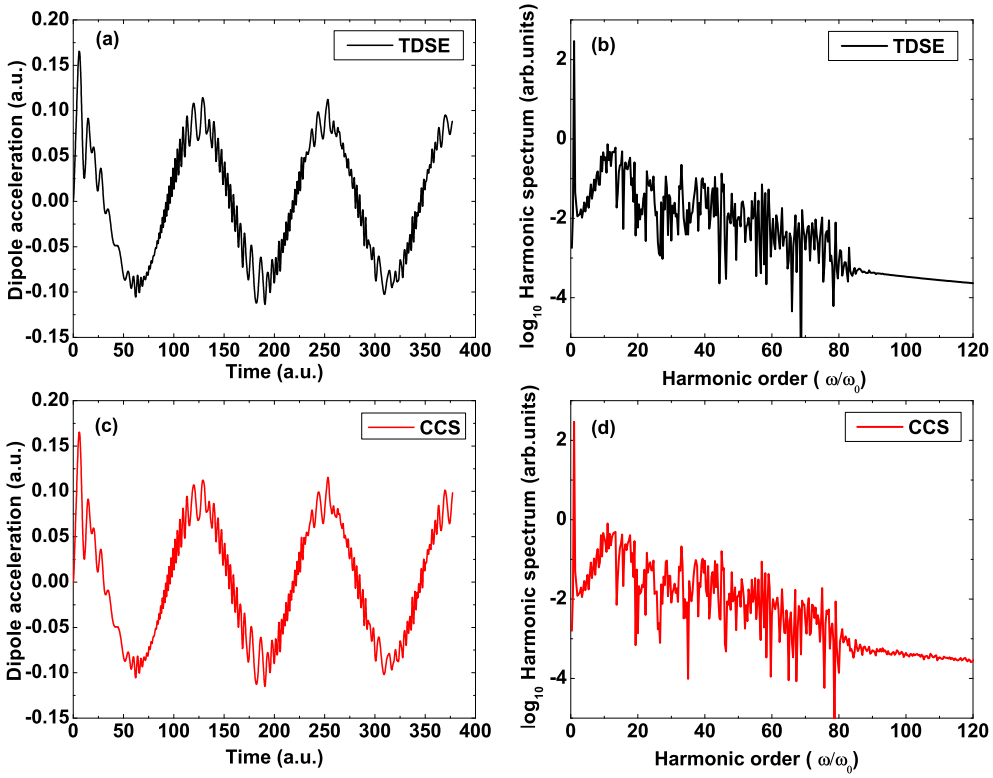

Figure 7.5: The dipole accelerations and corresponding HHG spectra computed from the 1D Gaussian potential $V_g(x) = -\exp(-\lambda x^2)$, with $\lambda = 0.5$, in an external laser field. (a): the dipole acceleration from the TDSE; (c): the dipole acceleration from the CCS method with reprojection of the wave function at each atomic unit; (b) and (d) are the corresponding HHG spectra of (a) and (c). The initial wave packet is (7.4) centred at $(q_c, p_c) = (0, 0)$, with $\gamma = 1.0$. The laser field is $E(t) = E_0 \cos(\omega_0 t)$, with strength $E_0 = 0.1$. and frequency $\omega_0 = 0.05$.

what happens when the initial wave packet is centred at some distance away from the bare atomic core? This initial wave packet has been applied in Refs. [25, 26] to study the dynamics of the recollision picture by eliminating the ionization process in the HHG process. In Fig. 7.7, we display the dipole acceleration [panel (c)] together with its HHG spectrum [panel (d)], by considering the initial wave packet (7.4) starting from the excursion distance [47] $x_{exc} = E_0/\omega_0^2$. From this figure we can see that a similar dipole acceleration structure as that shown

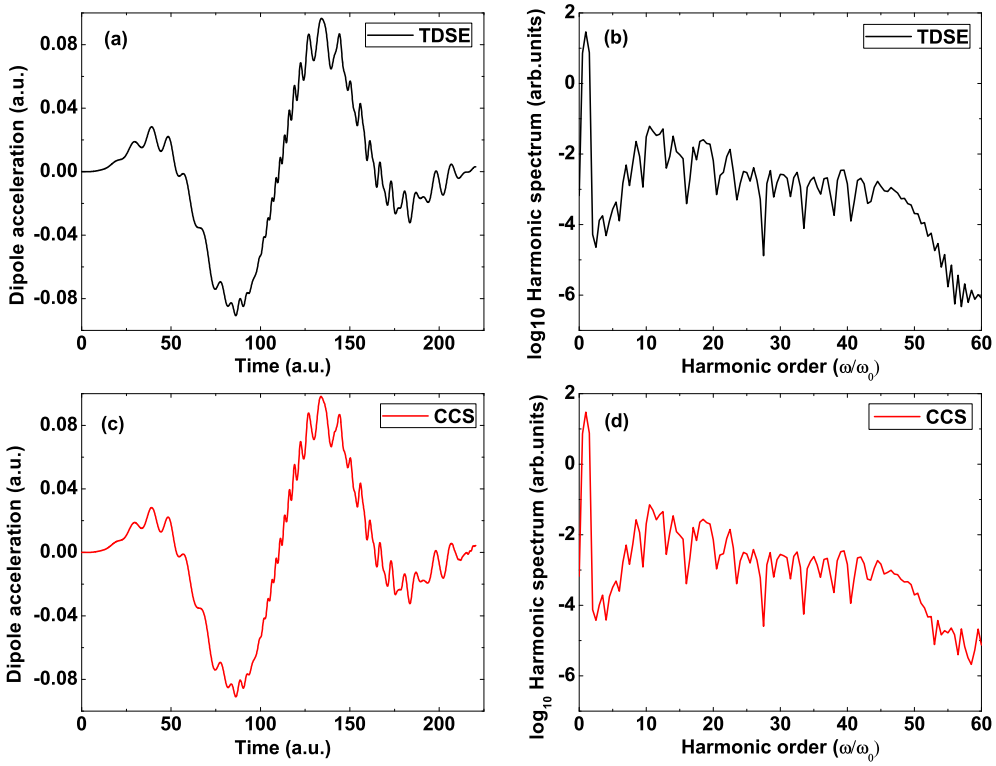

Figure 7.6: The dipole acceleration and HHG spectra from the sine square pulse Eq. (7.16), with the laser strength $E_0 = 0.1$, frequency $\omega_0 = 0.057$ and $N = 2$. The initial wave packet (7.4) starts from the origin $(q_c, p_c) = (0, 0)$, with $\gamma = 1.0$. The upper panels are the results from the TDSE, the lower panels are the corresponding results from the CCS method with reprojection.

in Ref. [25–28] is found in the CCS method. Furthermore, a good quantitative agreement is achieved between the HHG spectra obtained with the CCS approach and the TDSE, which is the HHG spectra exhibit a clean plateau and sharp cutoff located at $I_p + 2U_p = 105\omega_0$. Here, instead of a 3.5 cycle laser field considered in the Ref. [25–28], we use 2 cycle laser field. Since we can clearly see from Fig. 7.7 that the high frequency oscillations which contribute to the plateau and cutoff appear close to the end of one laser cycle ($2\pi/\omega_0 \simeq 116.2$), it is sufficient to use a two-cycle laser field to reproduce the main feature of HHG spectrum. However, if a shorter pulse is considered, for instance, only one cycle, it is not enough to

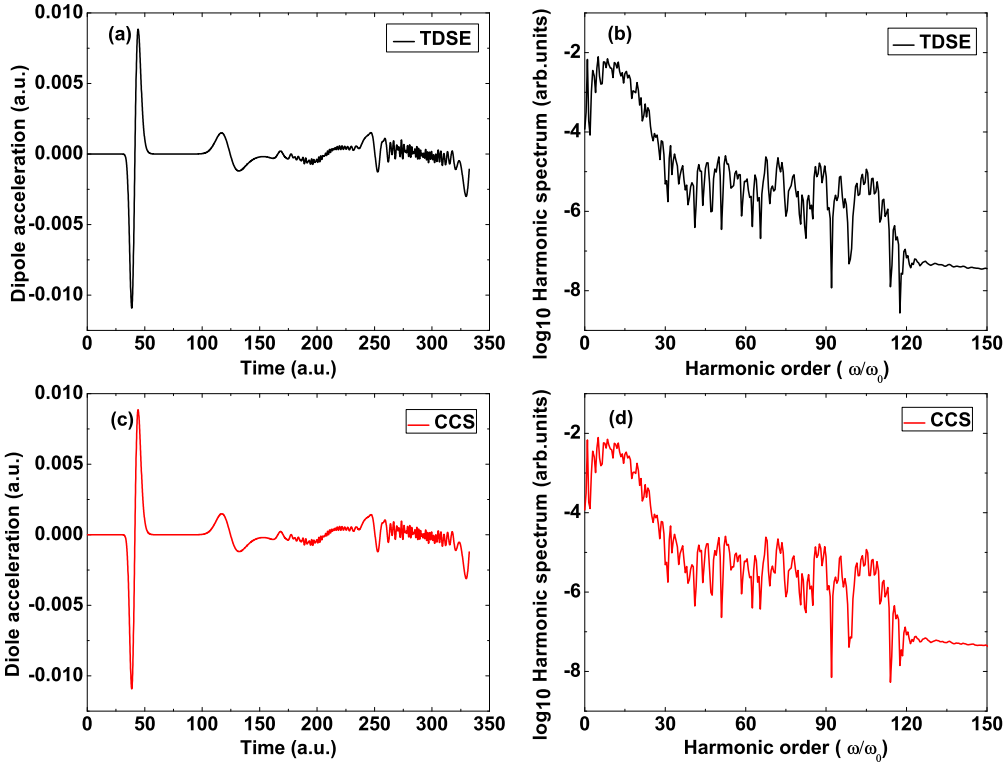

Figure 7.7: The dipole acceleration and corresponding HHG spectra. The initial wave packet (7.4) starts from the excursion amplitude ($x_{exc} = E_0/\omega_0^2$) with $\gamma = 0.05$, in the laser field $E(t) = E_0 \cos(\omega_0 t)$ with $E_0 = 0.1$ and frequency $\omega_0 = 0.0378$ [25–28]. Upper panels are results from the TDSE, lower panels are those from the CCS approach with reprojection. Note that, the initial sampling used here is the same as that shown in Fig. 7.1, but around $(q_c, p_c) = (x_{exc}, 0)$.

observe these high frequency oscillations and consequently the plateau and cutoff structure of the spectrum cannot be reproduced.

7.5.2 HHG spectrum from 3D Gaussian potential

In the previous subsection we have successfully applied an improved reprojection technique to the CCS method to study the HHG spectra for different kinds of laser pulses. We have established that the results from this method agree well

with those from the TDSE on the quantitative level. We now further investigate whether this reprojection method works on 3D systems through studying the HHG spectra.

Here, we would like to first extend our simulation to the 3D Gaussian potential $V_G(R) = -\exp(-\lambda R^2)$, with $R^2 = x^2 + y^2 + z^2$. The corresponding Hamiltonian of (6.11) in 3D form reads as

$$\hat{H} = \frac{\hat{P}^2}{2m} + V(\hat{R}) + \vec{R} \cdot \vec{E}(t), \tag{7.17}$$

where $\vec{E}(t)$ is the laser field along the z direction.

In the CSR, similar to the 1D formula Eq. (6.12), the kinetic energy is written in the form of

$$\langle Z_i | \frac{\hat{P}^2}{2m} | Z_j \rangle = -\frac{\hbar^2 \gamma}{4m} (Z_i^{*2} - 2Z_i^* \cdot Z_j - 3 + Z_j^2) \langle Z_i | Z_j \rangle, \tag{7.18}$$

where

$$\begin{aligned} Z_i^{*2} &= Z_{ix}^{*2} + Z_{iy}^{*2} + Z_{iz}^{*2} \\ Z_i^* \cdot Z_j &= Z_{ix}^* Z_{jx} + Z_{iy}^* Z_{jy} + Z_{iz}^* Z_{jz} \\ Z_j^2 &= Z_{jx}^2 + Z_{jy}^2 + Z_{jz}^2, \end{aligned} \tag{7.19}$$

Z_{ix}, Z_{iy} and Z_{iz} are the three elements of vector $Z_i = (Z_{ix}, Z_{iy}, Z_{iz})$. Note that, in Eq. (7.18) "3" comes from the 3 times' application of the 1D commutator Eq. (6.13). In fact, one can write $\hat{P}^2 = \hat{P}_x^2 + \hat{P}_y^2 + \hat{P}_z^2$ and then insert it into Eq. (7.18) to obtain

$$\begin{aligned} \langle Z_i | \frac{\hat{P}^2}{2m} | Z_j \rangle &= \langle Z_i | \frac{\hat{P}_x^2 + \hat{P}_y^2 + \hat{P}_z^2}{2m} | Z_j \rangle \\ &= \langle Z_i | \frac{\hat{P}_x^2}{2m} | Z_j \rangle + \langle Z_i | \frac{\hat{P}_y^2}{2m} | Z_j \rangle + \langle Z_i | \frac{\hat{P}_z^2}{2m} | Z_j \rangle \\ &= -\frac{\hbar^2 \gamma}{4m} (Z_i^{*2} - 2Z_i^* \cdot Z_j - 3 + Z_j^2) \langle Z_i | Z_j \rangle. \end{aligned} \tag{7.20}$$

The 3D Gaussian potential and the laser field in the CSR reads

$$\begin{aligned} \langle Z_i | V_G(R) | Z_j \rangle &= -\int e^{-\lambda R^2} \langle Z_i | \vec{R} \rangle \langle \vec{R} | Z_j \rangle \mathrm{d}^3 \vec{R} \\ &= -\left(\frac{\gamma}{\lambda + \gamma} \right)^{3/2} e^{-\frac{\lambda \gamma}{\lambda + \gamma} \rho^2} \langle Z_i | Z_j \rangle, \end{aligned} \tag{7.21}$$

and

$$\langle Z_i|\vec{R}\cdot\vec{E}(t)|Z_j\rangle = \rho_z E(t) = \vec{\rho}\cdot\vec{E}(t), \tag{7.22}$$

where $\rho = \sqrt{\vec{\rho}\cdot\vec{\rho}}$, $\vec{\rho} = \frac{Z_i^* + Z_j}{\sqrt{2\gamma}}$, and ρ_z is the element of vector $\vec{\rho}$ along $\vec{e}_z$.

From the above statement one can get

$$H_{ord}(Z_i^*, Z_j) = -\frac{\hbar^2\gamma}{4m}(Z_i^{*2} - 2Z_i^*\cdot Z_j - 3 + Z_j^2) - \left(\frac{\gamma}{\lambda+\gamma}\right)^{3/2} e^{-\frac{\lambda\gamma}{\lambda+\gamma}\rho^2} + \vec{\rho}\cdot\vec{E}(t). \tag{7.23}$$

Hence, the corresponding time-dependent elements of Z_i from the 3D Gaussian potential can be obtained through

$$\begin{aligned}\frac{\mathrm{d}Z_{i\chi}}{\mathrm{d}t} &= -\frac{i}{\hbar}\frac{\partial H_{ord}(Z_i^*, Z_i)}{\partial Z_{i\chi}^*} \\ &= -\frac{i}{\hbar}\left[-\frac{\hbar^2\gamma}{2m}Z_{i\chi}^* + \frac{\hbar^2\gamma}{2m}Z_{i\chi} + \frac{\sqrt{2}\lambda\rho_{i\chi}}{\sqrt{\gamma}}\left(\frac{\gamma}{\lambda+\gamma}\right)^{5/2} e^{-\frac{\lambda\gamma}{\lambda+\gamma}\rho^2} + \frac{\vec{E}(t)\cdot\vec{e}_\chi}{\sqrt{2\gamma}}\right].\end{aligned} \tag{7.24}$$

Here, $\vec{e}_\chi$ is the unit direction of the coordinate and $\chi = x, y, z$.

Fig. 7.8 shows the dipole acceleration, which in the CSR reads

$$\mathscr{D}_{i,j}^{(a)} = -2\lambda\left(\frac{\gamma}{\gamma+\lambda}\right)^{5/2}\rho_z e^{-\frac{\gamma\rho^2}{\gamma+\lambda}}\langle Z_i|Z_j\rangle, \tag{7.25}$$

and its related HHG spectrum from the 3D Gaussian potential as described above. For simplicity, a 3D Gaussian wave packet similar to Eq. (7.4) is applied as the initial wave function, written as

$$\Psi(x, y, z, 0) = \left(\frac{\gamma}{\pi}\right)^{3/4}\exp\left\{-\frac{\gamma}{2}\left[(x-q_{xc})^2 + (y-q_{yc})^2 + (z-q_{zc})^2\right]\right\}, \tag{7.26}$$

where $(q_{xc}, q_{yc}, q_{zc}) = (0, 0, 0)$ is selected. In fact, this wave function is a simple multiple of three 1D Gaussian wave packets defined by Eq. (7.4). The initial sampling for this case is chosen as follows: 1) q_x, q_y and p_x, p_y are randomly selected using a normal distribution (stated in Section 5.7); 2) for q_z and p_z, the same values as those stated in Section 7.1 are selected. This is because the laser

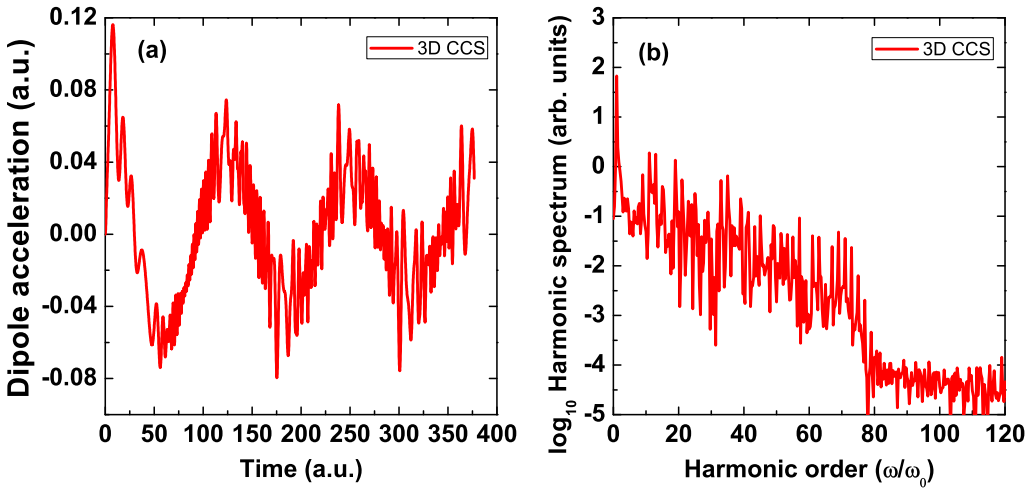

Figure 7.8: Panel (a) is the dipole acceleration computed from the 3D Gaussian potential $V_G(R) = -\exp(-\lambda R^2)$, with $\lambda = 0.5$, in the laser field $E(t) = E_0 \cos(\omega_0 t)$, with strength $E_0 = 0.1$ and frequency $\omega_0 = 0.05$; panel (b) is the corresponding HHG spectrum from (a).

field is along the $\hat{e}_z$ direction and this direction plays the main role during the time propagation. From our results we can clearly see that a dipole acceleration, roughly following the laser field, is present. The corresponding HHG spectrum shows a clean plateau and cutoff located at $I_p + 3.17U_p$, which is the same as that found in the previous 1D simulations.

7.5.3 HHG spectrum from 3D Coulomb potential

In this subsection we show the application of the improved CCS method on the most realistic 3D potential, namely, the 3D Coulomb potential. As mentioned in the previous chapter, the CCS method has some limitations in terms of obtaining the analytical form of the 1D and 2D Coulomb and soft-core potentials, and our main purpose of this thesis is trying to pave a way for the numerical simulation of systems with multiple degrees of freedom. Here we only considering the 3D Coulomb potential expressed as

$$V_C(R) = -\frac{1}{R}. \tag{7.27}$$

We will apply two kinds of initial wave functions for the 3D Hydrogen in this subsection, namely, a wave function starting from the origin and a wave function starting from the excursion distance. Three approaches can be adopted to obtain the initial wave function starting from the origin.

1) From Chapter 5 we see that the initial wave function in the CSR is $\Phi_i(0) = C_i(0)$, as soon as the initial $z_i(0)$ are obtained, this can be derived using the variational principle. Specifically, starting from

$$\frac{\langle\Psi(0)|\hat{H}|\Psi(0)\rangle}{\langle\Psi(0)|\Psi(0)\rangle} = E, \tag{7.28}$$

inserting the identity operator (5.83), we can get

$$\frac{\sum_{ij}^{n}\sum_{kl}^{n}\langle\Psi(0)|Z_i\rangle\left(\Omega^{-1}\right)_{ij}\langle Z_j|\hat{H}|Z_k\rangle\left(\Omega^{-1}\right)_{kl}\langle Z_l|\Psi(0)\rangle}{\sum_{ij}^{n}\langle\Psi(0)|Z_i\rangle\left(\Omega^{-1}\right)_{ij}\langle Z_j|\Psi(0)\rangle} = E \tag{7.29}$$

Writing the above equation in the matrix form and rearranging it, we obtain

$$\Omega^{-1}\left(\Omega\cdot\mathbf{H}\right)\Omega^{-1}\mathbf{C} = \mathbf{E}\Omega^{-1}\mathbf{C}, \tag{7.30}$$

where $\left(\Omega\cdot\mathbf{H}\right)_{ij} = \Omega_{ij}H_{ord}\left(Z_i^*, Z_j\right)$. By solving Eq. (7.30) one can get n eigenvalues (energies) and corresponding eigenvectors for the given basis $Z_i(0)$. By choosing the lowest eigenvalue and corresponding eigenvector, we obtain the initial $C_i(0)$. Note that, if the ground state of Hydrogen is considered, this lowest eigenvalue should close to the ground state energy of Hydrogen. Otherwise, the initial $Z_i(0)$ should be reselected.

2) The second way to compute the initial $C_i(0)$ for the 3D Hydrogen is through numerical calculation of the 3D Eq. (5.53), with the ground state wave function of hydrogen

$$\Psi(R,0) = \frac{1}{\sqrt{\pi}}e^{-R}. \tag{7.31}$$

In the above equation, atomic units are used.

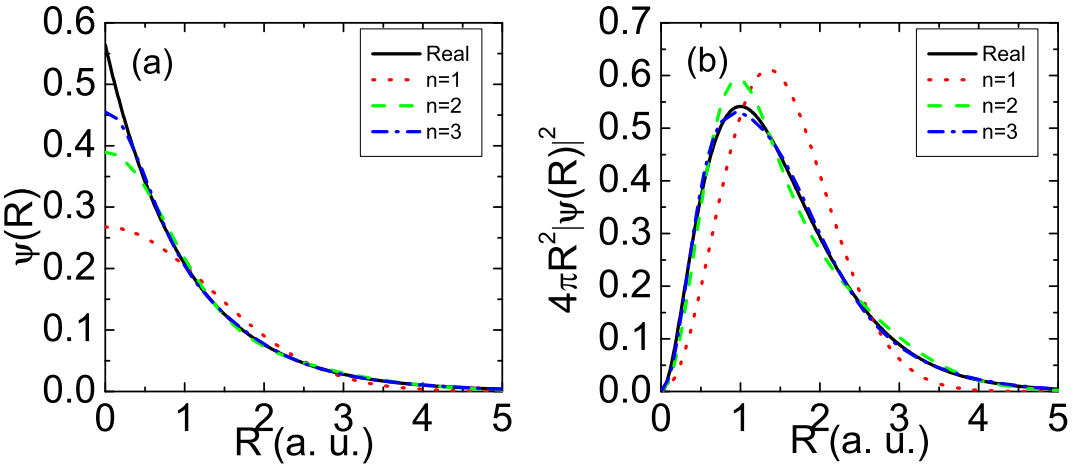

Figure 7.9: Panel (a): the ground state wave function of Hydrogen approximated by the Gaussian wave packet $\Psi(R)$. Panel (b): the corresponding radial distribution functions ($4\pi R^2|\Psi(R)|^2$) of panel (a). The black solid line is the exact wave function; the red dot line is the wave function approximated by one Gaussian, with $\alpha_1 = 1.0$, $\beta_1 = 0.270950$; the green dot line is the wave function approximated by two Gaussians, with $\alpha_1 = 0.678914$, $\beta_1 = 0.151623$, $\alpha_2 = 0.430129$, $\beta_2 = 0.851819$; and the blue dash dot line is the wave function approximated by 3 Gaussians, with $\alpha_1 = 0.444635$, $\beta_1 = 0.109818$, $\alpha_2 = 0.535328$, $\beta_2 = 0.405771$, $\alpha_3 = 0.154329$, $\beta_3 = 2.22766$. (The parameters used in this figure are cited from Ref. [224].)

3) Theoretically, there is no problem to carry out the numerical computation through method 2. However, further simplifications are explored, this is because a CS in the coordinate space is a Gaussian wave packet, the analytic form of $C_i(0)$ can be obtained by approximating the initial wave function as some Gaussian wave packets, we show this as follows.

The wave function (7.31) can be approximated as [224]

$$\Psi(R,0) = \sum_{k=1}^{n} \alpha_k \left(\frac{2\beta_k}{\pi}\right)^{3/4} \exp(-\beta_k R^2). \tag{7.32}$$

In Fig. 7.9, we show the wave function of three cases ($n = 1, 2, 3$) as well as the

exact wave function given by (7.31).
Because

$$\langle \vec{R}|Z_i\rangle = \left(\frac{\gamma}{\pi}\right)^{3/4} \exp\left(-\frac{P_i^2}{2\hbar^2\gamma} + \frac{i}{2\hbar}\vec{P}_i\cdot\vec{Q}_i\right) \exp\left[-\frac{\gamma}{2}\left(\vec{R} - \sqrt{\frac{2}{\gamma}}Z_i\right)^2\right], \quad (7.33)$$

one can get $\langle\Psi(0)|Z_i\rangle$ as

$$\begin{aligned}
\langle\Psi(0)|Z_i\rangle &= \int \langle\Psi(0)|\vec{R}\rangle\langle\vec{R}|Z_i\rangle \mathrm{d}^3\vec{R} \\
&= \int \sum_k \alpha_k \left(\frac{2\beta_k}{\pi}\right)^{3/4} \exp(-\beta_k R^2) \left(\frac{\gamma}{\pi}\right)^{3/4} \exp\left(-\frac{P_i^2}{2\hbar^2\gamma} + \frac{i}{2\hbar}\vec{P}_i\cdot\vec{Q}_i\right) \\
&\quad \times \exp\left[-\frac{\gamma}{2}\left(\vec{R} - \sqrt{\frac{2}{\gamma}}Z_i\right)^2\right] \mathrm{d}^3\vec{R} \\
&= \sum_k \alpha_k \left[\frac{2\beta_k\gamma}{\left(\frac{\gamma}{2}+\beta_k\right)^2}\right]^{3/4} \exp\left(-\frac{P_i^2}{2\hbar^2\gamma} + \frac{i}{2\hbar}\vec{P}_i\cdot\vec{Q}_i\right) \exp\left(-\frac{\beta_k}{\frac{\gamma}{2}+\beta_k}Z_i^2\right).
\end{aligned} \quad (7.34)$$

Therefore, for the given basis $Z_i(0)$, the initial coefficient $C_i(0)$ is

$$\begin{aligned}
C_i(0) = \Phi_i(0) &= \langle Z_i|\Psi(0)\rangle = \langle\Psi(0)|Z_i\rangle^* \\
&= \sum_k \alpha_k \left[\frac{2\beta_k\gamma}{\left(\frac{\gamma}{2}+\beta_k\right)^2}\right]^{3/4} \exp\left(-\frac{P_i^2}{2\hbar^2\gamma} - \frac{i}{2\hbar}\vec{P}_i\cdot\vec{Q}_i\right) \exp\left(-\frac{\beta_k}{\frac{\gamma}{2}+\beta_k}Z_i^2\right).
\end{aligned} \quad (7.35)$$

Thus for testing purposes, using a Gaussian wave packet to replace the real ground state wave function of Hydrogen is reasonable. In this subsection the Gaussian wave packet Eq. (7.26) is applied as the initial wave function. In fact, through our simulations (but not shown here) if the above stated Gaussian approximation wave function (7.32) with $n = 3$ is selected as the initial wave function, results very similar to our following outcomes can be obtained.

The explicit Hamiltonian of (7.17), for the 3D Coulomb potential, in the CSR is (see Appendix for details)

$$H_{ord}(Z_i^*, Z_j) = -\frac{\hbar^2\gamma}{4m}(Z_i^{*2} - 2Z_i^*\cdot Z_j - 3 + Z_j^2) - \frac{1}{\rho}\mathrm{erf}(\sqrt{\gamma}\rho) + \vec{\rho}\cdot\vec{E}(t), \quad (7.36)$$

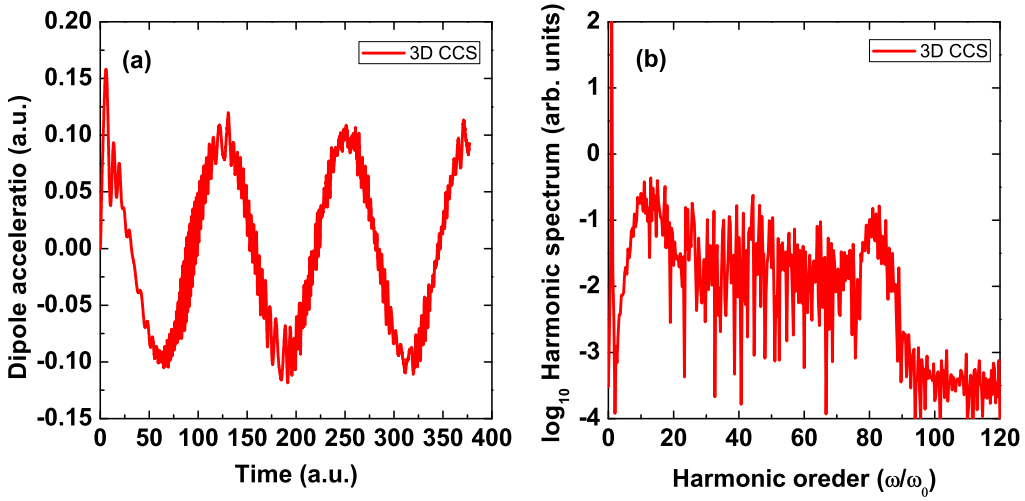

Figure 7.10: Results computed from the CCS method with the reprojection of the wave function to the initial grids. Panel (a) is the dipole acceleration computed from the 3D Coulomb potential $V_C(R) = -1/R$, in the laser field $E(t) = E_0 \cos(\omega_0 t)$, with strength $E_0 = 0.1$ and frequency $\omega_0 = 0.05$. Panel (b) shows the corresponding HHG spectrum of (a), with the initial wave function (7.26) centered at $(q_{xc}, q_{yc}, q_{zc}) = (0, 0, 0)$ with $\gamma = 1.0$. The cutoff locates at about $I_p + 3.17U_p$.

and the time-dependent derivative of $Z_{i\chi}$ corresponding to Eq. (7.36) is

$$\begin{aligned}\frac{\mathrm{d}Z_{i\chi}}{\mathrm{d}t} &= -\frac{i}{\hbar}\frac{\partial H_{ord}(Z_i^*, Z_i)}{\partial Z_{i\chi}^*} \\ &= -\frac{i}{\hbar}\left[-\frac{\hbar^2\gamma}{2m}Z_{i\chi}^* + \frac{\hbar^2\gamma}{2m}Z_{i\chi} + \frac{\rho_{i\chi}}{\rho^3\sqrt{2\gamma}}\mathrm{erf}(\sqrt{\gamma}\rho) - \frac{\rho_{i\chi}\sqrt{2}}{\rho^2\sqrt{\pi}}e^{-\gamma\rho^2} + \frac{\vec{E}(t)\cdot\vec{e}_\chi}{\sqrt{2\gamma}}\right].\end{aligned} \tag{7.37}$$

Fig. 7.10 shows the dipole acceleration of the Coulomb potential along the laser field direction, expressed as (see Appendix for details)

$$\mathscr{D}_{i,j}^{(a)} = -\frac{\rho_z}{\rho^3}\mathrm{erf}(\rho\sqrt{\gamma}) + 2\sqrt{\frac{\gamma}{\pi}}\frac{\rho_z}{\rho^2}e^{-\gamma\rho^2} \tag{7.38}$$

in the CSR, and the corresponding HHG spectrum in the external laser field. As shown in this figure, a dipole acceleration similar to that observed in the 1D

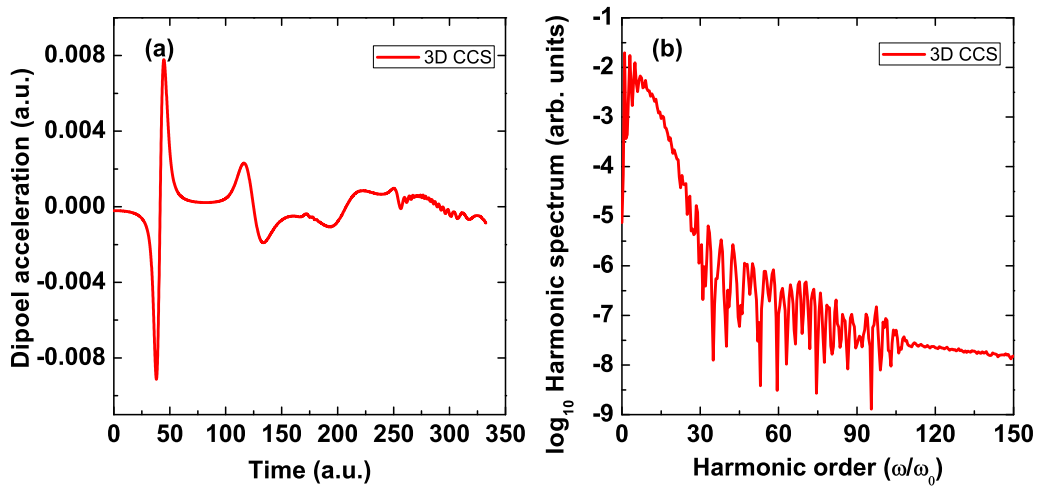

Figure 7.11: Dipole acceleration in panel (a) is computed from the 3D Coulomb potential $V_C(R) = -1/R$, in the laser field $E(t) = E_0 \cos(\omega_0 t)$, with strength $E_0 = 0.1$ and frequency $\omega_0 = 0.0378$; panel (b) shows the corresponding HHG spectrum of (a). In this figure $\Psi(x, y, z, 0) = \left(\frac{\gamma}{\pi}\right)^{3/4} \exp\left\{-\frac{\gamma}{2}\left[x^2 + y^2 + (z - x_{exc})^2\right]\right\}$, which starts from the excursion amplitude $x_{exc} = E_0/\omega_0^2$ and with $\gamma = 0.05$, is used as the initial wave function. The cutoff locates at about $I_p + 2U_p$.

Gaussian potential is obtained. A clean HHG spectrum with the cutoff position located at about $I_p + 3.17U_p$ can also be obtained. If we let the initial wave function start from the excursion amplitude, i.e., select (q_{xc}, q_{yc}, q_{zc}) in Eq. (7.26) to be $(0, 0, E_0/\omega_0^2)$, results very similar to those found in Fig. 7.7 and Ref. [25–28] can also be obtained through the CCS computation (as shown in Fig. 7.11).

7.6 Conclusions

In this chapter we have applied the CCS method to study the ACFs and HHG spectra. Instead of random initial sampling, a set of equal spacing grids in the main direction, namely along the laser field direction, are used for the simulations. Through the studies of the ACF and the time-dependent wave function of the 1D Gaussian potential in the coordinate space, our outcomes show that, similar to other Gaussian wave packet techniques that are accurate for short time

propagation, the original CCS works very well for short time propagation. However, during long time propagation the results degrade, which might be due to the fact that the CCS method depends strongly on the coherence nature of the states.

In order to overcome the problem above, a periodic reprojection technique of the wave function onto the initial grids [207, 208] is applied, and subsequently a good quantitative agreement with the results from the TDSE can be achieved. The first ever computation of the HHG spectra with clean plateau and expected sharp cutoff are obtained through this improved CCS method, and is confirmed through comparison to the TDSE computations on different kinds of laser fields and initial wave packets for the 1D Gaussian potential.

Going beyond the 1D system, the reprojected CCS method is applied to the studies of both the 3D Gaussian and Coulomb potentials in strong laser fields. Using equal spacing grids along the laser field direction, and random selected grids in the other directions, we find that very good results in both the dipole acceleration and HHG spectra can also be obtained in both 3D Gaussian and Coulomb potentials.

Finally, we would like to point out that the CCS method can be easily applied to multidimensional systems, without dramatically increasing the cost of the computation. However, because the HHG phenomenon is a coherent process, in which quantum interference is ever-present, it is very difficult to achieve converged results with regard to the initial sampling. Further attentions might be paid to solve certain technical hurdles, just as the reprojection technique applied here in this thesis.

Chapter 8

Summary and conclusion

Two orbit-based novel approaches in the strong field and attosecond physics, namely, the Bohmian trajectories and the IVR methods, are mainly employed to study single electron dynamics in external laser fields in this thesis. Both of them describe the system dynamics in terms of trajectories, and include the binding potential and the laser field.

In the first part of this thesis, Bohmian trajectories are employed to the study of HHG. Specifically, in Chapter 3, several driving-field intensities, pulse shapes and binding potentials are considered to cover general scenarios of applications. Our results show that the part of the wave function located in the immediate vicinity of $x = 0$ provides the HHG spectrum. The innermost Bohmian trajectory starting at $x(0) = 0$ most closely replicates the harmonic spectra on a qualitative level. This is a stronger statement of observation than that provided by the dipole acceleration: by using the dipole acceleration, one may conclude that the overlap between the continuum and the bound part of the wave function near the core region is important. Using the time-frequency analysis, we associate this central Bohmian trajectory to an ensemble of unbound classical trajectories leaving and returning to the core, in agreement with the TSM. The phase information can be transmitted non-locally to the central Bohmian trajectory by changing the flow far from the core, examples are provided using truncated potentials. Moreover our studies illustrate why the SFA works so well: the SFA reduces the influence of the core to a single point and approximates the continuum by Volkov waves, because the most relevant part of the wave function for the HHG is localised.

We also relate the Bohmian trajectories to the short and long trajectories encountered in the SFA and show that the time-frequency maps from the central Bohmian trajectory overestimate the contribution of the long SFA trajectory, in comparison to the TDSE, which is in agreement with what has been observed in the literature [128, 135, 136].

In Chapter 4, we have applied the Bohmian mechanics to assess the influence of specific regions in the configuration space on HHG. By considering an ensemble of Bohmian trajectories we show that a spatially extended core is paramount for obtaining good agreement with the TDSE, this holds not only for the low plateau and below-threshold harmonics, but also for the cutoff region. This implies that a wide initial wave packet spread in position space is necessary for an accurate description of the problem. In the Bohmian trajectory view, this spread manifests itself as an uncertainty in the initial conditions [58]. This is consistent with recent studies in which the SFA has been improved to include this spread [134, 137]. The fully quantum mechanical version of the SFA, without resorting to the steepest-descent method, has shown very good agreement with the TDSE in the cutoff region. In the time-frequency maps, neglecting the initial position spread causes an over-enhancement in the signal related to the long SFA trajectory [135, 136]. We have identified a similar effect in our computations if only the central Bohmian trajectory is considered. By deliberately placing absorbing boundaries in the spatial regions within the ranges of excursion amplitudes of a classical electron, but outside the core region, we have degraded the phase of the whole wave function. This has influenced both the HHG spectrum and the time-frequency maps of the central Bohmian trajectory and the degradation has occurred as would be expected from the TSM. In fact, these changes are transmitted nonlocally, as the probability density flow associated with the central Bohmian trajectory never leaves the core region. Since Bohmian trajectories are in fact slices of the wave function, they will always depend on the behavior associated with the whole wave function, regardless of the positions occupied by the probability density in the configuration space. Hence, if the wave function is altered far from the core, all the slices will be different. Finally, by reconstructing the flow of the wave function from an ensemble of Bohmian trajectories, we have found that a Hanning filter modifies this flow and suppresses irreversible ioniza-

tion. For this reason, it reduces the background if the length form of the dipole operator is used.

Here, we would like to list the advantages and disadvantages of Bohmian trajectories. On one hand, Bohmian trajectories are directly extracted from the time-dependent wave function, they contain all phase information related to the full time-dependent Hamiltonian, both the driving field and the binding potential are accounted for. They may therefore be used to probe the time-dependent wave function in specific regions in the configuration space, and study how the time-dependent probability density flow behaves in specific spatial regions. On the other hand, one should keep in mind that a Bohmian trajectory functions much more like a slice of the wave function than a trajectory in the classical sense, it depicts a highly nonlocal entity. One cannot distinguish "bound" and "unbound" through the position of a Bohmian trajectory, it may be localised in the innermost part of the core and still contains bound and continuum dynamics, and vice versa. Therefore, if one is interested in information related to the phase of the wave function, and not the probability-density flow, one needs to employ additional resources such as time-frequency maps or quasiprobabilities in the phase space. Another advantage is that, theoretically, Bohmian trajectories may be used for reconstructing the probability flow in the real time. In practice, however, the main obstacle for the reconstruction is that the time-dependent wave function has to be solved first in order to obtain the trajectories, which has been almost computationally impossible for systems with multiple degrees of freedom. However, a real effort to overcome this obstacle and construct Bohmian trajectories without the need for the TDSE solution has been carried out recently [138].

In the second part of this thesis, we study the applications of the IVRs in strong fields. In Chapter 6, comparison between the quantum IVR (the CCS) method and a semiclassical IVR (HK propagator) method are presented. The trajectories in the HK method are purely classical, while in the CCS method the trajectory of a CS is driven by the ordered Hamiltonian, which is the average of the quantum Hamiltonian with regard to the CSs, and takes into account the local zero-point energy and further corrections due to commutators. This ordered Hamiltonian leads to the lowering of the barrier, which partially takes tunneling into account.

The CCS and HK trajectories are identical only in the case of a harmonic potential. Through the trajectory analysis we find that, the forbidden region defined in the classical mechanics cannot be crossed by the trajectories used to construct the HK propagator, while it can be crossed by the trajectories defined in the CCS method. Applying Wigner quasiprobability distributions, we find that if those classical trajectories starting outside the bound phase-space region are taken into consideration, the common feature of tails present in the Wigner distribution can be observed. Depending on the momenta associated with this tail, it may be related to over-the-barrier or tunneling ionization. Similar tails have been identified in the literature, using either a zero range potential [217, 219] or the TDSE [221]. On the other hand, if those classical trajectories starting outside of the bound phase-space region are removed, the tails in the Wigner function disappear. This implies that these trajectories are an essential and fully classical ingredient for reproducing the tails in the context of a semiclassical IVR. Furthermore, the absence of the tails in the Wigner function also support the assumption that the Wigner function is non-local. Moreover, through direct comparison of the Wigner quasiprobability distributions obtained from the TDSE, the HK propagator and the CCS method, we find that good agreement with the full solution from the TDSE can be obtained through both IVRs. Our results, once again, indicate that the HK propagator does not fully account for tunneling and over-the-barrier reflections, however, the CCS method represents a fully quantum IVR and accurately reproduces the results of a standard TDSE solver.

In Chapter 7, in order to test the convergence of the CCS method for long time propagations, the ACF of 1D Gaussian potential in an external laser field is first studied. Our results show that, as a quantum orbit-based IVR method, the original CCS method works well for short time propagations. However, because successful application of the CCS method strongly depends on the coherence feature of the states, for long time propagation the CCS method does not work well. In order to solve this problem, a periodic reprojection of the wave function to the initial grids is applied. With the reprojection at each atomic unit, our results show that the ACF, the time-dependent wave function as well as the dipole acceleration and the HHG spectra obtained from the CCS method can give good quantitative agreement with those from the standard TDSE. In order to test the

stability of this improved CCS method, we have considered simple 1D short-range Gaussian potential exposed to different kinds of external fields. All of our simulations show a common conclusion, namely that the HHG spectra show a clear plateau and cutoff structure located at the expected position predicted by the TSM. If the initial wave packet starts from the origin, the HHG spectra show a clear plateau and the cutoff locates at $I_p + 3.17U_p$. By modeling the initial wave packet starting from the excursion amplitude, the high frequency oscillations in the dipole acceleration found in other Refs. [25–28] can also be seen under the CCS method, and the spectrum show a cutoff located at about $I_p + 2U_p$ being observed. Furthermore, we have gone beyond the 1D model potential and applied the CCS method to the study of HHG from 3D potentials, and very good results are obtained from both 3D Gaussian and 3D Coulomb potentials.

One should note that, in principle, the CCS approach has several advantages: 1) it can be easily extended to more degrees of freedom such as multi-electron atoms and molecules without dramatically increase the computing cost; 2) the initial state can be chosen randomly; 3) in the coupled equations some cancelations will appear which can simplify the quantum mechanical coupling terms; 4) the motion of electrons can be guided by classical mechanics; and 5) it accounts for quantum mechanical effects such as tunneling and quantum interference. However, in practice, to complete the numerical simulations some technical challenges need to be overcome, such as the selection of initial sampling and the reprojection technique employed in this thesis. Furthermore, the CCS method can effectively tackle the singularity of 3D Coulomb potential, however some obstacles have to be overcome in order to apply it to Coulomb potentials with lower degrees of freedom (less than 3) and the soft-core potential. This does not mean that the CCS approach is not applicable, but analytical forms of these potentials appears to be impossible to obtain in the CSR, as we point out in the appendix.

Appendix A

Appendix

A.1 The generalization of multi-dimensional CSs

The multi-dimensional CS $|Z\rangle$ is a product of each of 1D CSs. For example, a M dimensional CS is written as $|Z\rangle = |z_1\rangle|z_2\rangle|z_3\rangle\cdots|z_M\rangle$. The corresponding eigenvalue is

$$\begin{aligned} Z &= \sqrt{\frac{\gamma}{2}}\vec{Q} - \frac{i}{\hbar}\sqrt{\frac{1}{2\gamma}}\vec{P} \\ Z^* &= \sqrt{\frac{\gamma}{2}}\vec{Q} + \frac{i}{\hbar}\sqrt{\frac{1}{2\gamma}}\vec{P}, \end{aligned} \tag{A.1}$$

where $\vec{Q}$, $\vec{P}$, Z and Z^* are M dimensional vectors.

The overlap between two CSs is defined as

$$\langle Z_i|Z_j\rangle = \Omega_{ij} = \exp\left(Z_i^* \cdot Z_j - \frac{|Z_i|^2}{2} - \frac{|Z_j|^2}{2}\right). \tag{A.2}$$

The corresponding multi-dimensional expression of Eq. (5.49) is

$$\langle\vec{R}|Z_j\rangle = \left(\frac{\gamma}{\pi}\right)^{3/4}\exp\left[-\frac{\gamma}{2}(\vec{R}-\vec{Q}_j)^2 + \frac{i}{\hbar}\vec{P}_j\cdot(\vec{R}-\vec{Q}_j) + \frac{i}{2\hbar}\vec{P}_j\cdot\vec{Q}_j\right] \tag{A.3}$$

and

$$\langle Z_i|\vec{R}\rangle = \left(\frac{\gamma}{\pi}\right)^{3/4}\exp\left[-\frac{\gamma}{2}(\vec{R}-\vec{Q}_i)^2 - \frac{i}{\hbar}\vec{P}_i\cdot(\vec{R}-\vec{Q}_i) - \frac{i}{2\hbar}\vec{P}_i\cdot\vec{Q}_i\right]. \tag{A.4}$$

Therefore,

$$\begin{aligned}
\langle Z_i|\vec{R}\rangle\langle\vec{R}|Z_j\rangle &= \left(\frac{\gamma}{\pi}\right)^{3/2}\exp\left\{\begin{array}{l} -\frac{\gamma}{2}\left[\left(\vec{R}-\vec{Q}_j\right)^2+\left(\vec{R}-\vec{Q}_i\right)^2\right] \\ +\frac{i}{\hbar}\vec{R}\cdot\left(\vec{P}_j-\vec{P}_i\right)-\frac{i}{2\hbar}\vec{P}_j\cdot\vec{Q}_j+\frac{i}{2\hbar}\vec{P}_i\cdot\vec{Q}_i \end{array}\right\} \\
&= \left(\frac{\gamma}{\pi}\right)^{3/2}\exp\left\{\begin{array}{l} -\frac{\gamma}{2}\left[2R^2+Q_j^2-2\vec{R}\cdot(\vec{Q}_i+\vec{Q}_j)+Q_i^2\right] \\ +i\vec{R}\cdot\left(\vec{P}_j-\vec{P}_i\right)-\frac{i}{2\hbar}\vec{P}_j\cdot\vec{Q}_j+\frac{i}{2\hbar}\vec{P}_i\cdot\vec{Q}_i \end{array}\right\} \\
&= \left(\frac{\gamma}{\pi}\right)^{3/2}\exp\left\{\begin{array}{l} -\gamma\left[R^2-\vec{R}\cdot(\vec{Q}_i+\vec{Q}_j)-\frac{i\vec{R}\cdot(\vec{Q}_j-\vec{Q}_i)}{\gamma}\right] \\ +\frac{\gamma}{2}\left(Q_i^2+Q_j^2\right)-\frac{i}{2\hbar}\vec{P}_j\cdot\vec{Q}_j+\frac{i}{2\hbar}\vec{P}_i\cdot\vec{Q}_i \end{array}\right\} \\
&= \left(\frac{\gamma}{\pi}\right)^{3/2}\exp\left\{\begin{array}{l} -\gamma\left[R^2-2\vec{R}\cdot\left(\frac{\vec{Q}_i+\vec{Q}_j}{2}+i\frac{\vec{P}_j-\vec{P}_i}{2\gamma}\right)\right] \\ +\frac{\gamma}{2}\left(Q_i^2+Q_j^2\right)-\frac{i}{2\hbar}\vec{P}_j\cdot\vec{Q}_j+\frac{i}{2\hbar}\vec{P}_i\cdot\vec{Q}_i \end{array}\right\}.
\end{aligned} \tag{A.5}$$

By defining

$$\vec{\rho}=\frac{Z_i^*+Z_j}{\sqrt{2\gamma}}=\frac{\vec{Q}_i^*+\vec{Q}_j}{2}+i\frac{\vec{P}_j^*+\vec{P}_i}{2\gamma}, \tag{A.6}$$

one can obtain

$$\begin{aligned}
\langle Z_i|\vec{R}\rangle\langle\vec{R}|Z_j\rangle &= \left(\frac{\gamma}{\pi}\right)^{3/2}\exp\left[\begin{array}{l} -\gamma\left(R^2-2\vec{R}\cdot\vec{\rho}+\frac{Q_i^2+Q_j^2}{2}\right) \\ -\frac{i}{2\hbar}\vec{P}_j\cdot\vec{Q}_j+\frac{i}{2\hbar}\vec{P}_i\cdot\vec{Q}_i \end{array}\right] \\
&= \left(\frac{\gamma}{\pi}\right)^{3/2}\exp\left[\begin{array}{l} -\gamma\left(\vec{R}-\vec{\rho}\right)^2+\gamma\rho^2-\gamma\frac{Q_i^2+Q_j^2}{2} \\ -\frac{i}{2\hbar}\vec{P}_j\cdot\vec{Q}_j+\frac{i}{2\hbar}\vec{P}_i\cdot\vec{Q}_i \end{array}\right] \\
&= \left(\frac{\gamma}{\pi}\right)^{3/2}\exp\left(\gamma\frac{Q_i^2+Q_j^2+2Q_iQ_j}{4}-\frac{P_i^2+P_j^2-2P_iP_j}{4\gamma}\right) \\
&\quad\times\exp\left(i\frac{\vec{P}_j\cdot\vec{Q}_j+\vec{P}_j\cdot\vec{Q}_i-\vec{P}_i\cdot\vec{Q}_j-\vec{P}_i\cdot\vec{Q}_i}{2}\right) \\
&\quad\times\exp\left(-\gamma\frac{Q_i^2+Q_j^2}{2}-\frac{i}{2\hbar}\vec{P}_j\cdot\vec{Q}_j+\frac{j}{2\hbar}\vec{P}_i\cdot\vec{Q}_i\right) \\
&= \left(\frac{\gamma}{\pi}\right)^{3/2}\exp\left[-\gamma\left(\vec{R}-\vec{\rho}\right)^2\right]\exp\left(\gamma\frac{Q_iQ_j}{2}-\frac{P_i^2+P_j^2}{4\gamma}+\frac{P_iP_j}{2\gamma}\right) \\
&\quad\times\exp\left(-\gamma\frac{Q_i^2+Q_j^2}{4}-\frac{i}{2\hbar}\vec{P}_i\cdot\vec{Q}_j+\frac{i}{2\hbar}\vec{P}_j\cdot\vec{Q}_i\right).
\end{aligned} \tag{A.7}$$

Since

$$\begin{aligned}\langle Z_i|Z_j\rangle &= \exp\left(Z_i^* Z_j - \frac{|Z_i|^2}{2} - \frac{|Z_j|^2}{2}\right) \\ &= \exp\left[\frac{\gamma Q_i Q_b}{2} + \frac{P_i P_j}{2\gamma} - \frac{iP_i Q_j}{2} - \left(\frac{\gamma Q_i^2}{4} + \frac{P_i^2}{4\gamma}\right) - \left(\frac{\gamma Q_j^2}{4} + \frac{P_j^2}{4\gamma}\right)\right] \\ &= \exp\left[\frac{\gamma Q_i Q_b}{2} + \frac{P_i P_j}{2\gamma} - \frac{i\vec{P}_i\cdot\vec{Q}_j}{2} + \frac{i\vec{P}_j\cdot\vec{Q}_i}{2} - \frac{\gamma}{4}\left(Q_i^2 + Q_j^2\right) - \frac{P_i^2 + P_j^2}{4\gamma}\right],\end{aligned} \tag{A.8}$$

Eq. (A.5) can be reduced to

$$\langle Z_i|\vec{R}\rangle\langle\vec{R}|Z_j\rangle = \left(\frac{\gamma}{\pi}\right)^{3/2}\exp\left[-\gamma\left(\vec{R}-\vec{\rho}\right)^2\right]\langle Z_i|Z_j\rangle. \tag{A.9}$$

A.2 The 3D potentials in the CSR

A.2.1 3D SHO potential in the CSR

Although the simple harmonic oscillator (SHO) potential is not used in this thesis, the CSs are derived from this potential, it is necessary to show this fundamental potential in the CSR. Several methods, such as direct application of the operators on the CSs, the integrations in the Cartesian or spheral coordinates can be applied to calculate the CSR of the 3D SHO potential, $V_G(R) = \frac{1}{2}m\omega^2R^2$, as well as the other quantities we are interested in in this appendix. However, in order to avoid the duplication, we only outline the last approach in this appendix.

The SHO potential in the CSR is expressed as

$$\begin{aligned}\langle Z_i|V_{SHO}(R)|Z_j\rangle &= \int\langle Z_i|\vec{R}\rangle\langle\vec{R}|\frac{1}{2}m\omega^2R^2|Z_j\rangle\mathrm{d}^3\vec{R} \\ &= \frac{1}{2}m\omega^2\int R^2\langle Z_i|\vec{R}\rangle\langle\vec{R}|Z_j\rangle\mathrm{d}^3\vec{R},\end{aligned} \tag{A.10}$$

inserting Eq. (A.9) into this equation, it can be rewritten as

$$\begin{aligned}
\langle Z_i|V_{SHO}(R)|Z_j\rangle &= \left(\frac{\gamma}{\pi}\right)^{3/2}\frac{1}{2}m\omega^2\int R^2 e^{-\gamma\left(\vec{R}-\vec{\rho}\right)^2}\mathrm{d}^3\vec{R}\langle Z_i|Z_j\rangle \\
&= \left(\frac{\gamma}{\pi}\right)^{3/2}\frac{1}{2}m\omega^2\int R^2 e^{-\gamma\left(R^2-2R\cos\theta+\rho^2\right)}\mathrm{d}^3\vec{R}\langle Z_i|Z_j\rangle \\
&= \left(\frac{\gamma}{\pi}\right)^{3/2}\pi m\omega^2\int\int R^2\sin\theta R^2 e^{-\gamma\left(R^2-2R\cos\theta+\rho^2\right)}\mathrm{d}R\mathrm{d}\theta\langle Z_i|Z_j\rangle \\
&= \left(\frac{\gamma}{\pi}\right)^{3/2}\pi m\omega^2\int\int R^4 e^{-\gamma\left(R^2-2R\cos\theta+\rho^2\right)}\mathrm{d}R\mathrm{d}\cos\theta\langle Z_i|Z_j\rangle \\
&= \left(\frac{\gamma}{\pi}\right)^{3/2}\frac{\pi}{2\gamma\rho}m\omega^2\int R^3\left[e^{-\gamma(R-\rho)^2}-e^{-\gamma(R+\rho)^2}\right]\mathrm{d}R\langle Z_i|Z_j\rangle \\
&= \left(\frac{\gamma}{\pi}\right)^{3/2}\frac{\pi}{4\gamma}m\omega^2\left(2\rho^2\gamma+3\right) \\
&= \frac{\hbar\omega}{4}\left(2\rho^2\gamma+3\right),
\end{aligned} \tag{A.11}$$

here, $\rho=\sqrt{\vec{\rho}\cdot\vec{\rho}}$.

Assumption I: Note that, in the Eq. (A.11), from the first equal sign to the second equal sign, we assume the $\vec{\rho}$ is along the $\vec{e}_z$ direction, if this is not the case, we can rotate the coordinate framework and let $\vec{\rho}$ to be along the $\vec{e}_z$, this will not change the result.

A.2.2 3D Gaussian potential in the CSR

The 3D Gaussian potential $V_G(R)=-e^{-\lambda R^2}$ in the CSR reads as

$$\langle Z_i|V_G(R)|Z_j\rangle=\int\langle Z_i|\vec{R}\rangle\langle\vec{R}|V_G(R)|Z_j\rangle\mathrm{d}^3\vec{R}=-\int e^{-\lambda R^2}\langle Z_i|\vec{R}\rangle\langle\vec{R}|Z_j\rangle\mathrm{d}^3\vec{R}. \tag{A.12}$$

Inserting Eq. (A.9) into this equation we obtain (**Assumption I** is applied here)

$$\begin{aligned}
\langle Z_i|V_G(R)|Z_j\rangle &= -\left(\frac{\gamma}{\pi}\right)^{3/2}\int e^{-\lambda R^2}e^{-\gamma(\vec{R}-\vec{\rho})^2}\mathrm{d}^3\vec{R}\langle Z_i|Z_j\rangle \\
&= -\left(\frac{\gamma}{\pi}\right)^{3/2}\int e^{-\lambda R^2}e^{-\gamma(R^2-2R\cos\theta+\rho^2)}\mathrm{d}^3\vec{R}\langle Z_i|Z_j\rangle \\
&= -\left(\frac{\gamma}{\pi}\right)^{3/2}2\pi\int\int R^2\sin\theta e^{-\lambda R^2}e^{-\gamma(R^2-2R\cos\theta+\rho^2)}\mathrm{d}R\mathrm{d}\theta\langle Z_i|Z_j\rangle \\
&= -\left(\frac{\gamma}{\pi}\right)^{3/2}2\pi\int\int R^2 e^{-\lambda R^2}e^{-\gamma(R^2-2R\cos\theta+\rho^2)}\mathrm{d}R\mathrm{d}\cos\theta\langle Z_i|Z_j\rangle \\
&= -\left(\frac{\gamma}{\pi}\right)^{3/2}\frac{\pi}{\gamma\rho}\int Re^{-\lambda R^2}\left[e^{-\gamma(R-\rho)^2}-e^{-\gamma(R+\rho)^2}\right]\mathrm{d}R\langle Z_i|Z_j\rangle \\
&= -\left(\frac{\gamma}{\pi}\right)^{3/2}\frac{\pi}{\gamma\rho}\int Re^{-(\gamma+\lambda)R^2+2\gamma R\rho-\gamma\rho^2}\mathrm{d}R\langle Z_i|Z_j\rangle \\
&\quad +\left(\frac{\gamma}{\pi}\right)^{3/2}\frac{\pi}{\gamma\rho}\int Re^{-(\gamma+\lambda)R^2-2\gamma R\rho-\gamma\rho^2}\mathrm{d}R\langle Z_i|Z_j\rangle \\
&= -\left(\frac{\gamma}{\gamma+\lambda}\right)^{3/2}e^{-\frac{\lambda\gamma}{\gamma+\lambda}\rho^2}.
\end{aligned} \tag{A.13}$$

A.2.3 3D Coulomb potential in the CSR

The 3D coulomb potential in the CSR can be written as

$$\langle Z_i|-1/R|Z_j\rangle = \int\langle Z_i|\vec{R}\rangle\langle\vec{R}|-1/R|Z_j\rangle\mathrm{d}^3\vec{R} = -\int 1/R\langle Z_i|\vec{R}\rangle\langle\vec{R}|Z_j\rangle\mathrm{d}^3\vec{R}. \tag{A.14}$$

By using Eq. (A.9), the above equation can be simplified to (**Assumption I** is applied here)

$$\begin{aligned}
\langle Z_i|-\frac{1}{R}|Z_j\rangle &= -\left(\frac{\gamma}{\pi}\right)^{3/2}\int\frac{1}{R}e^{-\gamma\left(\vec{R}-\vec{\rho}\right)^2}\mathrm{d}^3\vec{R}\langle Z_i|Z_j\rangle \\
&= -\left(\frac{\gamma}{\pi}\right)^{3/2}\int\frac{1}{R}e^{-\gamma\left(R^2-2R\cos\theta+\rho^2\right)}\mathrm{d}^3\vec{R}\langle Z_i|Z_j\rangle \\
&= -\left(\frac{\gamma}{\pi}\right)^{3/2}2\pi\int\int R^2\sin\theta\frac{1}{R}e^{-\gamma\left(R^2-2R\cos\theta+\rho^2\right)}\mathrm{d}R\mathrm{d}\theta\langle Z_i|Z_j\rangle \\
&= -\left(\frac{\gamma}{\pi}\right)^{3/2}2\pi\int\int Re^{-\gamma\left(R^2-2R\cos\theta+\rho^2\right)}\mathrm{d}R\mathrm{cos}\,\theta\langle Z_i|Z_j\rangle \\
&= -\left(\frac{\gamma}{\pi}\right)^{3/2}\frac{\pi}{\gamma\rho}\int e^{-\gamma(R-\rho)^2}-e^{-\gamma(R+\rho)^2}\mathrm{d}R\langle Z_i|Z_j\rangle.
\end{aligned} \tag{A.15}$$

Using

$$\int_0^\infty e^{-\gamma(R\pm\rho)^2}\mathrm{d}R = \frac{1}{2}\sqrt{\frac{\pi}{\gamma}}\left[1 \mp erf(\sqrt{\gamma}\rho)\right], \tag{A.16}$$

we can obtain

$$\langle Z_i| - \frac{1}{R}|Z_j\rangle = -\frac{1}{\rho}erf(\sqrt{\gamma}\rho)\langle Z_i|Z_j\rangle. \tag{A.17}$$

Therefore, the Coulomb potential $V_C(R) = -\frac{1}{R}$ in the CRS is written as

$$\langle Z_i|V_C(R)|Z_j\rangle = -\frac{1}{\rho}erf(\sqrt{\gamma}\rho)\langle Z_i|Z_j\rangle. \tag{A.18}$$

Note that, the analytical forms of 1D Coulomb and Soft-core potential in the CSR are not attainable. Since similar to Eq. (A.14) and (A.15), the analytical forms of them can be written as

$$\langle Z_i|\frac{1}{x}|Z_j\rangle = \left(\frac{\gamma}{\pi}\right)^{1/2}\int \frac{1}{x}e^{-\gamma(x-\rho)^2}\mathrm{d}x\langle z_i|z_j\rangle, \tag{A.19}$$

and

$$\langle z_i|\frac{1}{\sqrt{x^2+a}}|z_j\rangle = \left(\frac{\gamma}{\pi}\right)^{1/2}\int \frac{1}{\sqrt{x^2+a}}e^{-\gamma(x-\rho)^2}\mathrm{d}x\langle z_i|z_j\rangle, \tag{A.20}$$

but they are non-integrable.

A.3 The laser field along $\vec{e}_z$ direction in the CSR

The laser field along $\vec{e}_z$ is $\vec{R}\cdot\vec{E}(t) = zE(t) = R\cos\alpha E(t)$, otherwise stated, α denotes the angle between $\vec{e}_z$ and the vector $\vec{R}$. In the CSR, this can be calculated as follows

$$\begin{aligned}\langle Z_i|R\cos\alpha|Z_j\rangle &= \int\langle Z_i|\vec{R}\rangle\langle\vec{R}|R\cos\alpha|z_j\rangle\mathrm{d}^3\vec{R}\\ &= \int R\cos\alpha\langle Z_i|\vec{R}\rangle\langle\vec{R}|Z_j\rangle\mathrm{d}^3\vec{R}\\ &= \left(\frac{\gamma}{\pi}\right)^{3/2}\int R\cos\alpha e^{-\gamma(\vec{R}-\vec{\rho})^2}\mathrm{d}^3\vec{R}\langle Z_i|Z_j\rangle.\end{aligned} \tag{A.21}$$

Assumption II: Now, assume that after the rotation of the coordinate frame around $\vec{e}_x$, $\vec{e}_y$ and $\vec{e}_z$ with angles β_x, β_y and β_z, we can get the new $\vec{e}_{z'}$ along $\vec{\rho}$,

and the angle between $\vec{R}$ and ρ is θ. Therefore, the corresponding

$$\begin{aligned} R\cos\alpha &= x'\sin\theta_y - y'\sin\beta_x\cos\beta_y + z'\cos\beta_x\cos\beta_y \\ &= R'\sin\theta\cos\phi\sin\beta_y - R'\sin\theta\sin\phi\sin\beta_x\cos\beta_y + R'\cos\theta\cos\beta_x\cos\beta_y. \end{aligned} \tag{A.22}$$

Inserting Eq. (A.22) into Eq. (A.21) (because $R' = R$, in the following calculation we use R instead of R') and integrating over R', θ and ϕ, we can obtain

$$\begin{aligned} &\langle Z_i|R\cos\alpha|Z_j\rangle \\ &= \left(\frac{\gamma}{\pi}\right)^{3/2}\iiint R^2\sin\theta R\cos\theta\cos\beta_x\cos\beta_y e^{-\gamma(\vec{R}-\vec{\rho})^2}\mathrm{d}R\mathrm{d}\alpha\mathrm{d}\phi\langle Z_i|Z_j\rangle \\ &= 2\pi\left(\frac{\gamma}{\pi}\right)^{3/2}\cos\beta_x\cos\beta_y\iint R^3\sin\theta\cos\theta e^{-\gamma(\vec{R}-\vec{\rho})^2}\mathrm{d}R\mathrm{d}\theta\langle Z_i|Z_j\rangle \\ &= 2\pi\left(\frac{\gamma}{\pi}\right)^{3/2}\cos\beta_x\cos\beta_y\iint R^3\cos\theta e^{-\gamma(\vec{R}-\vec{\rho})^2}\mathrm{d}R\mathrm{d}\cos\theta\langle Z_i|Z_j\rangle \\ &= 2\pi\left(\frac{\gamma}{\pi}\right)^{3/2}\cos\beta_x\cos\beta_y\iint R^3\cos\theta e^{-\gamma(R^2+\rho^2-2R\rho\cos\theta)}\mathrm{d}R\mathrm{d}\cos\theta\langle Z_i|Z_j\rangle \\ &= 2\pi\left(\frac{\gamma}{\pi}\right)^{3/2}\cos\beta_x\cos\beta_y\int\frac{e^{-\gamma(R-\rho)^2}(2\gamma\rho R-1)+e^{-\gamma(R+\rho)^2}(2\gamma\rho R+1)}{4\gamma^2\rho^2}R\mathrm{d}R\langle Z_i|Z_j\rangle \\ &= 2\pi\left(\frac{\gamma}{\pi}\right)^{3/2}\frac{\cos\beta_x\cos\beta_y}{4\gamma^2\rho^2}\begin{bmatrix}\sqrt{\pi\gamma}\rho^3\left[1+erf(\sqrt{\gamma}\rho)\right]+e^{-\gamma\rho^2}\left(\rho^2-\frac{1}{2\gamma}\right)\\ +\sqrt{\pi\gamma}\rho^3\left[1-erf(\sqrt{\gamma}\rho)\right]-e^{-\gamma\rho^2}\left(\rho^2-\frac{1}{2\gamma}\right)\end{bmatrix}\langle Z_i|Z_j\rangle \\ &= 2\pi\left(\frac{\gamma}{\pi}\right)^{3/2}\frac{\cos\beta_x\cos\beta_y}{4\gamma^2\rho^2}\left\{\sqrt{\pi\gamma}\rho^3\left[1+erf(\sqrt{\gamma}\rho)\right]+\sqrt{\pi\gamma}\rho^3\left[1-erf(\sqrt{\gamma}\rho)\right]\right\}\langle Z_i|Z_j\rangle \\ &= 2\pi\left(\frac{\gamma}{\pi}\right)^{3/2}\frac{\cos\beta_x\cos\beta_y}{4\gamma^2\rho^2}2\sqrt{\pi\gamma}\rho^3\langle Z_i|Z_j\rangle \\ &= \rho_z\langle Z_i|Z_j\rangle. \end{aligned} \tag{A.23}$$

Note that, in this equation we omit the first and the second terms in Eq. (A.22), since they integrate to zero. Therefore, for the 3D system

$$\langle Z_i|\vec{R}\cdot\vec{E}(t)|Z_j\rangle = \rho_z E(t) = \vec{\rho}\cdot\vec{E}(t). \tag{A.24}$$

A.4 Dipole of different forms in the CSR

A.4.1 Dipole of acceleration form in the CSR: $\mathscr{D}^{(a)}$

Dipole acceleration of 3D SHO potential

The dipole acceleration of 3D SHO potential reads as

$$\mathscr{D}^{(a)}_{i,j} = \langle Z_i| - \nabla V_{SHO}(R)|Z_j\rangle \ = \langle Z_i| - m\omega^2\vec{R}|Z_j\rangle. \tag{A.25}$$

For the $\vec{e}_z$ direction, this term reads as

$$\langle Z_i| - m\omega^2 z|Z_j\rangle, \tag{A.26}$$

or

$$\langle Z_i| - m\omega^2 R\cos\theta\cdot\vec{e}_z|Z_j\rangle. \tag{A.27}$$

From Eqs. (A.24)-(A.29) we can get

$$\mathscr{D}^{(a)}_{i,j} = \langle Z_i| - m\omega^2 z|Z_j\rangle \ = \langle Z_i| - m\omega^2 R\cos\theta|Z_j\rangle = -m\omega^2\rho_z\langle Z_i|Z_j\rangle. \tag{A.28}$$

The dipole acceleration of 3D Gaussian potential

The dipole acceleration of 3D Gaussian potential reads as

$$\mathscr{D}^{(a)}_{i,j} = \langle Z_i| - \nabla V_G(R)|Z_j\rangle = \langle Z_i| - 2\lambda\vec{R}e^{-\lambda R^2}|Z_j\rangle. \tag{A.29}$$

For the $\vec{e}_z$ direction

$$\langle Z_i| - 2\lambda z e^{-\lambda R^2}|Z_j\rangle = \langle Z_i| - 2\lambda R\cos\theta e^{-\lambda R^2}|Z_j\rangle. \tag{A.30}$$

Similar to Eq. (A.23) and using **Assumption II**, (A.29) can be obtained as

$$\begin{aligned}
\mathscr{D}_{i,j}^{(a)} &= \langle Z_i| - 2\lambda R\cos\theta e^{-\lambda R^2}|Z_j\rangle \\
&= -2\lambda\left(\frac{\gamma}{\pi}\right)^{3/2}\int R\cos\theta\cos\beta_x\cos\beta_y e^{-\lambda R^2}e^{-\gamma\left(\vec{R}-\vec{\rho}\right)^2}\mathrm{d}^3\vec{R}\langle Z_i|Z_j\rangle \\
&= -2\lambda\left(\frac{\gamma}{\pi}\right)^{3/2}\cos\beta_x\cos\beta_y\int R\cos\theta e^{-\lambda R^2}e^{-\gamma\left(R^2-2R\rho\cos\theta+\rho^2\right)}\mathrm{d}^3\vec{R}\langle Z_i|Z_j\rangle \\
&= -4\lambda\pi\left(\frac{\gamma}{\pi}\right)^{3/2}\cos\beta_x\cos\beta_y\iint R\cos\theta e^{-\lambda R^2}e^{-\gamma\left(R^2-2R\rho\cos\theta+\rho^2\right)}R^2\sin\theta\mathrm{d}R\mathrm{d}\theta\langle Z_i|Z_j\rangle \\
&= -4\lambda\pi\left(\frac{\gamma}{\pi}\right)^{3/2}\cos\beta_x\cos\beta_y\iint R^3\cos\theta e^{-\lambda R^2}e^{-\gamma\left(R^2-2R\rho\cos\theta+\rho^2\right)}\mathrm{d}R\mathrm{d}\cos\theta\langle Z_i|Z_j\rangle \\
&= -4\lambda\pi\left(\frac{\gamma}{\pi}\right)^{3/2}\cos\beta_x\cos\beta_y\int Re^{-\lambda R^2}\frac{e^{-\gamma(R-\rho)^2(2\gamma\rho R-1)}+e^{-\gamma(R+\rho)^2(2\gamma\rho R+1)}}{4\gamma^2\rho^2}\mathrm{d}R\langle Z_i|Z_j\rangle \\
&= -2\lambda\left(\frac{\gamma}{\gamma+\lambda}\right)^{5/2}\cos\beta_x\cos\beta_y\rho e^{-\frac{\gamma\rho^2}{\gamma+\lambda}}\langle Z_i|Z_j\rangle \\
&= -2\lambda\left(\frac{\gamma}{\gamma+\lambda}\right)^{5/2}\rho_z e^{-\frac{\gamma\rho^2}{\gamma+\lambda}}\langle Z_i|Z_j\rangle.
\end{aligned} \tag{A.31}$$

Dipole acceleration of 3D Coulomb potential

For the dipole acceleration of the 3D Coulomb potential along the $\vec{e}_z$ direction, based on **Assumption II**, which can be carried out through

$$\begin{aligned}
\mathscr{D}_{i,j}^{(a)} &= \langle Z_i|\Delta\frac{1}{R}|Z_j\rangle \\
&= \left(\frac{\gamma}{\pi}\right)^{3/2}\cos\beta_x\cos\beta_y\iiint R^2\sin\theta\frac{-R\cos\theta}{R^3}e^{-\gamma(\vec{R}-\vec{\rho})^2}\mathrm{d}R\mathrm{d}\theta\mathrm{d}\phi\langle Z_i|Z_j\rangle \\
&= -\left(\frac{\gamma}{\pi}\right)^{3/2}\cos\beta_x\cos\beta_y\iiint R^2\sin\theta\sin\theta\cos\theta e^{-\gamma(\vec{R}-\vec{\rho})^2}\mathrm{d}R\mathrm{d}\theta\mathrm{d}\phi\langle Z_i|Z_j\rangle \\
&= -2\pi\left(\frac{\gamma}{\pi}\right)^{3/2}\cos\beta_x\cos\beta_y\iiint R^2\sin\theta\cos\theta e^{-\gamma(R^2+\rho^2-2R\rho\cos\theta)}\mathrm{d}R\mathrm{d}\cos\theta\langle Z_i|Z_j\rangle.
\end{aligned} \tag{A.32}$$

Integrate over $\cos\theta$ one can obtain

$$\begin{aligned}
&\langle Z_i|\Delta\frac{1}{R}|Z_j\rangle \\
=& -2\pi\left(\frac{\gamma}{\pi}\right)^{3/2}\cos\beta_x\cos\beta_y\int\frac{e^{-\gamma(R-\rho)^2}(2\gamma\rho R-1)+e^{-\gamma(R+\rho)^2}(2\gamma\rho R+1)}{4\gamma^2\rho^2R^2}\mathrm{d}R\langle Z_i|Z_j\rangle.
\end{aligned} \tag{A.33}$$

And then integrate over R, one can obtain

$$\begin{aligned}
\langle Z_i|\Delta\frac{1}{R}|Z_j\rangle &= -2\pi\left(\frac{\gamma}{\pi}\right)^{3/2}\cos\beta_x\cos\beta_y\left[\begin{array}{l}\frac{\sqrt{\pi\gamma}erf\left[\sqrt{\gamma}(R-\rho)\right]+\frac{e^{-\gamma(R-\rho)}}{R}}{4\gamma^2\rho^2}\\ -\frac{\sqrt{\pi\gamma}erf\left[\sqrt{\gamma}(R+\rho)\right]+\frac{e^{-\gamma(R+\rho)}}{R}}{4\gamma^2\rho^2}\end{array}\right]_0^\infty\\
&= -2\pi\left(\frac{\gamma}{\pi}\right)^{3/2}\cos\beta_x\cos\beta_y\left[\begin{array}{l}\frac{\sqrt{\pi\gamma}\left[1-erf(-\rho\sqrt{\gamma})\right]-\sqrt{\pi\gamma}\left[1-erf(\rho\sqrt{\gamma})\right]}{4\gamma^2\rho^2}\\ +\frac{e^{-\gamma(R-\rho)^2}-e^{-\gamma(R+\rho)^2}}{4R\gamma^2\rho^2}\Big|_0^\infty\end{array}\right]\\
&= -2\pi\left(\frac{\gamma}{\pi}\right)^{3/2}\cos\beta_x\cos\beta_y\left[\begin{array}{l}\frac{\sqrt{\pi\gamma}\left[erf(\rho\sqrt{\gamma})-erf(-\rho\sqrt{\gamma})\right]}{4\gamma^2\rho^2}\\ -2\pi\left(\frac{\gamma}{\pi}\right)^{3/2}\frac{e^{-\gamma(R-\rho)^2}-e^{-\gamma(R+\rho)^2}}{4R\gamma^2\rho^2}\Big|_0^\infty\end{array}\right]\\
&= \left[-\frac{1}{\rho^2}erf(\rho\sqrt{\gamma})-2\pi\left(\frac{\gamma}{\pi}\right)^{3/2}\frac{e^{-\gamma(R-\rho)^2}-e^{-\gamma(R+\rho)^2}}{4R\gamma^2\rho^2}\Big|_0^\infty\right]\cos\beta_x\cos\beta_y.
\end{aligned} \tag{A.34}$$

As $\lim_{R\to\infty}e^{-\gamma(R-\rho)^2}\to 0, \lim_{R\to\infty}e^{-\gamma(R+\rho)^2}\to 0$ the dipole acceleration in (A.34) can be reduced to

$$\langle Z_i|\Delta\frac{1}{R}|Z_j\rangle = \left[-\frac{1}{\rho^2}erf(\rho\sqrt{\gamma})-2\pi\left(\frac{\gamma}{\pi}\right)^{3/2}\lim_{R\to 0}\frac{e^{-\gamma(R-\rho)^2}-e^{-\gamma(R+\rho)^2}}{4R\gamma^2\rho^2}\right]\cos\beta_x\cos\beta_y. \tag{A.35}$$

Using the Taylor series to expand $e^{-\gamma(R-\rho)^2}$ and $e^{-\gamma(R+\rho)^2}$ around $R=0$,

$$\begin{aligned}
e^{-\gamma(R-\rho)^2} &= 1+(-2\gamma)(R-\rho)e^{-\gamma(R-\rho)^2}\big|_{R=0}R\\
&\quad+\left[-2\gamma e^{-\gamma(R-\rho)^2}+4\gamma^2(R-\rho)^2e^{-\gamma(R+\rho)^2}\right]\big|_{R=0}R^2+...\\
&= 1+2\gamma\rho e^{-\gamma\rho^2}R+\left[-2\gamma e^{-\gamma\rho^2}+4\gamma^2\rho^2e^{-\gamma\rho^2}\right]R^2+...
\end{aligned} \tag{A.36}$$

$$\begin{aligned}
e^{-\gamma(R+\rho)^2} &= 1+(-2\gamma)(R+\rho)e^{-\gamma(R+\rho)^2}\big|_{R=0}R\\
&\quad+\left[-2\gamma e^{-\gamma(R-\rho)^2}+4\gamma^2(R+\rho)^2e^{-\gamma(R+\rho)^2}\right]\big|_{R=0}R^2+...\\
&= 1+2\gamma\rho e^{-\gamma\rho^2}R+\left[-2\gamma e^{-\gamma\rho^2}+4\gamma^2\rho^2e^{-\gamma\rho^2}\right]R^2+...
\end{aligned} \tag{A.37}$$

Therefore,

$$\begin{aligned}
2\pi\left(\frac{\gamma}{\pi}\right)^{3/2}\lim_{R\to 0}\frac{e^{-\gamma(R-\rho)^2}-e^{-\gamma(R+\rho)^2}}{4R\gamma^2\rho^2} &= -2\pi\left(\frac{\gamma}{\pi}\right)^{3/2}\frac{4\gamma\rho e^{-\gamma\rho^2}}{4\gamma^2\rho^2}\\
&= -2\sqrt{\frac{\gamma}{\pi}}\frac{e^{-\gamma\rho^2}}{\rho}.
\end{aligned} \tag{A.38}$$

The acceleration in the $\vec{e}_z$ direction is

$$\begin{aligned}\mathscr{D}_{i,j}^{(a)} &= \left[-\frac{1}{\rho^2}erf(\rho\sqrt{\gamma}) + 2\sqrt{\frac{\gamma}{\pi}}\frac{e^{-\gamma\rho^2}}{\rho}\right]\cos\beta_x\cos\beta_y \\ &= \left[-\frac{1}{\rho^2}erf(\rho\sqrt{\gamma}) + 2\sqrt{\frac{\gamma}{\pi}}\frac{e^{-\gamma\rho^2}}{\rho}\right]\frac{\rho\cos\beta_x\cos\beta_y}{\rho} \\ &= -\frac{\rho_z}{\rho^3}erf(\rho\sqrt{\gamma}) + 2\sqrt{\frac{\gamma}{\pi}}\frac{\rho_z}{\rho^2}e^{-\gamma\rho^2}.\end{aligned} \tag{A.39}$$

A.4.2 Dipole of velocity form in the CSR: $\mathscr{D}^{(v)}$

The dipole velocity in the CSR reads as

$$\begin{aligned}\mathscr{D}_{i,j}^{(v)} &= \langle Z_i|\hat{P}|Z_j\rangle \\ &= i\int\langle Z_i|\vec{R}\rangle\nabla_R\langle\vec{R}|Z_j\rangle\mathrm{d}^3\vec{R}.\end{aligned} \tag{A.40}$$

From Eq. (A.3), we can see

$$\nabla_R\langle\vec{R}|Z_j\rangle = \left[-\gamma(\vec{R}-\vec{Q_j}) + i\vec{P_j}\right]\langle\vec{R}|Z_j\rangle, \tag{A.41}$$

therefore Eq. (A.40) can be reduced to

$$\begin{aligned}\mathscr{D}_{i,j}^{(v)} &= \langle Z_i|\hat{P}|Z_j\rangle \\ &= i\int\left[-\gamma(\vec{R}-\vec{Q_j}) + i\vec{P_j}\right]\langle Z_i|\vec{R}\rangle\langle\vec{R}|Z_j\rangle\mathrm{d}^3\vec{R} \\ &= i\left(\frac{\gamma}{\pi}\right)^{3/2}\int\left[-\gamma(\vec{R}-\vec{Q_j}) + i\vec{P_j}\right]e^{-\gamma(\vec{R}-\vec{\rho}_j)^2}\mathrm{d}^3\vec{R}\langle Z_i|Z_j\rangle.\end{aligned} \tag{A.42}$$

In Cartesian Coordinates

$$-\gamma(\vec{R}-\vec{\rho})^2 = -\gamma\left[(x-\rho_x)^2 + (y-\rho_y)^2 + (z-\rho_z)^2\right]. \tag{A.43}$$

As

$$\int_{-\infty}^{\infty} xe^{-\gamma(x-\rho_{jx})^2}\mathrm{d}x = \sqrt{\frac{\pi}{\gamma}}\rho_{jx}, \tag{A.44}$$

$$\int_{-\infty}^{\infty} e^{-\gamma(y-\rho_{jy})^2}\mathrm{d}y = \sqrt{\frac{\pi}{\gamma}}, \tag{A.45}$$

$$\begin{aligned}\int_{-\infty}^{\infty} xe^{-\gamma(\vec{R}-\vec{\rho_j})^2}\mathrm{d}^3\vec{R} &= \int_{-\infty}^{\infty} xe^{-\gamma(x-\rho_{jx})^2}\mathrm{d}x \int_{-\infty}^{\infty} e^{-\gamma(y-\rho_{jy})^2}\mathrm{d}y \int_{-\infty}^{\infty} e^{-\gamma(z-\rho_{jz})^2}\mathrm{d}z \\ &= \left(\frac{\pi}{\gamma}\right)^{3/2} \rho_{jx},\end{aligned} \tag{A.46}$$

$$\begin{aligned}\int_{-\infty}^{\infty} \vec{R}e^{-\gamma(\vec{R}-\vec{\rho_j})^2}\mathrm{d}^3\vec{R} &= \int_{-\infty}^{\infty} xe^{-\gamma(\vec{R}-\vec{\rho_j})^2}\mathrm{d}^3\vec{R}\cdot\hat{e_x} + \int_{-\infty}^{\infty} ye^{-\gamma(\vec{R}-\vec{\rho_j})^2}\mathrm{d}^3\vec{R}\cdot\hat{e_y} \\ &\quad + \int_{-\infty}^{\infty} ze^{-\gamma(\vec{R}-\vec{\rho_j})^2}\mathrm{d}^3\vec{R}\cdot\hat{e_z} \\ &= \left(\frac{\pi}{\gamma}\right)^{3/2} \vec{\rho}_j,\end{aligned} \tag{A.47}$$

we can obtain

$$\begin{aligned}\mathscr{D}_{i,j}^{(v)} &= \langle Z_i|\hat{P}|Z_j\rangle \\ &= i\left(\frac{\gamma}{\pi}\right)^{3/2}\left(\frac{\gamma}{\pi}\right)^{-3/2}\left[-\gamma(\vec{\rho}-\vec{Q_j}) + i\vec{P_j}\right]\langle Z_i|Z_j\rangle \\ &= i\left[-\gamma(\vec{\rho}-\vec{Q_j}) + i\vec{P_j}\right]\langle Z_i|Z_j\rangle.\end{aligned} \tag{A.48}$$

A.4.3 Dipole of length form in the CSR: $\mathscr{D}^{(l)}$

The dipole length form along the laser direction, in the CSR, reads as

$$\mathscr{D}_{i,j}^{(l)} = \langle Z_i|z|Z_j\rangle \tag{A.49}$$

Using Eqs. (A.21)-(A.23) one can obtain the dipole length along $\vec{e}_z$ as

$$\mathscr{D}_{i,j}^{(l)} = \langle Z_i|z|Z_j\rangle = \rho_z\langle Z_i|Z_j\rangle. \tag{A.50}$$

A.5 Derivation of $D(t)$

Starting from the Schrödinger equation

$$\frac{\mathrm{d}|\Psi(t)\rangle}{\mathrm{d}t} = -\frac{i}{\hbar}\hat{H}|\Psi(t)\rangle, \tag{A.51}$$

inserting

$$|\Psi(t)\rangle = \sum_j^n |z_j\rangle D_j e^{\frac{i}{\hbar}S_j} \tag{A.52}$$

into Eq (A.51), one can obtain

$$\begin{aligned}\frac{\mathrm{d}|\Psi(t)\rangle}{\mathrm{d}t} &= \sum_j^n \frac{\mathrm{d}|z_j\rangle D_j e^{\frac{i}{\hbar}S_j}}{\mathrm{d}t} \\ &= \sum_j^n |\dot{z}_j\rangle D_j e^{\frac{i}{\hbar}S_j} + \sum_j^n |z_j\rangle \dot{D}_j e^{\frac{i}{\hbar}S_j} + \sum_j^n \frac{i}{\hbar}\dot{S}_j |z_j\rangle D_j e^{\frac{i}{\hbar}S_j}.\end{aligned} \tag{A.53}$$

Letting $\langle z|$ act on both sides of Eq. (A.53) we can obtain

$$\langle z|\frac{\mathrm{d}|\Psi(t)\rangle}{\mathrm{d}t} = \sum_j^n \langle z_i|\dot{z}_j\rangle D_j e^{\frac{i}{\hbar}S_j} + \sum_j^n \langle z_i|z_j\rangle \dot{D}_j e^{\frac{i}{\hbar}S_j} + \sum_j^n \frac{i}{\hbar}\dot{S}_j \langle z_i|z_j\rangle D_j e^{\frac{i}{\hbar}S_j}. \tag{A.54}$$

From Eq. (5.59) we can see that

$$\langle z_i|\dot{z}_j\rangle = \langle z_i|z_j\rangle \left[\frac{\mathrm{d}z_j}{\mathrm{d}t} z_i^* - \frac{1}{2}\left(z_j \frac{\mathrm{d}z_j^*}{\mathrm{d}t} + \frac{\mathrm{d}z_j}{\mathrm{d}t} z_j^*\right)\right], \tag{A.55}$$

substituting this equation into (A.54), we can get

$$\begin{aligned}\langle z_i|\frac{\mathrm{d}|\Psi(t)\rangle}{\mathrm{d}t} &= \sum_j^n \langle z_i|z_j\rangle D_j e^{\frac{i}{\hbar}S_j}\left[\frac{\mathrm{d}z_j}{\mathrm{d}t} z_i^* - \frac{1}{2}\left(z_j \frac{\mathrm{d}z_j^*}{\mathrm{d}t} + \frac{\mathrm{d}z_j}{\mathrm{d}t} z_j^*\right)\right] \\ &+ \sum_j^n \langle z_i|z_j\rangle \dot{D}_j e^{\frac{i}{\hbar}S_j} + \sum_j^n \frac{i}{\hbar}\dot{S}_j \langle z_i|z_j\rangle D_j e^{\frac{i}{\hbar}S_j} \\ &= -\frac{i}{\hbar}\sum_j^n \langle z_i|\hat{H}|z_j\rangle D_j e^{\frac{i}{\hbar}S_j} \\ &= -\frac{i}{\hbar}\sum_j^n \langle z_i|z_j\rangle H_{ord}(z_i^*, z_j) D_j e^{\frac{i}{\hbar}S_j}.\end{aligned} \tag{A.56}$$

Therefore, we can obtain

$$
\begin{aligned}
&\sum_j^n \langle z_i|z_j\rangle \dot{D}_j e^{\frac{i}{\hbar}S_j} \\
&= \sum_j^n \langle z_i|z_j\rangle \left[-\frac{\mathrm{d}z_j}{\mathrm{d}t}z_i^* + \frac{1}{2}\left(z_j\frac{\mathrm{d}z_j^*}{\mathrm{d}t} + \frac{\mathrm{d}z_j}{\mathrm{d}t}z_j^*\right) - \frac{i}{\hbar}\dot{S}_j - \frac{i}{\hbar}H_{ord}(z_i^*, z_j)\right] D_j e^{\frac{i}{\hbar}S_j} \\
&= \sum_j^n \langle z_i|z_j\rangle \left[-\frac{\mathrm{d}z_j}{\mathrm{d}t}z_i^* + \frac{1}{2}\left(z_j\frac{\mathrm{d}z_j^*}{\mathrm{d}t} + \frac{\mathrm{d}z_j}{\mathrm{d}t}z_j^*\right) + \frac{1}{2}\left(z_j^*\frac{\mathrm{d}z_j}{\mathrm{d}t} - \frac{\mathrm{d}z_j^*}{\mathrm{d}t}z_j\right)\right] \\
&\times \exp\left[\frac{i}{\hbar}H_{ord}(z_j^*, z_j) - \frac{i}{\hbar}H_{ord}(z_i^*, z_j)\right] D_j e^{\frac{i}{\hbar}S_j} \\
&= -\frac{i}{\hbar}\sum_j^n \langle z_i|z_j\rangle \left[H_{ord}(z_i^*, z_j) - H_{ord}(z_j^*, z_j) + i\hbar\frac{\mathrm{d}z_j}{\mathrm{d}t}(z_j^* - z_i^*)\right] D_j e^{\frac{i}{\hbar}S_j} \\
&= -\frac{i}{\hbar}\sum_j^n \langle z_i|z_j\rangle \left[H_{ord}(z_i^*, z_j) - H_{ord}(z_j^*, z_j) - \frac{\partial H_{ord}(z_j^*, z_j)}{\partial z_j^*}(z_i^* - z_j^*)\right] D_j e^{\frac{i}{\hbar}S_j} \\
&= -\frac{i}{\hbar}\sum_j^n \langle z_i|z_j\rangle \delta^2 H'^*_{ord}(z_i^*, z_j) D_j e^{\frac{i}{\hbar}S_j},
\end{aligned}
\tag{A.57}
$$

where,

$$
\delta^2 H'^*_{ord}(z_i^*, z_j) = H_{ord}(z_i^*, z_j) - H_{ord}(z_j^*, z_j) - \frac{\partial H_{ord}(z_j^*, z_j)}{\partial z_j^*}(z_i^* - z_j^*), \tag{A.58}
$$

and

$$
\frac{\mathrm{d}D_k}{\mathrm{d}t} = -\frac{i}{\hbar}\sum_{ij}^n \left(\Omega^{-1}\right)_{ki}\left(\Omega_{ij}\cdot\delta^2 H'^*_{ord}(z_i^*, z_j)\right) D_j \exp\left[\frac{i}{\hbar}(S_j - S_k)\right]. \tag{A.59}
$$

Bibliography

[1] N. A. Papadogiannis, B. Witzel, C. Kalpouzos, and D. Charalambidis, Phys. Rev. Lett. **83**, 4289 (1999).

[2] R. A. Bartels, A. Paul, H. Green, H. C. Kapteyn, M. M. Murnane, S. Backus, I. P. Christov, Y. Liu, D. Attwood, and C. Jacobsen, Science **297**, 376 (2002).

[3] Z. Zeng, Y. Cheng, X. Song, R. Li, and Z. Xu, Phys. Rev. Lett. **98**, 203901 (2007).

[4] Y. Oishi, M. Kaku, A. Suda, F. Kannari, and K. Midorikawa, Opt. Express **14**, 7230 (2006).

[5] V. S. Yakovlev, M. Ivanov, and F. Krausz, Opt. Express **15**, 15351 (2007).

[6] T. Pfeifer, A. Jullien, M. J. Abel, P. M. Nagel, L. Gallmann, D. M. Neumark, and S. R. Leone, Opt. Express **15**, 17120 (2007).

[7] M. Klaiber, K. Z. Hatsagortsyan, C. Müller, and C. H. Keitel, Opt. Lett. **33**, 411 (2008).

[8] A. Baltuska, Th. Udem, M. Uiberacker, M. Hentschel, E. Goulielmakis, Ch. Gohle, R. Holzwarth, V. S. Yakovlev, A. Scrinzi, T. W. Hänsch, and F. Krausz, Nature **421**, 611 (2003).

[9] G. Sansone, E. Benedetti, F. Calegari, C. Vozzi, L. Avaldi, R. Flammini, L. Poletto, P. Villoresi, C. Altucci, R. Velotta, S. Stagira, S. De Silvestri, and M. Nisoli, Science **314**, 443 (2006).

[10] E. Goulielmakis, M. Schultze, M. Hofstetter, V. S. Yakovlev, J. Gagnon, M. Uiberacker, A. L. Aquila, E. M. Gullikson, D. T. Attwood, R. Kienberger, F. Krausz, and U. Kleineberg, Science **320**, 1614 (2008).

[11] J. Itatani, J. Levesque, D. Zeidler, H. Niikura, H. Pépin, J. C. Kieffer, P. B. Corkum, and D. M. Villeneuve, Nature **432**, 867 (2004).

[12] M. Lein, J. Phys. B, **40** R135, (2007).

[13] F. Krausz and M. Ivanov, Rev. Mod. Opt., **81** 163, (2009).

[14] S. Haessler, J. Caillat, W. Boutu, C. Giovanetti-Teixeira, T. Ruchon1, T. Auguste, Z. Diveki, P. Breger, A. Maquet, B. Carré, R. Taïeb, and P. Salières, Nature Physics **6**, 200 (2010).

[15] S. Haessler, J. Caillat, and P Salières, J. Phys. B, **44** 203001, (2011).

[16] P. B. Corkum, Phys. Rev. Lett., **71** 1994, (1993).

[17] J. L. Krause, K. J. Schafer, and K. C. Kulander, Phys. Rev. Lett. **68**, 3535 (1992).

[18] K. J. Schafer, B. Yang, L. F. DiMauro, and K. C. Kulander, Phys. Rev. Lett. **70**, 1599 (1993).

[19] K. C. Kulander, K. J. Schafer, and J. L. Krause, in Superintense Laser-Atom Physics, NATO Advanced Study Institute Series B: Physics, edited by B. Piraux, A. L'Huillier, and K. Rzazewski, Vol. 316, Chap. 19, p. 95, Plenum, New York (1993).

[20] M. Lewenstein, Ph. Balcou, M. Yu. Ivanov, Anne L'Huillier, and P. B. Corkum, Phys. Rev. A **49**, 2117 (1994).

[21] Ph. Antoine, B. Piraux, and A. Maquet, Phys. Rev. A **51**, 1750 (1995).

[22] C. Figueira de Morisson Faria, M. Dörr, and W. Sandner, Phys. Rev. A **55**, 3961 (1997).

[23] A. de Bohan, Ph. Antoine, D. B. Milošević, and B. Piraux, Phys. Rev. Lett. **81**, 1837 (1998).

[24] X. M. Tong and S. I. Chu, Phys. Rev. A **61**, 021802(R) (2000).

[25] M. Protopapas, D. G. Lappas, C. H. Keitel, and P. L. Knight, Phys. Rev. A **53**, R2933 (1995)

[26] G. van de Sand and J. M. Rost, Phys. Rev. Lett. **83**, 524 (1999).

[27] C. Zagoya, C. M. Goletz, F. Grossmann, and J. M. Rost, New J. Phys., **14** 093050 (2012).

[28] C. Zagoya, C. M. Goletz, F. Grossmann, and J. M. Rost, Phys. Rev. A, **85** 041401(R) (2012).

[29] A. Emmanouilidou, Phys. Rev. A **78**, 023411 (2008).

[30] D. F. Ye, X. Liu, and J. Liu, Phys. Rev. Lett. **101**, 233003 (2008).

[31] W. Quan, Z. Lin, M. Wu, H. Kang, H. Liu, X. Liu, J. Chen, J. Liu, X. T. He, S. G. Chen, H. Xiong, L. Guo, H. Xu, Y. Fu, Y. Cheng, and Z. Z. Xu, Phys. Rev. Lett. **103**, 093001 (2009).

[32] C. Zagoya, "*Semiclassical Descriptionof Quantum Interference in Nonlinear Dynamics*", PhD thesis (2013).

[33] L. V. Keldysh, Sov. Phys. JETP **20**, 1307 (1965).

[34] Zh. Eksp, Teor. Fiz. **47**, 1945 (1964).

[35] F. H. M. Faisal, J. Phys. B **6**, L89 (1973).

[36] H. R. Reiss, Phys. Rev. A **22**, 1786 (1980).

[37] C. I. Blaga, F. Catoire1, P. Colosimo, G. G. Paulus, H. G. Muller, P. Agostini, and L. F. DiMauro1, Nature Physics **5**, 335 (2009).

[38] D. A. Telnov and S. I. Chu, Phys. Rev. A **83**, 063406 (2011).

[39] T. M. Yan, S. V. Popruzhenko, M. J. J. Vrakking, and D. Bauer, Phys. Rev. Lett. **105**, 253002 (2010).

[40] A. Rudenko, K. Zrost, C. D. Schöter, V. L. B. de Jesus1, B. Feuerstein, R. Moshammer, and J. Ullrich, J. Phys. B **37**, L407 (2004).

[41] D. G. Arbó, S. Yoshida, E. Persson, K. I. Dimitriou, and J. Burgdörfer, Phys. Rev. Lett. **96**, 143003 (2006).

[42] A. Kamor, F. Mauger, C. Chandre, and T. Uzer, Phys. Rev. Lett. **110**, 253002 (2013).

[43] F. Mauger, C. Chandre, and T. Uzer, Phys. Rev. Lett. **105**, 083002 (2010).

[44] S. V. Popruzhenko, G. G. Paulus, and D. Bauer, Phys. Rev. A **77**, 053409 (2008).

[45] O. Smirnova, M. Spanner, and M. Ivanov, J. Phys. B **39**, S307 (2006).

[46] O. Smirnova, M. Spanner, and M. Ivanov, Phys. Rev. A **77**, 033407 (2008).

[47] Y. Okajima, O. I. Tolstikhin, and T. Morishita, Phys. Rev. A **85**, 063406 (2012).

[48] O. I. Tolstikhin and T. Morishita, Phys. Rev. A **86**, 043417 (2012).

[49] S. Baier, C. Ruiz, L. Plaja, and A. Becker, Phys. Rev. A **74**, 033405 (2006).

[50] S. Baier, C. Ruiz, L. Plaja, and A. Becker, Laser Phys. **17**, 358 (2007).

[51] P. B. Corkum and F. Krausz, Nature Physics **3**, 381 (2007).

[52] M. Drescher, M. Hentschel, R. Kienberger, M. Uiberacker, V. Yakovlev, A. Scrinzi, Th. Westerwalbesloh, U. Kleineberg, U. Heinzmann, and F. Krausz, Nature **419**, 803 (2002).

[53] M. Uiberacker, Th. Uphues, M. Schultze, A. J. Verhoef, V. Yakovlev, M. F. Kling, J. Rauschenberger, N. M. Kabachnik, H. Schröder, M. Lezius, K. L. Kompa, H. G. Muller, M. J. J. Vrakking, S. Hendel, U. Kleineberg, U. Heinzmann, M. Drescher, and F. Krausz, Nature **446**, 627 (2007).

[54] A. L. Cavalieri, N. Müller, Th. Uphues, V. S. Yakovlev, A. Baltuška, B. Horvath, B. Schmidt, L. Blümel, R. Holzwarth, S. Hendel, M. Drescher, U. Kleineberg, P. M. Echenique, R. Kienberger, F. Krausz, and U. Heinzmann, Nature **449**, 1029 (2007).

[55] M. F. Kling, Ch. Siedschlag, A. J. Verhoef, J. I. Khan, M. Schultze, Th. Uphues, Y. Ni, M. Uiberacker, M. Drescher, F. Krausz, and M. J. J. Vrakking, Science **312**, 246 (2007).

[56] K. Burnett, V. C. Reed, J. Cooper, and P. L. Knight, Phys. Rev. A **45**, 3347 (1992).

[57] J. L. Krause, K. J. Schafer, and K. C. Kulander, Phys. Rev. A **45**, 4998 (1992).

[58] D. Bohm, Phys. Rev. **85**, 166 (1952); ibid. 180 (1952).

[59] P. R. Holland, "*The Quantum Theory of Motion: An Account of the de-Broglie-Bohm Causal Interpretation of Quantum Mechanics*", Cambridge University Press, Cambridge (1993).

[60] X. Y. Lai, Q. Y. Cai, and M. S. Zhan, Eur. Phys. J. D **53**, 393 (2009).

[61] X. Y. Lai, Q. Y. Cai, and M. S. Zhan, New J. Phys. **11**, 113035 (2009).

[62] X. Y. Lai, Q. Y. Cai, and M. S. Zhan, Chin. Phys. B **19**, 020302 (2010).

[63] P. Botheron and B. Pons, Phys. Rev. A **83**, 062704 (2010).

[64] N. Takemoto and A. Becker, J. Chem. Phys. **134**, 074309 (2011).

[65] A. Picón, A. Benseny, J. Mompart, J. R. Vázquez de Aldana, L. Plaja, G. F. Calvo, and L. Roso, New J. Phys. **12**, 083053 (2010).

[66] A. Benseny, A. Picón, J. Mompart, L. Plaja, and L. Roso, *Hydrogen photoionization with strong lasers, in Applied Bohmian Mechanics: From Nanoscale Systems to Cosmology*, X. Oriols and J. Mompart Ed., ch. 2, Pan Standford Publishing, Singapore (2012).

[67] P. Botheron and B. Pons, Phys. Rev. A **82**, 021404R (2010).

[68] Y. Song, F. M. Guo, S. Y. Li, J. G. Chen, S. L. Zeng, and Y. J. Yang, Phys. Rev. A **86**, 033424 (2012).

[69] Y. Song, S. Y. Li, X. S. Liu, F. M. Guo, and Y. J. Yang, Phys. Rev. A **88**, 053419 (2013).

[70] S. S. Wei, S. Y. Li, F. M. Guo, Y. J. Yang, and B. B Wang, Phys. Rev. A **87**, 063418 (2013).

[71] J. Wu, B. B. Augstein, and C. Figueira de Morisson Faria, Phys. Rev. A **88**, 023415 (2013).

[72] J. Wu, B. B. Augstein, and C. Figueira de Morisson Faria, Phys. Rev. A **88**, 063416 (2013).

[73] R. E. Wyatt, *Quantum Dynamics with Trajectories*, Springer, New York (2005).

[74] A. S. Sanz and S. Miret-Artés, *A Trajectory Description of Quantum Processes*. I. Fundamentals, Lecture Notes in Physics 850 Springer, Berlin (2012).

[75] A. S. Sanz and S. Miret-Artés, Am. J. Phys. **80**, 525 (2012).

[76] E. Madelung, Z. Phys. **40**, 322 (1926).

[77] W. H. Miller and T. F. George, J. Chem. Phys. **53**, 3578 (1970).

[78] W. H. Miller and T. F. George, J. Chem. Phys. **56**, 5668 (1972).

[79] J. H. Van Vleck, Pro. Natl. Acad. Sci. U.S.A. **14**, 178 (1928).

[80] M. C. Gutzwiller, J. Math. Phys. **12**, 343 (1971).

[81] M. C. Gutzwiller, *Chaos in Classical and Quantum Mechanics*, Springer-Vertag, New York (1990).

[82] M. F. Herman and E. Kluk, Chem. Phys. **91**, 27 (1984).

[83] E. Kluk, M. F. Herman, and H. L. Davis, J. Chem. Phys. **84**, 326 (1986) .

[84] M. F. Herman, Annu. Rev. Phys. Chem. **45**, 83 (1994).

[85] D. V. Shalashilin and M. S. Child, J. Chem. Phys. **113**, 10028 (2000).

[86] D. V. Shalashilin and M. S. Child, J. Chem. Phys. **114**, 9296 (2001).

[87] D. V. Shalashilin and M. S. Child, J. Chem. Phys. **115**, 5367 (2001).

[88] D. V. Shalashilin and M. S. Child, J. Chem. Phys. **118**, 2061 (2003).

[89] D. V. Shalashilin and M. S. Child, J. Chem. Phys. **119**, 1961 (2003).

[90] D. V. Shalashilin, M. S. Child, and D. C. Clary, J. Chem. Phys. **120**, 5608 (2004).

[91] D. V. Shalashilin and M. S. Child, J. Chem. Phys. **121**, 3563 (2004).

[92] D. V. Shalashilin and M. S. Child, Chem. Phys. **304**, 103 (2004).

[93] D. V. Shalashilin and M. S. Child, J. Chem. Phys. **122**, 224108 (2005).

[94] D. V. Shalashilin and M. S. Child, J. Chem. Phys. **122**, 224109 (2005).

[95] D. V. Shalashilin, J. Chem. Phys. **128**, 054102 (2008).

[96] D. V. Shalashilin, M. S. Child, and A. Kirrander, Chem. Phys. **347**, 257 (2008).

[97] D. V. Shalashilin, J. Chem. Phys. **130**, 244101 (2009).

[98] A. Kirrander and D. V. Shalashilin, Phys. Rev. A, **84**, 033406 (2011).

[99] J. Guo, X. S. Liu, and S. I. Chu, Phys. Rev. A, **82**, 023402 (2010).

[100] R. E. Wyatt, "*Quamtum Dynamics with Trajectories: Introduction to Quantum Hydrodynamics*", Springer (2005).

[101] I. P. Christov, J. Chem. Phys. **135**, 044120 (2011).

[102] I. P. Christov, J. Chem. Phys. **135**, 149902 (2011).

[103] E. Lipparini, *Mordern Many-Particle Physics*, World Scientific, Singapore (2003).

[104] H. Nikolic, Foundations of Physics Letters, **17**, 363 (2004).

[105] H. Nikolic, Foundations of Physics Letters, **18**, 123 (2005).

[106] H. Nikolic, Foundations of Physics Letters, **18**, 549 (2005).

[107] H. Nikolic, International J. Mod. Phys. A, **25**, 1477 (2010).

[108] Z. S. Wang, G. R. Darling, and S. Holloway, J. Chem. Phys. **115**, 22 (2001).

[109] C. Figueira de Morisson Faria, R. Kopold, W. Becker, and J. M. Rost, Phys. Rev. A **65**, 023404 (2002).

[110] L. Lehtovaara, J. Toivanen, and J. Eloranta, J. Comp. Phys. **221**, 148 (2007).

[111] M. D. Feit, J. A. Fleck, Jr., and A. Stieger, J. Comp. Phys. 47, 412 (1982).

[112] W. H. Press, S. A. Teukolsky, W. T. Vetterling, and B. P. Flannery, *Numerical Recipes in Fortran 77: The Art of Scientific Computing*, Vol. 1, 2nd Ed., Cambridge University Press, Cambridge (1992).

[113] M. Ruggenthaler, S. V. Popruzhenko, and D. Bauer, Phys. Rev. A **78**, 033413 (2008).

[114] B. Sundaram, and P. W. Milonni, Phys. Rev. A **41**, 6571 (1990).

[115] W. Becker, S. Long, and J. K. McIver, Phys. Rev. A **50**, 1540 (1994).

[116] W. Becker, A. Lohr, M. Kleber, and M. Lewensterin, Phys. Rev. A **56**, 645 (2008).

[117] P. Saliéres, B. Carré, L. Le Déroff, F. Grasbon, G. G. Paulus, H. Walther, R. Kopold, W. Becker, D. B. Milošević, A. Sanpera, and M. Lewenstein, Science **292**, 902 (2001).

[118] C. Figueira de Morisson Faria and B. B. Augstein, Phys. Rev. A **81**, 043409 (2010).

[119] B. B. Augstein and C. Figueira de Morisson Faria, J. Phys. B **44**, 055601 (2011).

[120] B. B. Augstein and C. Figueira de Morisson Faria, Modern Physics Letters B **26**, 113002 (2012).

[121] P. Antoine, A. L'Huillier, and M. Lewenstein, Phys. Rev. Lett. **77**, 1234 (1996).

[122] F. I. Gauthey, B. M. Garraway, and P. L. Knight, Phys. Rev. A **56**, 3093 (1997).

[123] C. Figueira de Morisson Faria, M. Dörr, and W. Sandner, Phys. Rev. A **58**, 2990 (1998).

[124] D. Gabor, J. IEEE, **93**, 429 (1946).

[125] I. Daubechies, "*Ten Lectures on Wavelets*", Society for Industrial and Applied Mathmematics, Philadelphia (1992).

[126] S. G. Malat, "*A Wavelet tour of Signal Processing*", Academic press, London (1998).

[127] P. Antoine, B. Piraux, and A. Maquet, Phys. Rev. A **51**, R1750 (1995).

[128] C. C. Chirilă, I. Dreissigacker, E. V. van der Zwan, and M. Lein, Phys. Rev. A **81**, 033412 (2010).

[129] M. F. Ciappina, J. Biegert, R. Quidant, and M. Lewenstein, Phys. Rev. A **85**, 033828 (2012).

[130] M. F. Ciappina, S. S. Aćimović, T. Shaaran, J. Biegert, R. Quidant, and M. Lewenstein, Opt. Express **24**, 26261 (2012).

[131] J. Wu, B. B. Augstein, C. Figueira de Morisson Faria, A. Kirrander, and D. Shalashilin, *High Intensity Lasers and High Field Phenomena Conference*, doi: 10.1364/HILAS.2012.JT2A.53, Berlin, Germany (2012).

[132] J. A. Hostetter, J. L. Tate, K. J. Schafer, and M. B. Gaarde, Phys. Rev. A **82**, 023401 (2010).

[133] S. Dey and A. Fring, Phys. Rev. A **88**, 022116 (2013).

[134] L. Plaja and J. A. Pérez-Hernandez, Opt. Express **15**, 3629 (2007).

[135] J. A. Pérez-Hernandez, J. Ramos, L. Roso, and L. Plaja, Laser Phys. **20**, 1044 (2010).

[136] M. B. Gaarde and K. J. Schafer, Phys. Rev. A **65**, 031406(R) (2002).

[137] J. A. Pérez-Hernandez, and L. Plaja, Phys. Rev. A **76**, 023829 (2007).

[138] W. P. Schleich, M. Freyberger, and M. S. Zubairy, Phys. Rev. A **87**, 014102 (2013).

[139] R. N. Porter and L. M. Raff, *Dynamics of Molecular Collisions*, edited by W. H. Miller, Plenum, New York (1976).

[140] M. Karplus and G. A. Petsko, Nature **347**, 631 (1990).

[141] M. P. Allen and D. J. Tildesley, *Computer Simulation of Liquids* ,Clarendon, Oxford (1987).

[142] J. C. Tully, Catal. Lett. **9**, 205 (1991).

[143] W. H. Miller, W. L. Hase, and L. Darling, J. Chem. Phys. **91**, 2863 (1989).

[144] J. W. Bowman, B. Gazdy, and Q. Sun, J. Chem. Phys. **91**, 2859 (1989).

[145] M. Ben-Nun and R. D. Levine, J. Chem. Phys. **101**, 8768 (1994).

[146] X. Sun and W. H. Miller, J. Chem. Phys. **108**, 8870 (1998).

[147] A. L. Kaledin and W. H. Miller, J. Chem. Phys. **118**, 7174 (2003).

[148] A. L. Kaledin and W. H. Miller, J. Chem. Phys. **119**, 3078 (2003).

[149] F. Grossmann, Chem. Phys. Lett. **262**, 470 (1996).

[150] A. R. Walton and D. E. Manolopoulos, Chem. Phys. Lett. **244**, 448 (1995).

[151] G. Campolieti and P. Brumer, J. Chem. Phys. **107**, 791 (1997).

[152] S. Garashchuk and D. Tannor, Chem. Phys. Lett. **262**, 477 (1996).

[153] S. Garashchuk and J. C. Light, J. Chem. Phys. **114**, 1060 (2001).

[154] Y. Elran and K. G. Kay, J. Chem. Phys. **116**, 10577 (2002).

[155] H. Wang, X. Y. Song, D. Chandler, and W. H. Miller, J. Chem. Phys. **110**, 4828 (1999).

[156] V. Batista and P. Brumer, Phys. Rev. Lett. **89**, 143201 (2002).

[157] H. B. Wang, M. Thoss, K. L. Sorge, R. Gelabert, X. Giménez, and W. H. Miller, J. Chem. Phys. **114**, 2562 (2001).

[158] Y. Elran and P. Brumer, J. Chem. Phys. **121**, 2673 (2004).

[159] W. H. Miller, Adv. Chem. Phys. **25**, 69 (1974).

[160] M. Thoss and H. B. Wang, Annu. Rev. Phys. Chem. **55**, 299 (2004).

[161] L. A. Curtiss, P. C. Redfern, and K. Raghavachari, J. Chem. Phys. **126**, 084108 (2007).

[162] R. Saha, *Semi-classical Dynamics using initial value representations and Coherent path integrals*, PhD thesis (2008).

[163] G. D. Billing, J. Chem. Phys. **65**, 1 (1976).

[164] S. Tsuzuki, T. Uchimaru, K. Tanabe, and T. Hirano, J. Phys. Chem. **97**, 13469 (1993).

[165] S. Hammes-Schiffer and J. C. Tully, J. Chem. Phys. **101**, 4657 (1994).

[166] M. Hintenender, F. Rebentrost, R. Kosloff, and R. B. Gerber, J. Chem. Phys. **105**, 11347 (1996).

[167] P. Žd'ánská, B. Schmidt, and P. Jungwirth, J. Chem. Phys. **110**, 6246 (1999).

[168] W. H. Miller, J. Phys. Chem. A **105**, 2942 (2001).

[169] R. P. Feynman and A. R. Hibbs, *Quantum mechanics and path integrals*, p76-78, New York, McGraw-Hill (1965).

[170] E. J. Heller, Acc. Chem. Res. **14**, 368 (1981).

[171] M. A. Sepúlveda and E. J. Heller, J. Chem. Phys. **101**, 8016 (1994).

[172] M. A. Sepúlveda and F. Grossmann, Adv. Chem. Phys. **96**, 191 (1996).

[173] W. H. Miller, J. Chem. Phys. **53**, 1949 (1970).

[174] W. H. Miller, Chem. Phys. Lett. **7**, 431 (1970).

[175] W. H. Miller, AdV. Chem. Phys. **30**, 77 (1975).

[176] R. A. Marcus, Chem. Phys. Lett. **7**, 252 (1970).

[177] R. A. Marcus, J. Chem. Phys. **54**, 3965 (1971).

[178] R. A. Marcus, J. Chem. Phys. **56**, 3548 (1972).

[179] H. Kreek and R. A. Marcus, J. Chem. Phys. **61**, 3308 (1974).

[180] D. E. Fitz and R. A. Marcus, J. Chem. Phys. **59**, 4380 (1973).

[181] S. Keshavamurthy and W. H. Miller, Chem. Phys. Lett. **218**, 189 (1994).

[182] F. Grossmann and E. J. Heller, Chem. Phys. Lett. **241**, 45 (1995).

[183] N. T. Maitra and E. J. Heller, Phys. Rev. Lett. **78**, 3035 (1997).

[184] K. G. Kay, J. Chem. Phys. **107**, 2313 (1997).

[185] K. G. Kay, Annu. Rev. Phys. Chem. **56**, 255 (2005).

[186] T. J. Martinez, M. Ben-Nun, and G. Ashkenazi, J. Chem. Phys. **104**, 2847 (1996).

[187] H. D. Meyer, U. Manthe, and L. S. Cederbaum, Chem. Phys. Lett. **165**, 73 (1990).

[188] I. Burghardt, H. D. Meyer, and L. S. Cederbaum, J. Chem. Phys. **111**, 2927 (1999).

[189] G. A. Worth and I. Burghardt, J. Chem. Phys. **268**, 502 (2003).

[190] D. V. Shalashilin, J. Chem. Phys. **132**, 244111 (2012).

[191] E. Schrödinger, *Der stetige Übergang von der Mikro- zur Makromechanik, Naturwissenschaften*, **14**, 644 (1926).

[192] J. von Neumann, *Mathematical Foundations of Quantum Mechanics*, Princeton University Press (1996).

[193] R. J. Glauber, Phys. Rev. **131**, 2766 (1963).

[194] E. C. G. Sudarshan, Phys. Rev. Lett. **10**, 277 (1963).

[195] R. J. Glauber, Phys. Rev. **130**, 2529 (1963).

[196] U. M. Tltulaer and R. J. Glauber, Phys. Rev. **145**, 1041 (1966).

[197] J. R. Klauder, J. Math. Phys. **4**, 1055 (1963).

[198] V. V. Dodonov, J. Opt. B **4**, R1 (2002).

[199] J. R. Klauder, J. Phys. A **29**, L293 (1996).

[200] P. Majumdar and H. S. Sharatchandra, Phys. Rev. A **56**, R3322 (1997).

[201] R. F. Fox, Phys. Rev. A **59**, 3241 (1999).

[202] R. F. Fox and M. H. Chol, Phys. Rev. A **61**, 032107 (2000).

[203] J. R. Choi, Phys. Lett. A **325**, No.1, 1 (2004).

[204] L. Vela-Arevalo and R. F. Fox, Phys. Rev. A **71**, 063403 (2005).

[205] W. P. Schleich, *Quamtum Optics in Phase Space*, p295-297,Berlin (2001).

[206] W. H. Louisell, *Quamtum Properties of Radiation*, p109, New York (1990).

[207] D. V. Shalashilin and B. Jackson, Chem. Phys. Lett. **318**, 305 (2000).

[208] J. C. Burant and V. Batista, J. Chem. Phys. **116**, 2748 (2002).

[209] D. Huber and E. J. Heller, J. Chem. Phys. **87**, 5302 (1987).

[210] D. Huber and E. J. Heller, J. Chem. Phys. **89**, 4752 (1988).

[211] D. Huber, S. Ling, D. G. Imre, and E. J. Heller, J. Chem. Phys. **90**, 7317 (1989).

[212] B. W. Spath and W. H. Miller, J. Chem. Phys. **104**, 95 (1995).

[213] K. G. Kay, J. Chem. Phys. **100**, 4432(1994).

[214] M.F. Herman, J. Chem. Phys, **85**, 2069 (1986).

[215] K. G. Kay, J. Chem. Phys, **100**, 4377 (1994).

[216] E. Wigner, Phys. Rev. **40**, 749 (1932).

[217] A. Czirjak, R. Kopold, W. Becker, M. Kleber, and W. P. Schleich, Opt. Comm. **179**, 29 (2000).

[218] H. J. Kull, New J. Phys. **14**, 055013 (2012).

[219] A. Czirjak, S. Majorosi, J. Kovács, and M. G. Benedict, Phys. Scripta, **T153**, 014013 (2013).

[220] M. Lein, V. Engel, and E. K. U. Gross, Opt. Exp. **8**, 411 (2001).

[221] S. Gräfe, J. Doose, and J. Burgdörfer, J. Phys. B **45**, 055002 (2012).

[222] N. L. Balazs and A. Voros, Ann. Phys. **199**, 123 (1990).

[223] D. M. Heim, W. P. Schleich, P. M. Alsing, J. P. Dahl, and S. Varro, Phys. Lett. A **377**, 1822 (2013).

[224] A. Szabo and N. Ostlund, *Modern quantum chemistry: Introduction to advance electronic structure theory*, New York: McMillan (1982).